Dark Matter Search With The First Year Of Data From The DEAP-3600 Experiment

by

Thomas J. McElroy

A thesis submitted in partial fulfillment of the requirements for the degree of

Doctor of Philosophy

Department of Physics
University of Alberta

Abstract

Dark Matter is a fundamental building block and is essential for the universe to be understood on many scales. Currently, the top candidate for Dark Matter is a weakly interacting massive particle (WIMP). The DEAP-3600 experiment was built to search for rare interactions between baryonic matter and a WIMP. With 3257 $\pm$ 112 kg of liquid Argon (LAr), DEAP-3600 searches for elastic collisions between WIMPs and Ar nuclei.

Particle interactions with Ar create scintillation light that is measured with 255 Photomultiplier Tubes (PMTs). The PMTs are coupled to the detector through 0.5 m long light guides (LGs). To optimize the light collection efficiency of the detector and maximize the structural integrity of the detector, the LGs were bonded directly to the acrylic vessel (AV). To perform the LG bonding special equipment and techniques were developed in order to properly attach each of the LGs in such a way that they withstand the thermo-stresses from the cryogenic cooldown of the detector. An overview of the LG bonding development and execution is discussed.

The signal from the PMTs are recorded with digitizers. The PMT pulses are analyzed with a derivative pulse finding method capable of handling a large dynamic range of pulse rates and are fit with a resolution of $\sim$0.1 ns. A data reduction method is used to remove the digitized pulse traces from single photo-electrons. The removed pulse traces are replaced with summary information about the pulse providing $\sim$45% reduction in data file size.

The optical characteristics of the detector have been studied and the op-

tical parameters of the detector simulation have been tuned to match. The optical parameters for liquid argon (LAr) are updated and the optical models for the wavelength shifter and LG reflectors are optimized to improve the constancy between data and Monte Carlo. The tuned optics allows improved understanding of the detector and reduced radial bias in the event position reconstruction.

Overlapping ^{39}Ar-on-^{39}Ar and ^{39}Ar-on-Cherenkov events (pile-up) are removed from data using several specially developed techniques. Using a Monte Carlo to generate pile-up events from two data events, the methods are shown to be sufficient at removing pile-up events with no leakage of pile-up events entering the WIMP region of interest. The acceptance to single ^{39}Ar decays and ^{40}Ar recoils is measured using simulated events from the RAT detector simulation.

An analysis is performed using 2.05 ± 0.07 tonne-years of data, a limit on the WIMP-nucleon cross-section was set at 9.24×10^{-45} cm^2 for a 100 GeV WIMP(90% C.L.). This result is strongly limited by the presence of a large, currently unknown background. The background is inconsistent with neutron leakage as well as radioactivity at the edges of the LAr volume.

Preface

The work presented in this thesis is the author's own except where noted below. Direct use of the work of collaborators is indicated via appropriate citations in the body of the thesis.

The DEAP-3600 collaboration consists of approximately 100 researchers who, over the course of 10 years, have designed, built, commissioned and operated the detector. Over the course of 7 years with the project, the author's contributions have touched on each of the project's stages and the work presented in this thesis outlines the primary efforts in that period. Of particular note are the author's contributions to the light guide bonding, the development of pulse-finding algorithms, data stream reduction via the SmartQT method, tuning of the optical model of the detector, and rejection of event pile-up the data taking. Each of these are touched on in turn here.

Chapter 3 of the thesis discusses the bonding of the acrylic light guides. This was a coordinated effort that involved the entire DEAP group at the University of Alberta as well as the SNOLAB group during the on-site construction period. The author joined the light guide bonding project at a time when the tests with static bonds were in the final stages and the composition of the bonding syrup had been determined. The author's key contributions included development of the auto-fill system to simultaneously bond 10 light guides, as well as the control software to monitor the bonding process. The author assisted the University of Alberta group in completing the other final elements of the light-guide bonding development. During the SNOLAB construction period for the light guide bonding, the author was tasked with

overseeing the day-to-day bonding activities.

The development of the pulse-finding, SmartQT, and pile-up rejection algorithms presented in the thesis are the author's own. However, the full implementation of each of these involved input from collaborators. Of specific note, Ben Smith (TRIUMF) provided the collaboration review of the pulse-finding algorithm prior to its incorporation into the general RAT software framework. Ben Smith also incorporated the SmartQT algorithm into the frontend code. James Bueno (University of Alberta) participated in the review and testing of the Multi-Event pile-up identification algorithm, discussed in Chapter 8.

The tuning of the detector's optical model (discussed in Chapter 7) is primarily the work of the author, including the development of the related Monte Carlo simulation. Contributions by Courtney Mielnchuk (University of Alberta) are noted in the development of optical surface models and investigations into acrylic fluorescence that were incorporated.

Finally, the presented analysis (Chapter 9) was developed by the author largely independent from other collaborators with the exception of the event selections and calibration values discussed in Chapter 4 with appropriate references provided.

Acknowledgements

I would like to express my sincere thanks to my supervisors Aksel Hallin and Darren Grant. I can't imagine having better supervisors than you two. I stayed at the University of Alberta for graduate school specifically to work with you, and I have never regretted this decision.

To my parents, I can not thank you enough for all of your love and support throughout my whole life. You have always encouraged me to go for my dreams and gave me the support I need to see them through.

I am very thankful to the full DEAP collaboration, everyone from the principal investigators to the summer students and support staff, it has been great working with all of you. I especially want to think my University of Alberta collaborators, particularly Berta Beltran, Pierre Gorel, James Beuno, Rhys Chouinard and Courtney Mielnchuk.

I additionally thank fellow graduate students Tania Wood, Sarah Nowicki, Logan Sibly, Pawel Mekarski, and Jie Hu. Coffee breaks with you were always a welcome distraction.

Last, I thank those who helped keep me sane over these last seven years, particularly my climbing partners, housemates, and close friends.

Table of Contents

List of Tables

List of Figures

List of Abbreviations

List of commonly used abbreviations

AARF	Acrylic and Aluminum Reflector Fibre.
ADC	Analog to Digital Converter
AMU	Atomic Mass Units, (1.66×10^{-27} kg)
AP	After Pulse
AV	Acrylic Spherical Vessel
Bq	Becquerel, 1 decay/second (radioactivity)
CMSSM	Constrained Minimal Supersymmetric Model
CMB	Cosmic Microwave Background
DAQ	Data Acquisition
DEAP	Dark matter Experiment with Argon and Pulse shape discrimination
DM	Dark Matter
DTM	Digitizer and Trigger Module
eV	electronVolt, 1.6×10^{-19} Joules
FWHM	Full Width at Half Maximum
GEANT	GEometry ANd Tracking software
GeV	Giga-electronVolt
GR	General Relativity
HQE	High Quantum Efficiency
HG	High Gain
HV	High Voltage
keVee	kilo-electronVolts electron equivalent

kg	kilogram
kpc	kiloparsec (3.086×10^{19} m)
LAr	Liquid Argon
LET	linear energy transfer
LG	Light Guide
LN	Liquid Nitrogen
LY	Light Yield
MACHO	Massive Compact Halo Object
MC	Monte-Carlo
MOND	MOdified Newtonian Dynamics
MMA	Methyl MethAcrylate
MSSM	Minimal SuperSymmetric Model
ns	nano-second
PE	photo-electron
PMMA	Poly-Methyl MethAcrylate
PMT	Photomultiplier Tube
PSD	Pulse Shape Discrimination
Q	Charge
QE	Quantum Efficiency
QPE	Charge in units of mean single photo-electron pulse charge
RAT	the Reactor Analysis Tool
RMS	Root Mean Square
ROI	Region Of Interest

SCB	Signal Conditioning Board
SHM	Standard Halo Model
SM	Standard Model of particle physics
SPE	Single Photo-Electron
SS	Steel Shell
SUSY	Supersymmetry
TOF	Time-Of-Flight
TPB	Tetraphenyl-Butadiene
UV	Ultra-Violet
VUV	Vacuum Ultra-Violet
WIMP	Weakly Interacting Massive Particle
ZLE	Zero Length Encoding

Chapter 1

Introduction

1.1 History of Dark Matter

The Newtonian theory of gravity and its descendent General Relativity, have been the backbone of Astrophysics since the 18th century. The discovery of discrepancies between predictions and measurements have identified of new planets and other previously unobserved celestial bodies. In 1846, the existence of Neptune was discovered by John Galle [1], who located the planet within 1^o of its predicted location; computed by Le Varrier who analyzed peculiarities in Uranus's motion. However, discrepancies started to appear in the 19th century as astronomers began probing deeper into the sky with better instruments. The ratio of mass-to-light was calculated and found to be much higher than the local system by observing the motion in galaxies and galactic clusters. One of the fundamental early measurements came from F. Zwicky, who in 1937, measured the orbital velocities of galaxies in the Coma cluster and discovered that they are much faster than expected from the observed amount of visible

matter [2]. On the galactic level measurements of the rotational velocities of stars in galaxies, V. Rubin and W. Ford in the 1970's used the Doppler shift of the 21-cm H_α line to measure the rotational curve of M31 [3], the Milky Way's galactic neighbour, and found a higher value than expected from the observed amount of luminous matter [3]. Since then, rotation curves have been measured in many other galaxies, showing the same high velocity behaviour at large radii [4] [5]. Figure 1.1 shows an example of a galactic rotation curve of the galaxy NGC 3198 [4]. As shown in the plot, an additional mass component is needed to explain the high velocities at large radii.

As the evidence accumulated, the astronomical community concluded that there must be a "dark matter" component to the universe that remains unseen.

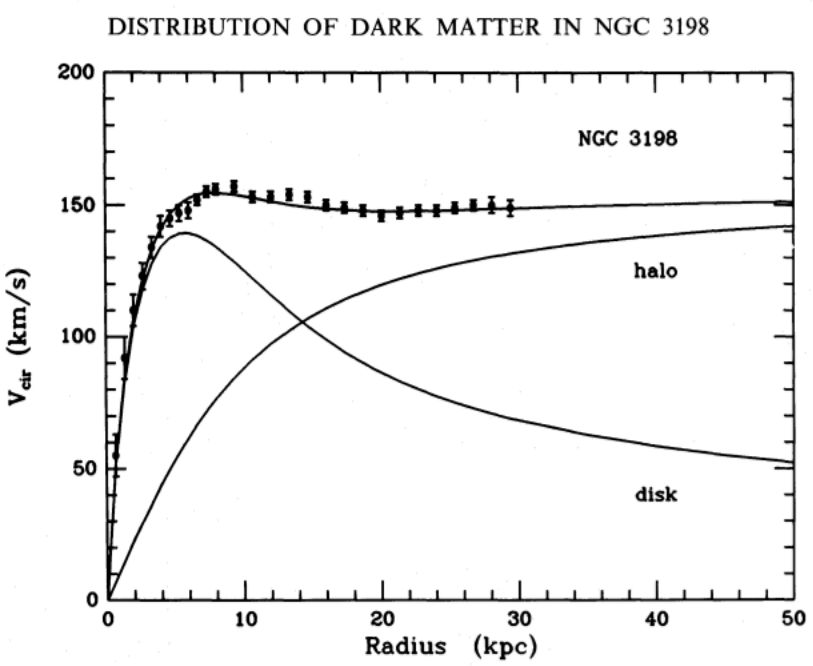

Figure 1.1: Rotation curve for Galaxy NGC 3198. The contributions to the orbital velocity from the visible disk and dark matter halo are shown [4].

The early "dark matter" concepts were not as exotic as what we currently

discuss today [6]. It was not until the late 1980's when particle physicists started to get involved with astronomy that the real discovery potential of Dark Matter was realized. As particle physicists got involved with the puzzle, the list of known particles that could contribute to Dark Matter was quickly crossed off leaving only theoretical particles. Today we see dark matter as a clear path to explore theories beyond the Standard Model of particle physics. Prospective theories are not considered complete unless they contain a dark matter candidate.

1.2 CMB and the λ cosmological model

One of the significant accomplishments in physics over the last 100 years has been the development of cosmology, which was first initially considered to be a field filled with pure speculation with no testable hypotheses [6]. With the astonishing discovery made by Edwin Hubble that distant objects are moving away from us at a rate proportional to their distance, the conclusion that the universe is expanding was soon reached [7]. This notion had been opposed by theorists, such as Albert Einstein, who had fought to formulate equations for a static universe [8]. This discovery is called Hubble's Law [9], and, as a consequence, it implies there was a time in the distant past where all the matter in the universe must have been in a very dense state that expanded and flew apart which is referred to as the Big Bang. Eventually, theorists started formulating an understanding of the early universe, building the first models of nucleosynthesis [10]. Constrained by the measurements of the abundances of light nuclei, the amounts of hydrogen through lithium where able to

be accurately calculated [11]. As the universe continued to expand, and the matter cooled to the point where neutral atoms could be formed, the radiation would become thermally uncoupled from the matter component allowing the radiation to freely propagate [1]. General relativity predicts that due to the expansion of the universe, this radiation would be stretched and today would be in the range of microwave wavelengths. This radiation is referred to as the Cosmic Microwave Background(CMB). Since its first accidental measurement by A. Penzias and R. Wilson [12], the CMB has been extensively studied for its cosmogenic implications. While early measurements lacked the resolution to measure the minute differences in the wavelength spectrum coming from a different location in the sky [12], today's satellites are capable of measuring the discrete in-homogeneity in the energies of the CMB [13]. These measurements have allowed cosmologists to extract critical information about the universe including the portion of the universe that is in the form of dark matter [14]. The latest measurements of the CMB come from the Planck satellite [13]. Measuring the angular size and amplitude of the inhomogeneities in the spectrum, a map of the temperature profile of the early universe can be made. Regions of higher matter densities create hot spots in the universe. Transforming this map into spherical harmonics gives indications to the scale of structures in the early universe. Parameters in the ΛCDM cosmological model can then be fit to the data. Figure 1.2 shows the CMB Map measured by Planck as well as the power spectrum of the spherical harmonics in the temperature in-homogeneity. Planck found that 84% of the total matter content of the universe must be in the form of dark matter [13].

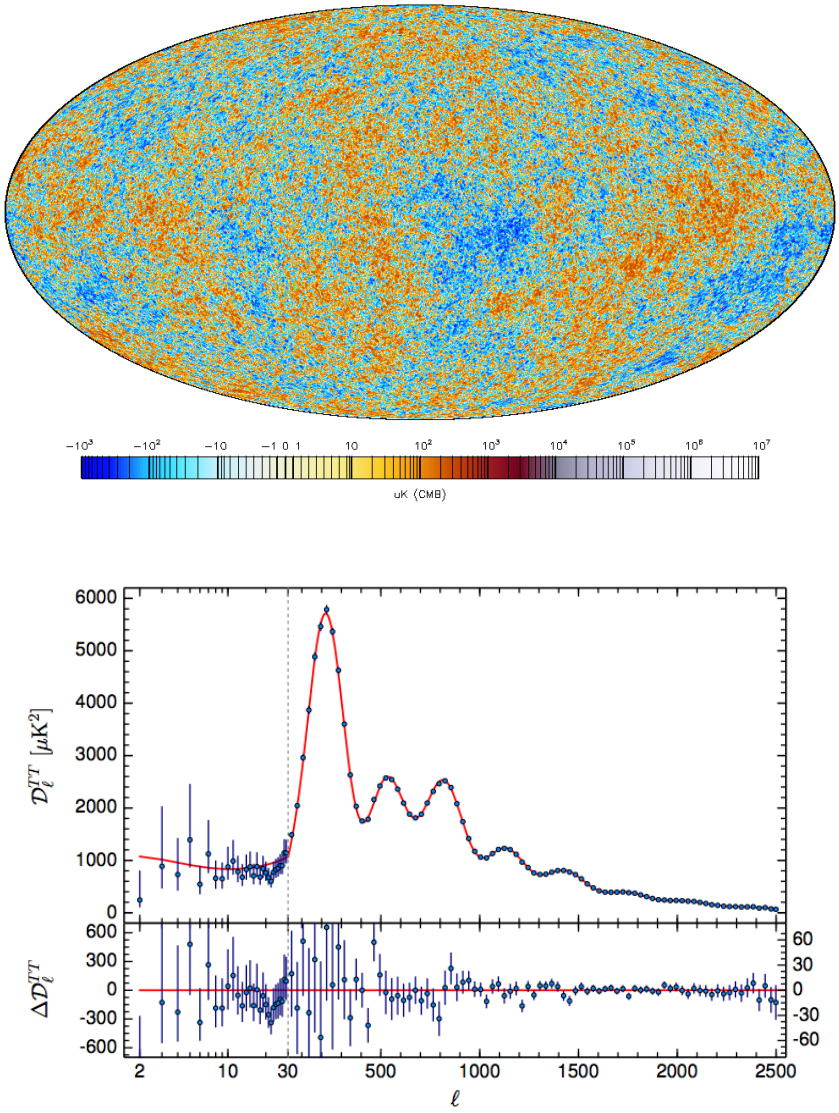

Figure 1.2: (Top) Map of the temperature fluctuations in the CMB measured by the Planck satellite [15]. (Bottom) The power spectrum of the spherical harmonic decomposition of the CMB temperature fluctuations, l is the multipole index [13].

1.3 Galactic Halo Model and Local DM measurements

As previously mentioned, one of the major pieces of evidence for DM comes from the rotation of galaxies. These measurements are particularly important for the detection of DM in our local area. As shown in Figure 1.1, a halo distribution of matter is required to account for the shape of the galactic rotational curves. This halo is assumed to consist of a dark matter gas which is nearly collision-less [16]. Our basic model for this halo of gas is called the standard Halo Model (SHM) [17]. In the SHM, the halo is assumed to be spherical with a density profile given by [17]:

$$\rho(r) = \frac{\rho_{crit}\delta_c}{(r/r_s)(1+r/r_s)^2}, \tag{1.1}$$

where ρ_{crit} is the critical closure density, δ_c is a dimensionless density factor and r_s is a scale radius. At the Sun's radius in the Milky Way, the Dark Matter mass density is $\rho_o = 0.3\text{GeVc}^{-2}\text{cm}^{-3}$ [18]. The number density of DM particles is then ρ/m_χ. The velocity distribution of DM in the halo is modelled to be Maxwellian as:

$$f(\text{v}) = \frac{1}{(2\pi)^3\sigma^3} e^{-(\text{v}-\text{v}_{lag})^2/2\sigma^2}, \tag{1.2}$$

with the velocity dispersion distribution σ is typically taken to be $\simeq 156$ km/s such that $2\sigma^2 = v_{glax}^2$ where v_{glax} is the rotational velocity of the galaxy [19]. The velocity v_{lag} has contributions from the Sun's motions through the galaxy and the Earth's velocity around the Sun. To first order, Earth's motion around

the Sun can be neglected. In this case, $v_{lag} \simeq 230$ km/s is typically used [19]. The effects of the earth's orbital motion will be discussed in Section 1.6.5. This velocity distribution cannot extend arbitrarily high since DM is gravitationally bound to the galaxy. This truncates the velocity distribution at the gravitational escape velocity, $v_{esc} \simeq 544$ km/s [20]. The Sun is travelling through the halo creating a DM wind passing through the Earth.

Possible Dark Matter candidates will be discussed in the following sections; however, first a brief examination of the attempt to explain the observations with modifications to the theory of gravity.

1.3.1 Modified Newtonian Dynamics

While a large part of the scientific community interpreted the orbital velocity observations meant that there was an unseen matter that accounted for the missing mass, there where others who started working under the assumption that the theory of gravity is wrong and needs to be modified to account for long-range behaviour [21]. These new theories are referred to as Modified Newtonian Dynamics (MOND). The basic idea of MOND theories is to assume that Newton's 2nd Law is the large acceleration limit of a higher order equation where gravitational acceleration (g_N) is in the form:

$$\mu(g/a_0)g = g_N, \tag{1.3}$$

where g is the classical acceleration and $u(\frac{g}{a_0})$ is an unknown transition function; where $\mu(x) \to 1$, at $x \gg 1$ and $\mu(x) \to x$ at $x \ll 1$ [21]. With the correct choice of $u(\frac{g}{a_0})$ the dynamics of the flat galactic rotation curves can be

reproduced [21], as well as the high velocities measured in galaxy clusters [22]. Despite the apparent mathematical breakthrough, many MOND theories suffer from the loss of conservation laws and a lack of a true relativistic extension [6].

MOND theories, for the most part, have been abandoned as a viable solution to the apparent mass discrepancy particularly after the 2006 measurements of the Bullet Cluster. The Bullet Cluster is formed from the collision of two clusters. Observations have been made of the Bullet Cluster; that looked at the distribution of the baryonic matter by observations of X-rays [23]. A second measurement mapped the distribution of matter through observing the magnitude of gravitational lensing [24]. Figure 1.3 shows an artificially coloured image showing the intensity of the X-ray emission overlaid with and the mass distribution measure using gravitational lensing shown in the green contours. What can be seen from the distributions is a difference in the interactions of the majority of the mass component of the clusters versus the baryonic components. While the baryonic matter in the two clusters collides and interacts, the bulk of the mass (presumably largely composed of dark matter) [24] passes with very little evidence for interaction. This observation strongly points to a component that behaves like a very weakly interacting gas that carries the majority of the mass of the cluster.

1.3.2 Massive Compact Halo Objects

Massive Compact Halo Objects (MACHOs) were a promising early candidate for DM. MACHOs are objects, such as black holes and brown dwarfs that are are difficult to observationally detect but have large mass. A number of

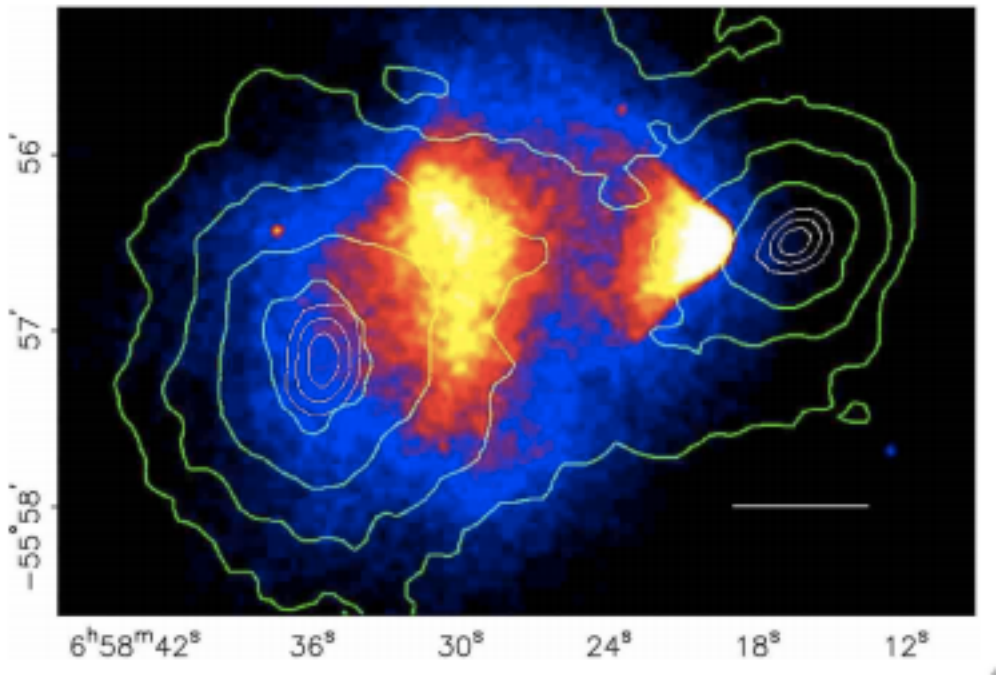

Figure 1.3: Image of the Bullet Cluster from the Chandra X-Ray Observatory with an exposure time of 500 ks. Shown in green contours is the weak lensing reconstructed surface mass density [24].

microlensing observations have been made to measure the population density of such objects. These objects are limited to 8% of DM mass coming from MACHOs [25]. The total mass of post-baryogenesis MACHOs are heavily constrained by the total baryon budget of the universe. A potential loophole is if the MACHOs consist of primordial black holes created in the Big Bang pre-baryogenesis. Bounds can be reasonably set for the mass that exists in the form of primordial black holes between 10^{14} kg and 10^{23} kg based on the lack of microlensing events and the lack of Hawking radiation [6].

1.3.3 Particle Dark Matter

Before discussing the possible particle candidates for Dark Matter, a distinction needs to be made between two types of Dark Matter commonly described as hot and cold. Hot Dark Matter consists of low mass particles that would remain relativistic through the major structure formation epoch [6]; an example being neutrinos. Cold Dark Matter is a matter; that would be non-relativistic during structure formation.The primary distinction between these two forms of dark matter comes from the order that different structure scales form in the universe. Computer simulations have shown that in a predominantly hot dark matter universe, structures would be formed in a "top-down" order, where large structures would be formed first and smaller structures, such as galaxies, would form later. In a cold dark matter dominated universe, small perturbations would quickly form galaxies, and the galaxies would then form larger structures such as galactic clusters in a "bottom-up" order. To match the observed structure formation and the estimated age of galaxies, simulations show that we must have a predominantly cold dark matter universe [26].

The next sections will discuss possible sources of cold dark matter.

Sterile Neutrinos

While neutrinos have been ruled out as a candidate for cold DM [6], with the discovery of the neutrino mass [27], a new question arises; where are the right-handed neutrinos [28]? One hypothesis is that the right-handed neutrinos exist but with much larger mass than the other neutrinos [29]. Since the weak force only interacts with left-handed neutrinos, right-handed neutrinos would

essentially be sterile and practically collision-less. There is no clear mechanism for production; however, the method most popular is through the decay of some massive scalar particle during the Big Bang [30]. The effect of sterile neutrinos are searched for by looking for oscillations with SM neutrinos. To date, no evidence has been seen for the existence of a heavy sterile neutrino [29].

Axions

Axions are a theoretical Goldstein boson that is created due to a proposed broken U(1) symmetry called the Penci-Quinn (PQ) symmetry [31]. This symmetry was first introduced as a solution to the strong Charge Parity (CP) problem in quantum chromodynamics [32]. Axions are very light particles with a mass given by

$$m_a \sim 6\text{eV}(\frac{10^6\text{GeV}}{f_a}), \tag{1.4}$$

where f_a is the energy scale where the PQ symmetry breaks, which is expected to be close to the Planck scale [31]. Although this would make the axion very light, they would not be in thermal equilibrium with the rest of the matter in the universe and would remain a potential source of cold dark matter. If they exist, axions take part in many astronomical events like supernovas. As such, there are many constraints derived from outside direct searches [31] [33] [34]. The primary way for axion Dark Matter searches is through the axion-photon coupling ($g_{a\gamma\gamma}$) where an axion interacts with an electromagnetic field and converts into a photon. The axions are very light particles meaning that, from conservation of momentum, these photons would be in the microwave range of the electromagnetic spectrum. The experiment which is currently leading

the field in the Axion dark matter search is ADMX [35]. ADMX is an axion helioscope that consists of a cold microwave resonator cavity. The cavity is tuned to a specific frequency that corresponds to a specific axion mass. A frequency range is then swept to search for a range of axion masses. The latest results from ADMX excludes $g_{a\gamma\gamma} \gtrsim 4 \times 10^{-16}(\mathrm{GeV}^{-1})$ for axion masses between 2.66 and 2.81 μeV [35].

Weakly Interacting Massive Particles

Weakly Interacting Massive Particles (WIMPs) are currently the most popular DM candidate. One of the primary traits that make the WIMP so attractive is that they are easy to incorporate into the Big Bang model and naturally have an abundance that meets the criteria. This is referred to as the "WIMP Miracle" [18].

WIMP Miracle

In the early universe, the various components were in thermal equilibrium; meaning the production and annihilation of particles were in balance $\phi + \phi \leftrightarrow \psi + \psi$ [18]. Since, the universe is continuously expanding and this expansion Doppler shifts the wavelength of relativistic particles; effectively cooling them [36]. Eventually the particles cool below the point where collisions of the lighter particles cannot create the more massive particles. At this point, the density of the heavy particles go through a period of exponential decay as they continue to self-annihilate. When the number of particles has dropped to the point that the decrease in the number density due to the annihilation is less than the reduction due to expansion, $\Gamma_{anni} = H$, the particles "freeze out." Be-

yond freeze out, the particle's co-moving density remains nearly constant [37]. The Boltzmann equation describes the dynamics of this whole process [18]:

$$\frac{dn}{dt} + 3Hn = -\langle\sigma v\rangle(n^2 - n_{eq}^2). \tag{1.5}$$

Here n is the number density, H is the Hubble expansion constant, $\langle\sigma v\rangle$ is the thermally averaged cross-section for annihilation, and n_{eq} is the number of particles when in equilibrium ($n^2 - n_{eq}^2 = 0$ during thermal equilibrium). If a new particle is considered to have been in equilibrium in the early universe, using some typical weak-scale numbers, an estimate for its freeze out density can be made. Using the critical density for the observed universe, the co-moving relative density can be approximated to be [18]:

$$\Omega_\chi h^2 = m_\chi n_\chi/\rho_c \simeq (3 \times 10^{-27}\text{cm}^3\text{s}^{-1}/ < \sigma_{Anni} v >), \tag{1.6}$$

where h is the Hubble expansion constant in units 100 km s^{-1} Mpc^{-1}. If an interaction cross section around the weak scale is applied $\langle\sigma v\rangle \simeq \alpha^2(100\text{GeV})^{-2} \simeq 10^{-25}$ for $\alpha \simeq 10^{-2}$, then the expected abundance is approximately what is needed to account for Dark Matter [18]. Figure 1.4 shows how the strength of the cross section reduces the abundance by lengthening the exponential decay period before expansion dominates. This argument is referred to as the "WIMP miracle" and solidified the idea that Dark Matter is likely made of a weakly interacting massive particle (WIMP).

There are no candidates for a WIMP within the standard model of particle physics; however, an extension to the SM provides an interesting candidate.

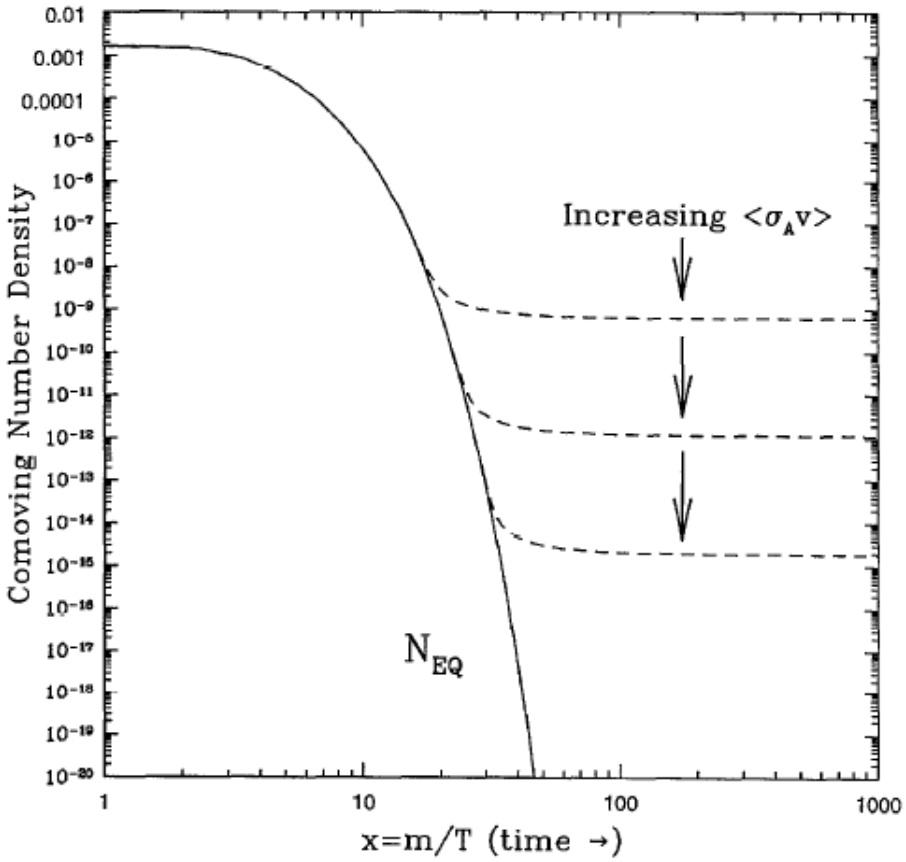

Figure 1.4: The co-moving number density of WIMPs in the early universe. The solid line indicates the density if the WIMP remain in thermal equilibrium. The dashed lines show the effect of the "freeze out" for increasing thermally averaged cross-sections. The X-axis shows the ratio between the WIMP mass (m) and the temperature of the universe (T). The increase in this ratio is due to the cooling of the universe with time. Figure taken from Ref. [36].

1.4 Supersymmetric Dark Matter

Particle theory extensions to the Standard Model give a number of candidates for WIMPs [18]. SUSY is a theorized new symmetry where there is a boson partner to every fermion and vice versa. SUSY's main features is its solution to the hierarchy problem in the SM [38]. The hierarchy problem is that over the

whole range that the Higgs mass could be, it turns out to be at the lower end at 124.97 ± 0.24 GeV [39]. By introducing a boson-fermion symmetry, terms for these new particles get included in the Higgs mass calculation. Since there is a sign difference between contributions from fermions and bosons, this provides cancellations that explain why the Higgs mass is small [40]. The fundamental operator for SUSY is Q. Q is the transformation operator between fermions and bosons:

$$Q|fermion\rangle = |boson\rangle, Q|boson\rangle = |fermion\rangle. \tag{1.7}$$

If SUSY were an unbroken symmetry, the super-partners would have the same mass as their SM counterparts. This is obviously not the case since such particles would have been discovered in colliders [38]. For SUSY to still solve the hierarchy problem, the super-partners must have masses O(TeV) [18]. The names for SUSY partners for SM fermions are prefixed with an "s" for scalar (selectron, squark, etc.). For the SUSY partners of SM bosons, an added "ino" suffix is added to the name (wino, photino, etc.). The neutral wino, bino, and higgsino states mix into four mass eigenstates referred to as neutralinos [40]. Along with the new symmetry, a new conserved quantity called R-parity is introduced. R-parity, defined by: $P_R = (-1)^{2S+3B+L}$ gives all Standard Model particles $P_R = 1$ and all SUSY particles $P_R = -1$. If it is not violated, R-parity conserves the stability of the proton and guarantees that the lightest SUSY particle (LSP) is stable [40]. In the minimal supersymmetric model (MSSM) this is the lightest neutralino state. Neutralinos weakly interact with matter through Z, H, h and squark exchange with quarks; shown in Figure 1.5 [18].

These interactions are split into the axial-vector and scalar components, discussed later in their contribution to the spin-dependent and spin-independent WIMP searches. The introduction of SUSY creates many new parameters; this makes prediction challenging. In MSSM, 105 new parameters need to be set. Simplifications and constraints must be applied to reduce the complexity. The Constrained MSSM (CMSSM) is often used for this purpose. The CMSSM uses available data, astronomical arguments and a few simplifications to reduce the parameter space. The CMSSM reduces the relevant number of parameters for making phenomenological predictions to just 5 [41]. While the CMSSM cannot be the end of the story, this model is useful for deriving constraints on the SUSY parameter space from WIMP-nucleon cross section measurements.

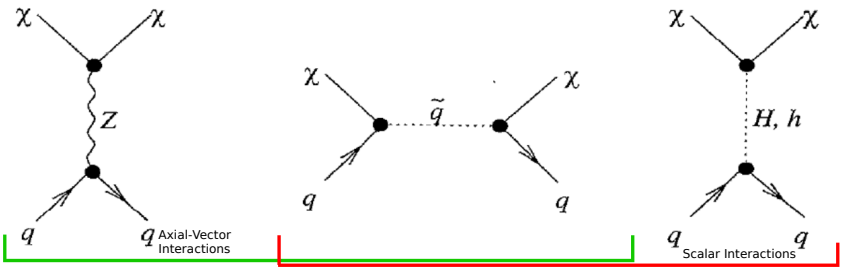

Figure 1.5: First order diagrams for SUSY WIMPs with quarks [18].

1.5 Previous Searches for WIMPs

Searches for dark matter have been performed over last 30 years by many experiments. While several experiments have published dark matter signals [42] [43] [44], it is still generally accepted that a positive WIMP signal has

yet to be discovered due to the lack of consistency between experiments [45]. There are two categories of WIMP detection experiments: indirect and direct.

1.5.1 Indirect Detection

Indirect detection WIMP searches look for WIMP annihilation signatures. The most useful signals are from high energy neutrinos from WIMP annihilation in the sun [46]. When WIMPS scatter off nuclei within large objects, such as the Sun, they lose energy. If the WIMP loses sufficient energy in the scatters, it may become gravitationally bound to the object. An accumulation of WIMPs will cause an increase in the probability for annihilation. The annihilation products of the WIMP will quickly react or decay and can produce neutrinos with high energies on the order of $\frac{1}{3}m_\chi$ to $\frac{1}{2}m_\chi$ [18]. These neutrinos are considerably more energetic than solar or geoneutrinos, and are capable of being detected by many neutrino detectors. The IceCube experiment currently holding the lead in indirect detection from solar observations, excluding spin-dependant nucleon cross-sections down to 10^{-40} cm^{2}for a $\sim$ 200 GeV WIMP [47].

1.5.2 Direct Detection

Direct detection experiments attempt to directly measure WIMP interactions through WIMP scatters off target nuclei in a detector. WIMP-nucleon scattering can be divided up into two different contributions: spin-dependent and spin-independent interactions.

Spin-Dependent

A spin-dependent interaction occurs when the WIMP particle couples with the spin of the nucleus through axial-vector interactions [18]. This interaction primarily happens between a WIMP and an unpaired nucleon within the nucleus. Targets for spin-dependent interactions are favourably lighter nuclei with odd atomic numbers and high spin moments. The ratio between the SD and SI cross sections is $\sigma_{SD}/\sigma_{SI} \approx 250\eta_A$ [18]. The parameter η_A is the spin moment of the nucleus, molecules with high fluorine ($\eta_A = 0.0071$ [18]) content have been used in a number of "spin-dependent" experiments [48] [49]. The most sensitive spin-dependent results to date have been presented by the PICO experiment, which excludes WIMP SD cross-sections down to $3.4 \times 10^{-41}\text{cm}^2$ at a WIMP mass of 30 GeV/c^2 [50] (see Figure 1.6).

Spin-Independent

The spin-independent interaction occurs when the WIMP couples with the mass of the target nucleus through scalar interactions. While weaker than the SD interaction, the scalar interaction coherently adds between all nucleons in the target nucleus [18]. Experiments that utilize the spin-independent interaction are therefore optimized by using nuclei with large atomic numbers. Spin-Independent direct detection will be the focus of this thesis. Currently, the leading limit for this type of experiment is set by the XENON1T experiment, reaching a WIMP-nucleon scattering sensitivity of $7.7 \times 10^{-47}\text{cm}^2$ at a WIMP mass of 35 GeV/c^2 [60] (see Figure 1.7).

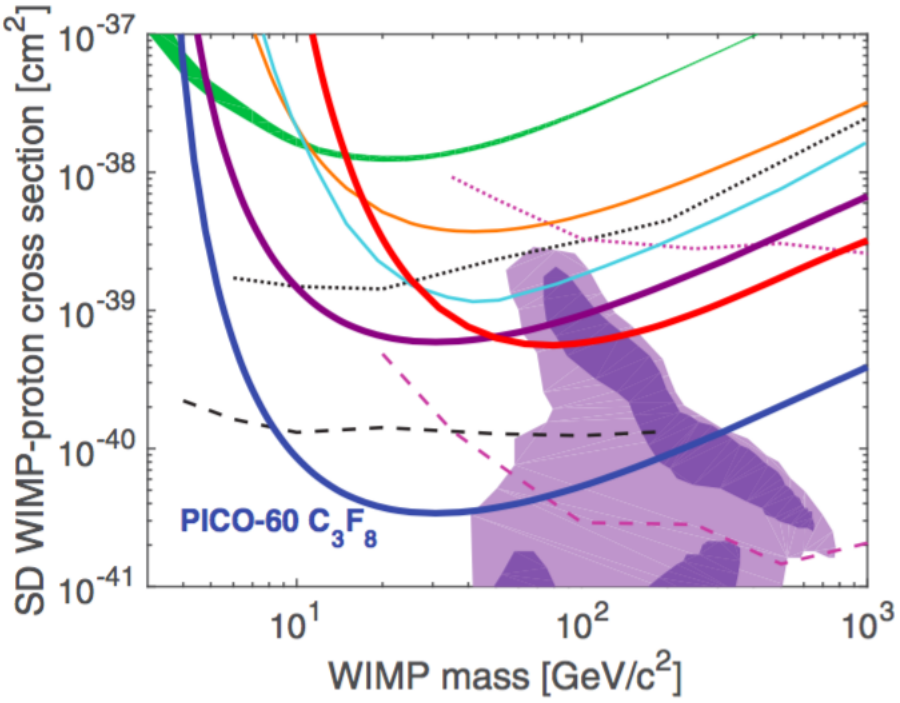

Figure 1.6: Limits on the spin-dependent WIMP-proton elastic scattering cross-section from PICO-60 C_3F_8 (thick blue) [50], along with limits from PICO-60CF_3I (thick red) [51], PICO-2L (thick purple) [52],PICASSO (green band) [53], SIMPLE (orange) [54], PandaX-II (cyan) [55],IceCube (dashed and dotted pink) [56], and SuperK (dashed and dotted black) [57] [58]. The indirect limits from IceCube and SuperK assume annihilation to τ leptons (dashed) and b quarks (dotted). The constrained minimal supersymmetric model parameter space is shown in the purple region [59]. Plot taken from Ref. [50].

1.6 WIMP Event Rate and Energy Spectrum

In order to make predictions and test theories the expected WIMP signal needs to be computed. The differential event rate per target nuclei for a generic WIMP interaction in a terrestrial detector is given by [19]:

$$\frac{dR}{dE_R} = \frac{\rho_o \sigma_N}{2\mu_{\chi N} m_\chi} A^2 F^2(E_R) \eta(v_{min}). \tag{1.8}$$

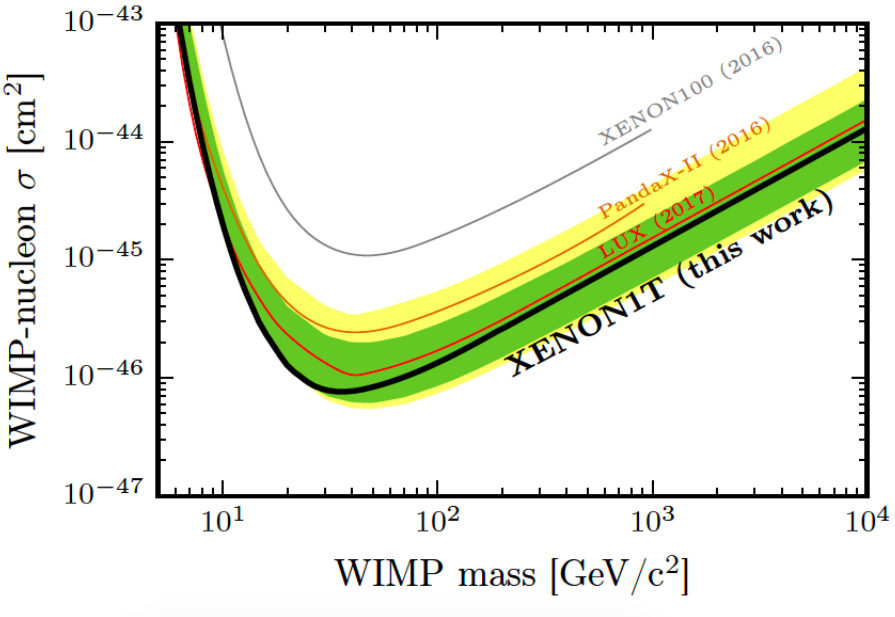

Figure 1.7: The spin-independent WIMP-nucleon cross-section limits as a function of WIMP mass at 90% confidence level. (black) XENON1T [60], (green and yellow) 1 and 2σ sensitivity bands for XENON1T result, (red) LUX [61], (brown) PandaX-II [62], and (gray) XENON100 [63]. Plot taken from Ref. [60]

This relationship contains terms with contributions from particle physics, nuclear physics, astronomical observations/models, collision kinematics and detector limitations. These contributions are each explained next.

1.6.1 Kinematics

Since WIMPs in the galactic halo are non-relativistic, classical conservation of energy and momentum in an elastic scatter can be applied to derive the minimal WIMP velocity to induce a recoil with energy E_r on target with mass m_N as:

$$v_{min} = \sqrt{\frac{E_r m_N}{2\mu_{N\chi}^2}}, \tag{1.9}$$

where $\mu_{N\chi}$ is the reduced mass between the WIMP and target. This is included in the rate calculation through the mean inverse speed [19]:

$$\eta(v_{min}) = \int_{v_{min}}^{\infty} \frac{f(\mathrm{v})}{v} d^3\mathrm{v}, \tag{1.10}$$

where $f(\mathrm{v})$ is the Boltzman velocity distribution of the halo.

1.6.2 Nuclear Form Factors

Since atomic nuclei are not featureless particles, as the momentum transfer between the WIMP and nuclei becomes large, approaching the de Broglie Wavelength $\lambda = h/q$ (where $q = 2\sqrt{m_N E_r}$ is smaller than the nucleus) the cross-section begins to decrease [64]. This reduction in the cross-section is formulated in a form factor $F(\mathrm{E_r})$. To first order, the form factor is derived from the Fourier transform of the mass density distribution $\rho(r)$ [64]. A slightly more advanced, but still analytic, form factor is typically used, called the Helm form factor and is given by:

$$F(qr_n) = 3\frac{J_1(qr_n)}{qr_n} e^{-(qs)^2/2}, \tag{1.11}$$

where s is an effective nuclear skin thickness. The first part of the Helm form factor is merely the solid spherical body form factor [65].

1.6.3 Energy Threshold

Since WIMPs would not be the only interactions observed in a detector (see the backgrounds sections below), a lower bound to the energy for the WIMP signal

must be set to continue to have good discrimination between the background and signal. This lower energy cutoff is called the threshold. The energy threshold is incorporated in the rate calculation by setting a minimum recoil cut off [19]. For higher energy thresholds, the minimum velocity increases for a given WIMP mass. The threshold causes a characteristic decrease in sensitivity for low mass WIMPs. Figure 1.8 shows basic shapes of the exclusion limit for various thresholds and target sizes.

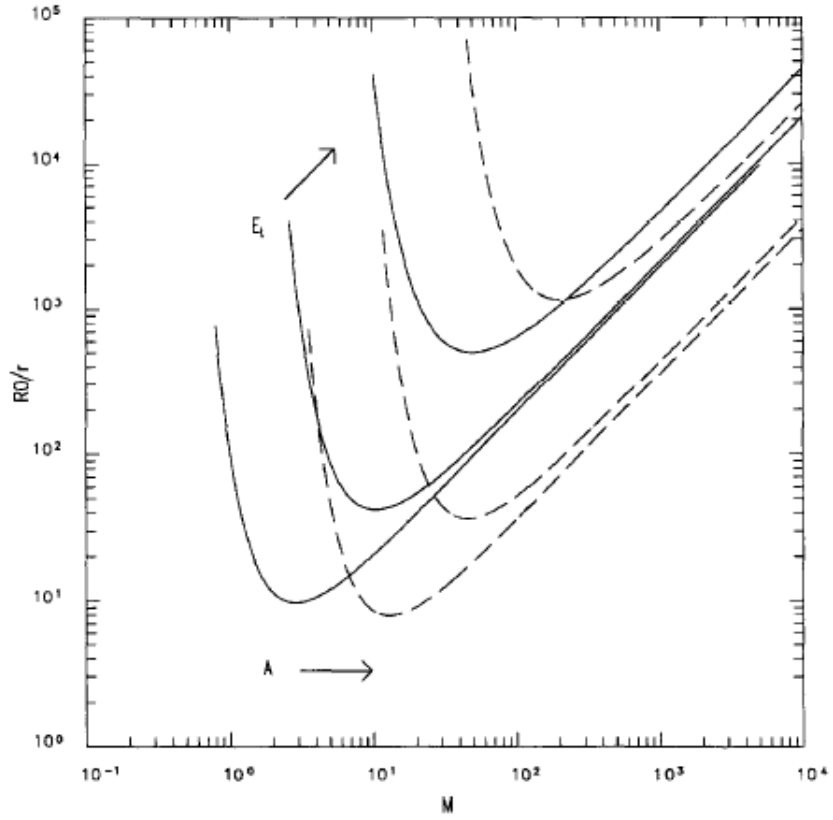

Figure 1.8: Typical shape of limit curves from direct detection experiments for a target with small atomic number A (solid) and large A (dotted) with increasing energy thresholds E_r.The X-axis is the mass of the WIMP and the Y-axis is the rate of interaction, relating to the WIMP-nucleon cross-section. The plot is taken from Ref. [64].

1.6.4 WIMP cross-section

For a given WIMP candidate from a specific SM extension, a WIMP-nucleon cross-section can be computed. However, in experimental searches, the cross-section is the derived quantity that is extracted from the measured event rate. As experiments continue to measure null rates with ever more massive detectors, the theories that predict large WIMP-nucleon cross-sections are ruled out.

1.6.5 Annual Modulation

As mentioned before, the motion of the Earth must be taken into consideration for the WIMP recoil rate. Due to the orbit of the Earth around the Sun, the Earth alternates between traveling with the WIMP wind with a decrease in the observed WIMP velocity and traveling against the WIMP wind, causing the opposite effect. The Earth's orbit would create a characteristic annual modulation in the WIMP signal. From the orbital direction of the Sun, the peak in the WIMP signal happens in July and minimum in December. This modulation is nearly sinusoidal with around a 5% decrease between max and min rates [64].

Chapter 2

DEAP-3600 Detector

The DEAP-3600 detector consists of 3260 kg of Liquid Argon (LAr) housed in an acrylic cryostat. In contrast to other detectors using Ar, DEAP is a single phase experiment meaning that only the scintillation signal is measured. The following sections will detail the physics of LAr scintillation as well as the physical design of the detector.

2.1 Liquid Argon Scintillation

In general, Noble elements are non-reactive and do not form strong molecular bonds with themselves or other atoms. Dimer states do form in LAr; however, in the ground state, the atoms are not strongly bound together. As particles travel through the LAr volume, they deposit energy into the LAr creating excited and ionized Ar atoms. When an Ar atom is excited or ionized, the attractive van der Waals force between the excited/ionized atom and a neutral Ar strengthens, and an excited dimer state forms. The dimer formation can

be created directly by excited Ar atoms via:

$$\begin{aligned} R^* + 2R &\rightarrow R_2^* + R, \\ R_2^* &\rightarrow 2R + h\nu + \text{heat} \end{aligned} \tag{2.1}$$

or through recombination for the ionized Ar atoms via:

$$\begin{aligned} R^+ + R &\rightarrow R_2^+, \\ R_2^+ + e^- &\rightarrow R^{**} + R, \\ R^{**} &\rightarrow R^* + \text{heat}, \\ R^* + 2R &\rightarrow R_2^* + R, \\ R_2^* &\rightarrow 2R + h\nu + \text{heat}. \end{aligned} \tag{2.2}$$

Here $*, +$ and $**$ refer to excitation, ionization, and excitation with vibration, respectively [66]. In both cases, the dimers decay back to the ground state by emitting a photon ($h\nu$) with a spectrum peaked at 128 nm with ~ 6 nm FWHM. In these equations we have explicitly mentioned heat in the end products of the decay due to a significant Stokes shift between the excited and ground states of the dimer. This Stokes shift is what makes Ar transparent to its own scintillation light [67]. Figure 2.1 shows an energy-level diagram for gaseous Ar dimer states. The excited dimers eventually settle into either the singlet or triplet states. The singlet has a short lifetime of $\sim$6 ns, while the triplet state requires a spin-orbit coupling to de-excite to the ground state [68] giving it a lifetime of $\sim$1400 ns [69]. These two states are not spectrally distin-

guishable. Figure 2.2 shows a combination of spectra measured for gaseous, liquid and solid Ar. There is very little agreement in the amplitude of the long wavelength section of the spectrum; without full information on the argon purity used in each measurement it is possible that impurities dominate at these wavelengths. This interpretation is reinforced by the observation of xenon lines at 149 nm and a broad feature around 197 nm that may be attributed to Oxygen [70] in a number of the spectra. The long wavelengths are left out when simulating LAr, as discussed in Chapter 7. By integrating the liquid Ar spectrum from 120 to 210 nm, the contribution from wavelengths above 135 nm is only $\sim 3.5\%$, which is negligible for events where less than 800 photons are detected.

2.1.1 Light Yield

The measure of the amount of light emitted by a scintillator per unit energy deposited is called the light yield (LY). Ar has a high LY, measured to be $55 \pm 8\gamma$ per keV of electronic excitation measured for heavy ion collisions [73]. At lower linear energy transfers (LETs) the LY has been measured to be ~40 γ/keV. This lower LY is expected to be due to the recombination efficiency at low LETs [74]. There are several other effects that quench the LY, namely:

- Nuclear quenching, when some fraction of the energy is carried away in the form of heat. The Lindhard Theory describes this quenching [75].
- Bi-excitation, where the collision of two excited argon atoms creates an electron-ion pair and a ground state argon atom: $Ar^* + Ar^* \rightarrow Ar + Ar^+ + e^-$ [76].

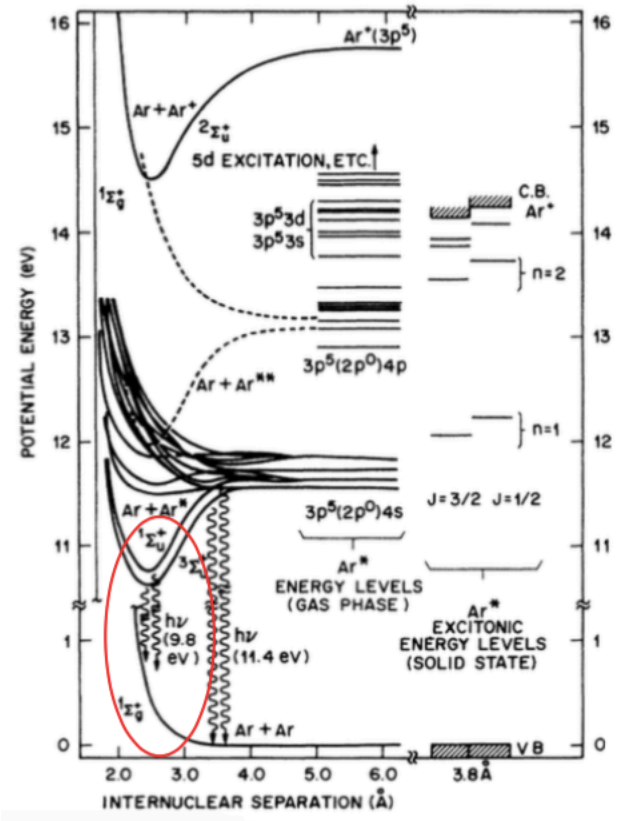

Figure 2.1: Inter-nuclear energy level diagram for gaseous Ar. The author indicates the singlet and triplet dimer de-excitations with the red outline. Plot taken from Ref. [71].

- The Penning process, where the collision of two excited dimers creates an ionized dimer and two unbound argon atoms via $Ar_2^* + Ar_2^* \rightarrow 2Ar + Ar_2^+ + e^-$ [77].

These effects quench the scintillation light production for high LET particle tracks like those from alphas, neutrons, and nuclei. The total quenching effect

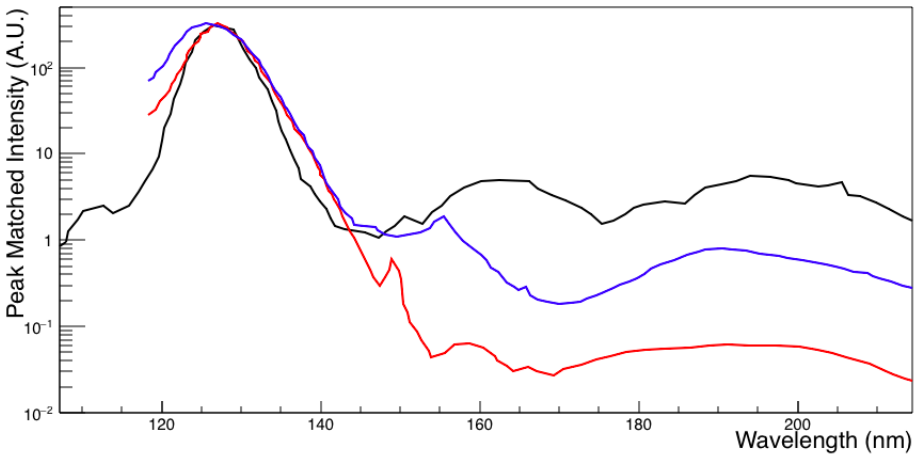

Figure 2.2: Measured spectra of Ar scintillation solid Ar (black) [71], liquid Ar (red) [72], and gaseous Ar (blue).

has been measured and is shown in Figure 2.3 reported at the ratio of LY for an electromagnetic interaction (LY_{em}) and a nuclear recoil interaction (LY_{nuc}). On average, for nuclear recoils the amount of scintillation light is $LY_{\text{nuc}} \sim 0.25 LY_{\text{em}}$.

Impurities within the Ar can also lead to a quenching of the measured scintillation light. The contaminants collide with the excited dimers that non-radiatively de-excite the dimer, causing a decrease in the measured lifetime of the state. Due to the long life of the triplet state, it is highly sensitive to impurities. As will be shown later, this is a direct method to monitor the contaminants in the LAr.

2.1.2 Pulse Shape Discrimination

What makes Ar an ideal target for DM searches, and possible to do a single phase experiment, is the fact that the population of the singlet and triplet

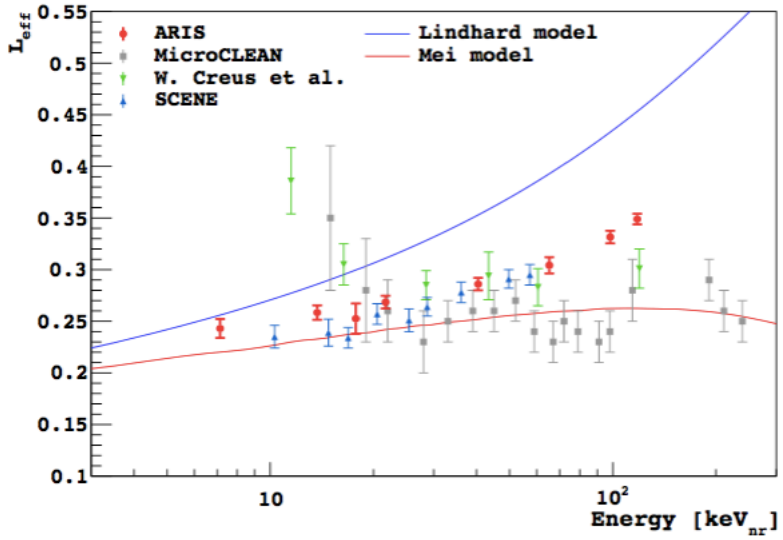

Figure 2.3: Light yield quenching dependence on NR energy in liquid argon as measured by the ARIS Collaboration and compared with other data sets and models. Plot taken from Ref. [78].

excited dimer states is highly dependent on the LET of the interacting particle [79]. In electromagnetic-type interactions, the LET is low and there is a preference for triplet states, giving a singlet and triple intensity ($I_{s,t}$) of $I_s/I_t \sim 0.26$. For nuclear recoils LET is high, $I_s/I_t \sim 3$. The large difference in the ratio of the states between the two event types, coupled with the large difference in lifetimes between the two states, is what allows for a discrimination between the two types of events in the WIMP region of interest. This is called Pulse Shape Discrimination (PSD). The PSD variable that DEAP uses to discriminate between the two types of events is fPrompt, defined as:

$$\text{fPrompt} = \frac{\int_{-28\text{ns}}^{t_{\text{prompt}}} I(t)}{\int_{-28ns}^{10000\text{ns}} I(t)}, \tag{2.3}$$

where t_{prompt} is the end time of a prompt window and $I(t)$ is the event's

measured time distribution of photon arrivals at the PMTs. The fPrompt variable will be further discussed in Section 9.3 for its formulation in this analysis.

2.2 Detector Design

The DEAP-3600 detector is a single phase liquid argon detector. Figure 2.4 shows a computer rendering of a cross-sectional view of the Vessel. At the heart of the detector is a 5 cm thick acrylic spherical vessel (AV) with an inner radius of ∼851 mm. At the top of the AV, there is a neck opening that connects to a long stainless steel section housing the cooling coils. The bottom of the neck is fitted with a flow guide to direct the flow of gaseous and LAr up through the cooling coil. There are 255 light guides (LGs) bonded to stubs on the AV's surface. The LGs couple the AV to the photomultiplier tubes (PMTs) that are used to detect the light generated in particle interactions. The bonding of the LGs will be discussed further in Chapter 3 and the PMTs in Section 2.2.4. Aluminized mylar is wrapped around the LG, to isolate each. On the outer surface of the AV, between the LGs, a layer of Tyvec$_{(\mathrm{TM})}$, is used to separate the inner AV from external light. The inter-LG spaces are filled with blocks consisting of alternating one-inch sheets of high-density polyethylene and polystyrene to provide extra shielding from neutrons. Polyurethane foam insulation is then used to fill in space at the ends of the filler blocks with a stainless steel mesh to stop the foam from moving. The entire detector is enclosed in a steel shell (SS) purged with radon scrubbed N_2 gas and submerged in a water tank. The SS is instrumented with 48 outward facing PMTs that

detect Cherenkov light generated in the water by muons and acts as a veto. The following sections will go into more detail about some of the aspects of the design and the construction of the detector.

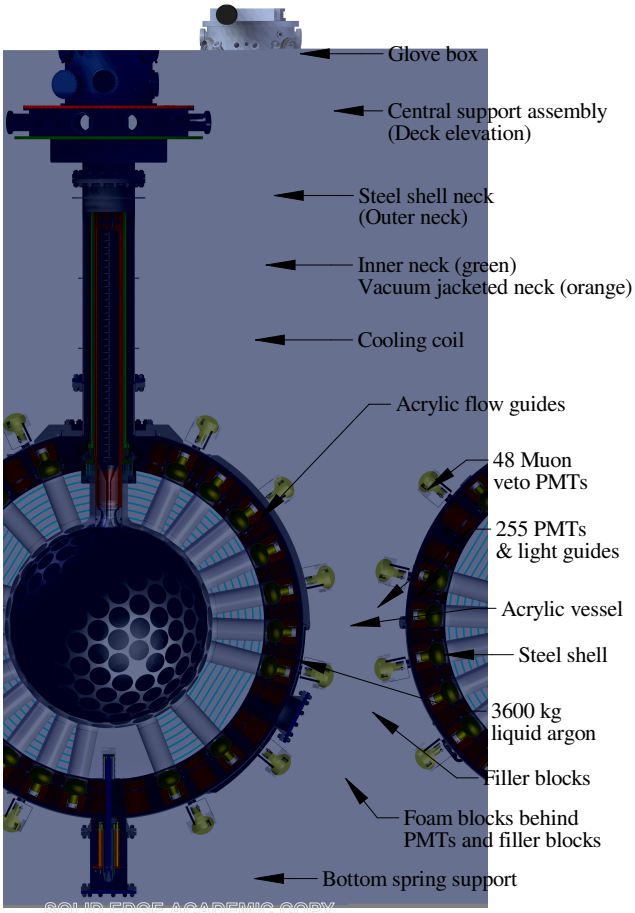

Figure 2.4: Computer rendering of a cross-sectional view of the DEAP-3600 detector. Plot taken from Ref. [80].

2.2.1 Acrylic Vessel

RPT Asia created the acrylic used in the fabrication of the main AV. The acrylic sheets were cast from a pure monomer in a low radon environment

to reduce contamination of radioactive isotopes. Typically, acrylic is cast with a mixture of monomer and dissolved polymer beads, used to catalyze the polymerization process. Air exposure of the polymer beads provides the primary source of the radioactive isotopes due to plating of radon daughters on the bead surfaces. A pure monomer cast allowed an acrylic bulk ^{210}Pb contamination of only 10^{-19} g/g, making this some of the most radioactively pure acrylic ever produced [81].

The acrylic sheets were transported to Grand Junction, Colorado where RPT thermoformed and machined them into spherical wedges. The wedge pieces were then bonded together to form the main shape of the AV. At the south pole of the AV, a circular plug was bonded to complete the sphere. The north pole of the AV (the top neck end) was left open, and a shoulder piece was formed as well as a neck block. Figure 2.5 shows the AV in Colorado during a dry fit of the five gore pieces before bonding. Due to the size constraints for bringing items into SNOLAB, the shoulder and neck pieces were not bonded to the AV until they arrived in the Cube Hall underground in SNOLAB. Before traveling underground, the acrylic pieces were shipped to the University of Alberta where they were machined on a large 5-axis mill to the desired shape, machining 255-25 mm long stubs for attaching the LGs onto the outer surface. Figure 2.6 shows the AV mounted on the mill during the facing of the AV stubs.

After any significant machining or bonding of the AV, the acrylic was thermally annealed to relieve stresses. The AV was annealed a total of 6 times. RPT performed the first anneal after bonding the main AV pieces. The AV was also annealed: after machining the LG stubs; after bonding the shoulder and

Figure 2.5: Photograph of the dry fit of the 5 acrylic gores that compose the main AV. Photo credit RPT.

neck pieces; after the onsite machining; and then one final time after all the LGs were bonded to the AV. For the last four anneals a custom built oven was used, consisting of two clamshells constructed of foam insulation panels held together with an exoskeleton made out of aluminum beams. The clamshells were attached to either side of a special support structure used to hold and maneuver the AV during the construction process. A closed loop forced air heater was then used to power the oven. The temperature control of the oven was performed using a custom program that used the input of 36 temperature sensors to monitor the average temperature as well as the temperature

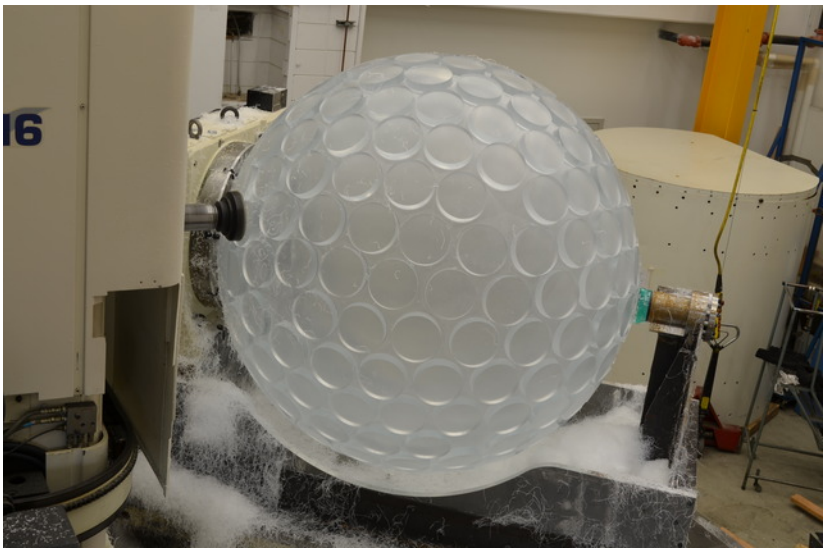

Figure 2.6: Photograph of the AV on the six-axis mill used to machine the AV.

uniformity. The program also monitored three temperature sensors embedded at different depths within an 8" test block used to gauge the temperature of the acrylic. Figure 2.7 shows the temperature cycle for a typical anneal. The radon levels in the air were monitored throughout the construction of the AV, the radon levels during an anneal is shown in Figure 2.7. For comparison, the circulated mine air has an activity of 129.5 ± 5.9 Bq/m^3 [82] and compressed air brought into the lab from the surface has an activity of 3.18 ± 0.15 Bq/m^3 [82]. This monitoring allowed an estimate of the concentration of radon daughters plating in the surface of the acrylic to be computed [83]. The plated daughters will slowly diffuse into the surface of the acrylic, at a rate of diffusion highly dependent on the temperature of the acrylic; the highest rates during the annealing cycles. Figure 2.8 shows the expected acrylic radioactivity as a function of surface depth. At the end of the AV construction, with the AV installed in its final location in SNOLAB and sealed from the

non-purified air, a robotic sanding arm was deployed into the AV to remove the inner 0.5 mm, the removed any of build-up surface contamination that would have diffused into the acrylic during the construction.

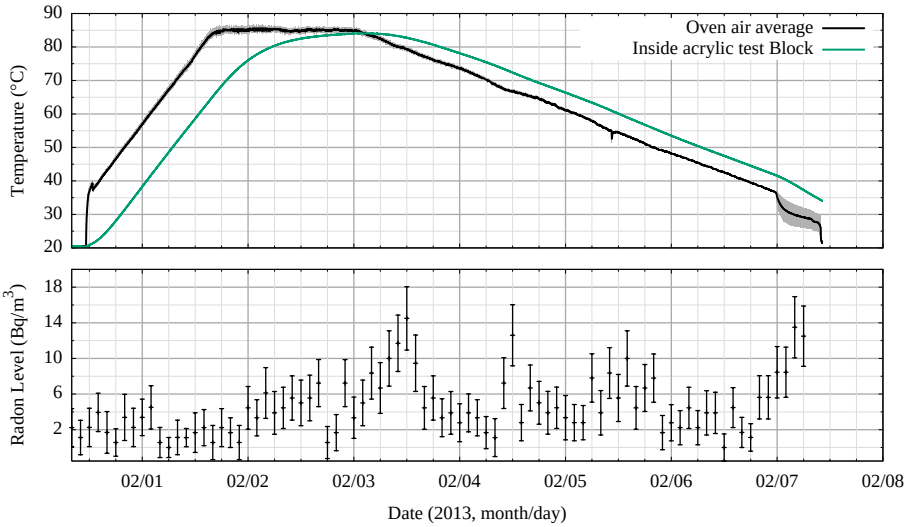

Figure 2.7: (Top) Temperature profile of an anneal of the detector. The average air temperature in the oven is shown (black) with the temperature at the centre of an acrylic test block used to estimate the temperature of the acrylic vessel (green). (Bottom) Radon activity measured in the gas inside the AV. Plot take from Ref. [84].

2.2.2 TPB

Acrylic is opaque to UV light, as is the glass of the PMTs. The wavelength of the Ar scintillation photons is shifted to the visible range to propagate the photon signal through the AV. The wavelength shifting is performed using an organic wavelength shifter called Tetraphenyl-Butadiene (TPB). After the inner surface of the AV was sanded, the acrylic was baked and put under vacuum to remove excess moisture and gasses. TPB was then evaporatively transferred to the surface of the acrylic by loading the heater used in the

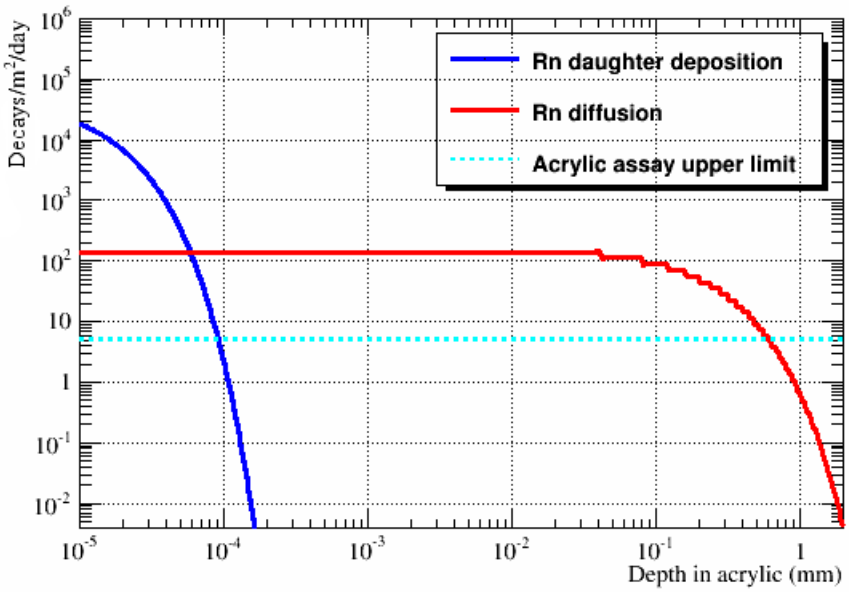

Figure 2.8: The expected ^{210}Pb activity as a function of acrylic depth before the AV resurfacing. Plot take from Ref. [80].

bake-out with TPB and evaporating it within the detector under vacuum. The deposition was performed in two stages, with a ∼1.5 μm thickness of TPB deposited at each stage [85]. The emission spectrum for TPB is shown in Figure 2.9 along side the Transmission amplitude through the LG and the quantum efficiency (QE) of the photomultiplier tubes (PMTs). The optical properties of the TPB material will be discussed in Chapter 7.

2.2.3 Ultrapure LAr

The AV is filled with ∼3257 kg of ultra-pure LAr. Before injecting the Ar into the detector, it is sent through a purification system that removes impurities down to sub-ppb levels of electronegative impurities (CH_4, CO, CO_2,

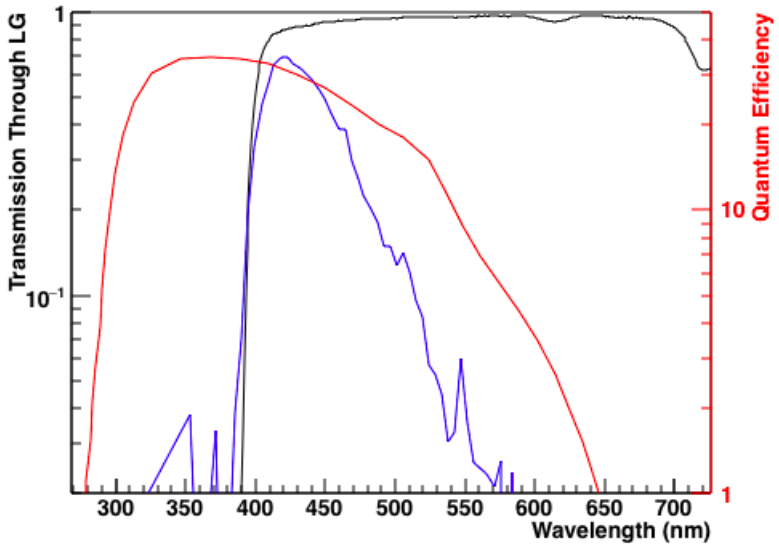

Figure 2.9: The emission spectrum of TPB for 128 nm excitation (blue) [86] is shown along with the transmission through the light guide (black) computed from the data in Ref. [87]. The quantum efficiency of the photomultiplier tubes [88].

H_2, H_2O, N_2 and O_2) [80]. The first step in this process is a SAES Mega-Torr PS5-MGT15 hot metal getter. This getter was custom for DEAP with the criteria that no thoriated welds were used. The next stage in the purification system is a radon trap to scrub the Ar of radon reducing the radon activity to nearly 5 μBq [80]. The detector was then filled from October through November 2016. Since then, the purity of the LAr has been monitored by measuring the stability of the long time component in the Ar scintillation signal. Figure 2.10 shows the stability of the long time component over the last year of running demonstrating only a couple of percent of degradation not visible in Figure 2.10. To date, no Ar re-purification has been required.

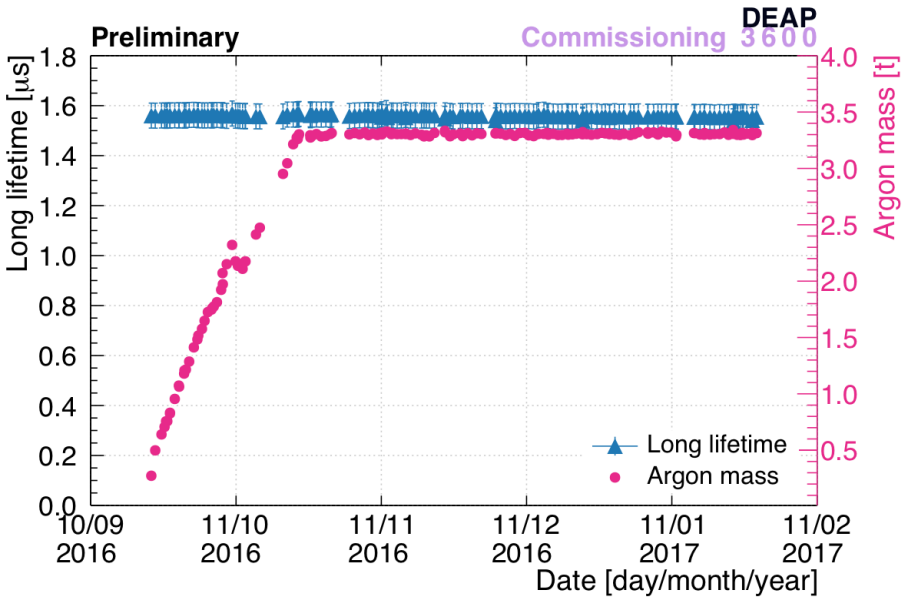

Figure 2.10: Measurement of the long component of the Ar scintillation signal; directly related to the triplet lifetime. The stability is used as a metric for the purity of the LAr. No significant signs of signal degradation have been observed. Plot created by Tina Pollmann.

2.2.4 Photomultiplier Tubes

Photons are detected in DEAP-3600 using Hamamatsu R5912 HQE 8" photomultiplier tubes (PMTs). A photon incident on the PMT's photocathode releases an electron via the photoelectric effect [89]. This electron, referred to as a photo-electron (PE), is accelerated to the dynode stack of the PMT with an internal electric field. This is illustrated in Figure 2.11. The R5912 PMTs have 12 stages in the dynode stack. At each step in the stack, electrons are accelerated and strike a dynode plate releasing more electrons. At the anode, the electron multiplication is $\sim 10^7$, and the photon is detected. Figure 2.9 shows the QE of the PMTs.

The electric pulse from the PMT is amplified and shaped with a custom

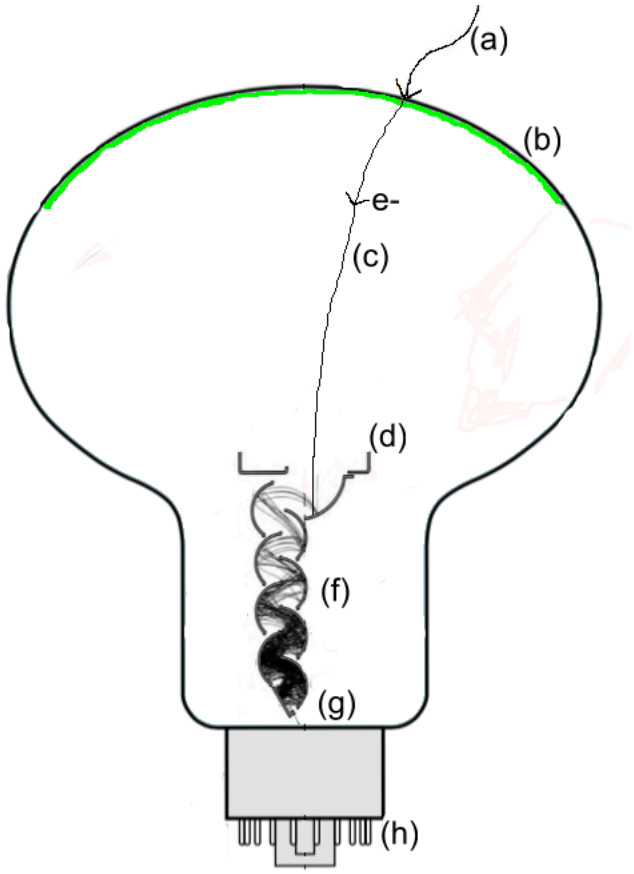

Figure 2.11: Illustraction of the basic process that happens within a PMT when a photon is detected.Shown is the process of an incident photon (a) striking the photocathode (green,b), this results in a photo-electron (c). The electron is accelerated towards the dynode stack (f), focused towards the first dynode by the focusing electrodes (d). The electrons impacting the dynodes causing multiple electrons to be released. The resulting electric signal is collected a the anode (f). The Illustration was created using components of multiple PMT diagrams in [88] and [90].

signal conditioning board (SCB). Without the SCB, the pulse is relatively sharp, ∼10 ns wide. The SCB stretches the pulse to a width of around 20 ns to permit a proper measurement of the charge to be made with the CAEN V1720 digitizers.

CAEN V1720 digitizers sample the PMT signals and create a digitized trace with 12-bit precision (4096 discrete voltage values, referred here as an

analog-to-digital unit (ADC)). The range of the digitizers is set from -2V to +0.5V so that the 0V baseline has value of 3900 ADC. The pulses appear as downwards peaks in the digitized waveform, discussed in Chapter 5. The digitizers record the data with Zero Length Encoding (ZLE) to reduce the file size (ZLE only saves the sections of the digitized waveform that are within 16 samples of a 5 ADC threshold crossing below the baseline).

A set of CAEN V1740 digitizers are used to measure a low gain output of the SCB. This signal is used if a PMT sees a significant amount of light that causes the V1720 digitizer to clip (reads a voltage over 2V), losing the full charge information of the pulse. At this stage of the detector operation, corrections to the energy using the V1740 digitizers have not be implemented; this correction is, however, being formulated and tested.

The SCB also has an output that is the sum of the boards ten input channels. The summed signals from all SCB boards are again summed and sent to an FPGA used as a digitizer and trigger module (DTM). The DTM uses the summed signal to determine if one of the trigger conditions have been satisfied and sends a signal to the digitizers to save the digitized waveforms. More information on the types of triggers for the physics data taking will be discussed in Section 4.1. Figure 2.12 shows a schematic of the data acquisition (DAQ).

2.2.5 Neck Veto

Surrounding the outer acrylic of the AV's neck is a Neck Veto detector. The Neck Veto consists of two bundles of 50-2 m long Kuraray Y-11 wavelength

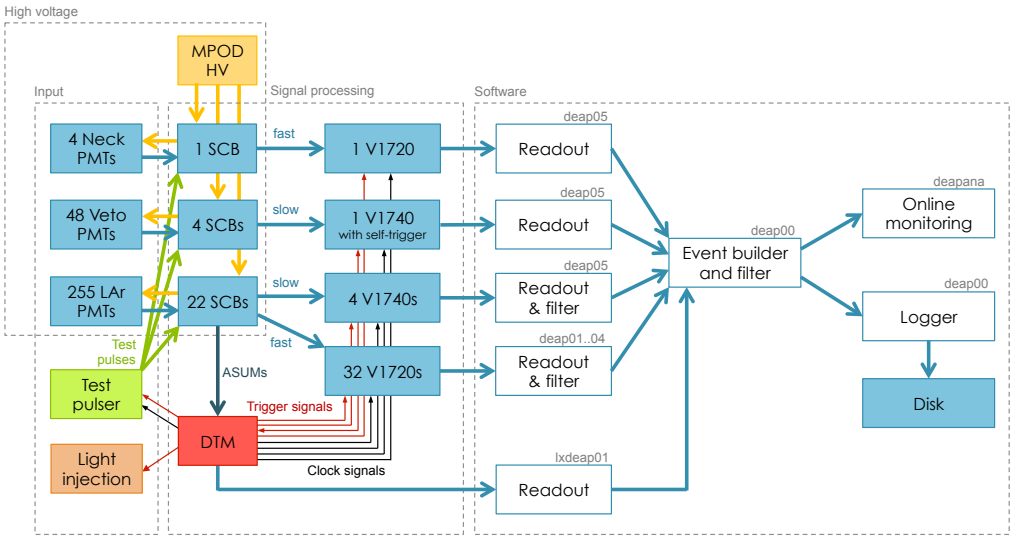

Figure 2.12: Diagram of the data acquisition system used in DEAP. Plot taken from Ref. [84].

shifting optical fibres wrapped around the bottom ∼10 cm of the neck. The fibre bundles terminate on either end at a 1" square R7600-300 Hamamatsu PMT. For light generated in the neck region of the detector, some fraction may escape out the neck piece of the AV and enter the optical fibres. When the light is wavelength shifted in the fibre, a fraction of this light travels done the fibre and is measured by the PMTs. The neck veto is intended to aid in discriminating events that occur in the inner neck area. This veto was originally designed for the case where the inner neck and flow guides would be coated with TPB. However, even without TPB on the neck parts, the veto continues to be an effective veto for Cherenkov events that occur in the neck acrylic.

2.2.6 Water Tank and Muon Veto

The entire DEAP-3600 detector is located in a stainless steel vessel and submerged in a water tank. The outer surface of the SS is instrumented with 48 Hamamatsu R1408 PMTs (recycled from the SNO experiment) that detect Cherenkov light from muons propagating through the water tank. The water tank also shields the detector from external gamma rays and neutrons. Figure 2.13 shows the measured rate of Cherenkov events occurring in the LGs due to gamma interactions while the AV was empty. As the level of water in the tank rises past the neck, the rate of gamma ray interactions decrease to that expected from the internal gamma ray sources.

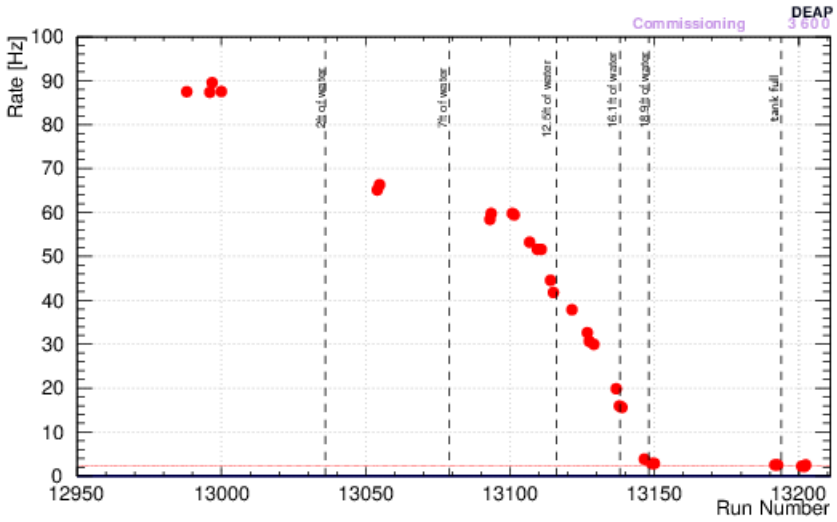

Figure 2.13: Gamma activity measured in the empty detector while the water tank was being filled. Plot courtesy of James Bueno.

2.2.7 Calibration Sources

DEAP-3600 takes two types of calibration data: optical calibration consists of injecting known amounts of light into the detector; and radioactive calibration,

where a radioactive source is brought close to the detector. The following sections will discuss some of the key calibration sources.

Optical Calibration

Optical calibrations are used to characterize the physical optics of the detector as well as calibrate the PMT responses. There are two optical calibration sources that DEAP uses to describe and monitor the detector. The first is a nearly isotropic laserball source that was deployed into the AV before installing the neck cooling coils. A second system is a series of optical fibres coupled to the LGs connected to a light emitting diode (LED) driver. This LED injection system is periodically used throughout the detector operation to monitor the response of the PMTs and optical properties of the detector. These optical calibration sources will be further explained in the next two sections.

Laserball Directly after the TPB deposition, a laserball source was deployed into the detector to give a fast time pulse of light at 445 nm to calibrate the PMT timing and relative efficiencies. The laserball consists of an 11 cm in diameter PerFluoroAlkoxy (PFA) flask loaded with quartz beads suspended in silicone gel to scatter light emitted into the flask through a 1-mm diameter optical fibre fed through the top of the flask. The fibre is coupled on the opposite end to a Hamamatsu PLP-10 picosecond light pulser. Multiple laser diode heads could be attached to the light pulser. The primary calibration is done with the 445 nm head. Additional data were taken at 375 nm, which is a short enough wavelength to excite and TPB.

LED Fibre Injection There are a series of 22 optical fibres attached to 20 LGs, with two connected to the AV neck in two locations. These fibres couple to a fast LED driver on the external end. The attachment to the LG is at the PMT with the cone of light directed to hit within 1 cm of the centre of the PMT as shown in Figure 2.14. Each fibre is independently flashed creating an isotropic light source for PMTs that are more than 50° from the injection position. This optical calibration is most commonly used to monitor the PMT gains and efficiencies. Calibration runs of at least 3 LEDs are run on a daily basis. The LED data has also been used to tune the optical model (as discussed in Chapter 7).

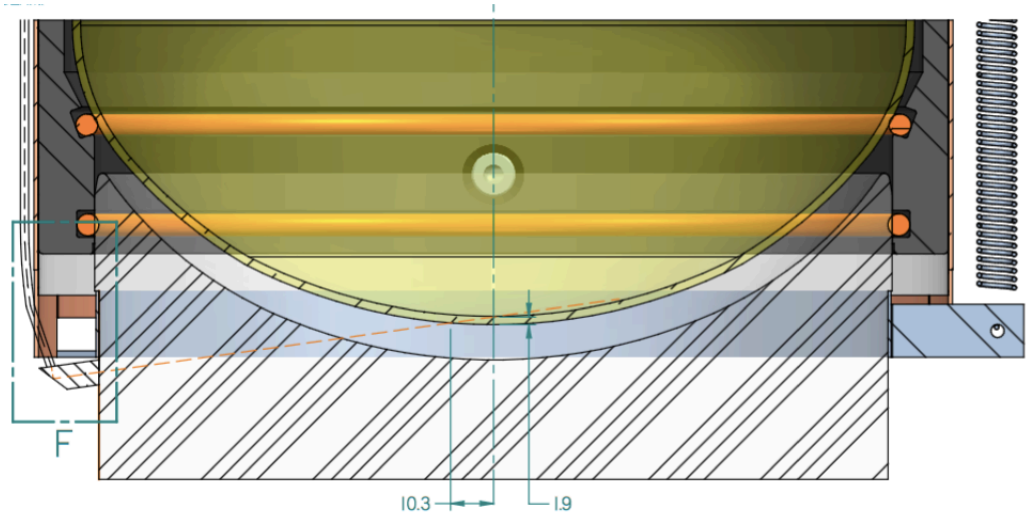

Figure 2.14: Diagram showing the orientation of one of the fibre attachments at the end of the LG. The optical fibre can be seen on the left coupling the the light guide with an acrylic block with an aluminum reflector. The light emerging from the fibre is aimed to hit the PMT within 1 cm of the centre position. Diagram provided by Koby Dering.

Radioactive Sources

Radioactive sources are used to bombard the detector with particles of known origin and energy. This bombardment is used to calibrate the energy response of the detector, as well as the detector's response to nuclear recoils. Radioactive sources are deployed from outside the steel shell to avoid the risk of contaminating the inner LAr. Source deployment is performed by lowering the radioactive source into one of the five calibration tubes. The calibration tubes are shown in Figure 2.15. The detector also has a natural radioactive source of ^{39}Ar decays. Due to the significant rate of ^{39}Ar decays, this is the primary source for studying the detector's response. External radioactive sources are then used to give extra information to reduce correlations in the detector's response function as well as probe the response of the detector to nuclear recoil events within the energy region used for the WIMP search, referred to as the WIMP region of interest (ROI). The next two sections discuss the primary external radioactive sources used to calibrate the detector.

^{22}Na Source The ^{22}Na source is periodically deployed to obtain a secondary measurement of the energy response. ^{22}Na is a $+\beta$ emitter, decaying to an excited state is ^{22}Ne. The ^{22}Ne then de-excites, emitting a 1.2 MeV gamma. The e^+ emitted from the ^{22}Na quickly annihilates with an electron creating two 511 keV gamma rays, emitted back-to-back. The canister used to hold the source and deploy it into the calibration tubes is instrumented with two Hamamatsu R9880U PMTs coupled to two LYSO scintillator crystals. The PMT assemblies sandwich the ^{22}Na source, acting as a tagging system and allowing for only events that see a decay within the source PMTs and the de-

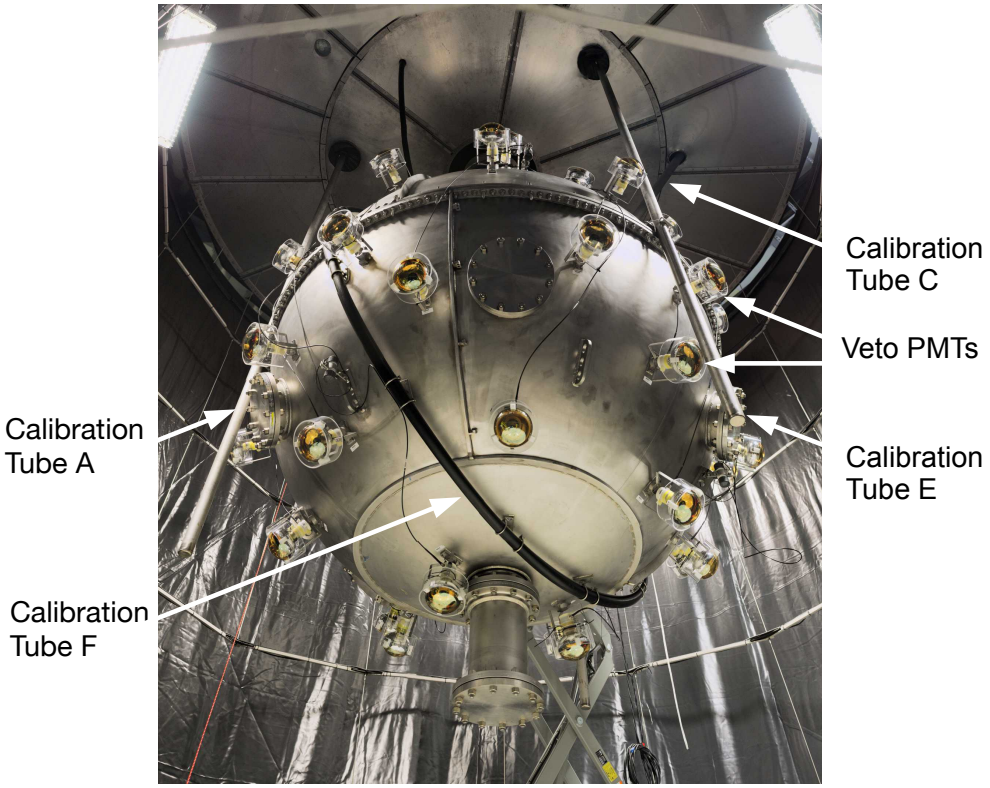

Figure 2.15: Photograph of the detector encased in the SS with the calibration tubes labelled. Photograph taken from Ref. [80].

tector PMTs to be selected. This reduces the calibration signal contamination from ^{39}Ar events. The ^{22}Na source activity is 3.7 MBq. The MC simulations give the expected rate of double-tagged events within the detector to be 1.2 kHz with a background rate of 0.032 kHz due to accidental coincidences with ^{39}Ar.

AmBe Source The detector has been designed to remove as many sources of radioactivity as possible that could produce a nuclear recoil within the WIMP ROI. A neutron source is deployed into the calibration tubes to calibrate the response of the detector to nuclear recoils. The neutrons from the source are

produced through (α, n) interactions in ^{9}Be where the αs are provided through the decay of Am. A high source strength of 74 MBq is required to calibrate the response of the detector to nuclear recoils. Due to the massive amounts of plastic shielding around the detector, only 0.023% of the emitted neutrons deposit energy in the LAr, with only 0.008% having recoil energy greater than 50 keV [91]. This low probability gives a rate of 0.4 Hz of neutrons with recoils that enter the WIMP energy ROI. The source doesn't only produce neutrons; there are also many gamma rays that are emitted. The highest energy gamma ray being the 4.44 MeV being from the de-excitation of the ^{12}C atom created after the α-capture on ^{9}Be and emission of a neutron. There are also some other gammas that come from the NaCl crystal used in the source's tagging system, as well as gamma rays that are created from the capture of neutrons as they travel towards the detector. If the neutron enters the LAr, it will likely scatter multiple times. These multi-scatter interactions make it difficult to directly relate the neutron signal directly back to a pure nuclear recoil without the use of a simulation of the detector. A sample of the neutron calibration data will be discussed in Section 9.2.

2.3 Backgrounds

The detector material selection and the overall detector design were performed to mitigate sources of background events that may leak into the WIMP signal region. By design, less than 0.2 background events are expected in the full three-year data set. The following section will introduce the backgrounds that may produce signals in the WIMP ROI.

2.3.1 ^{39}Ar

As mentioned, natural Ar has a trace amount of isotope ^{39}Ar, the activity of natural Ar is 1.01±0.02(stat)±0.08(syst) Bq per kg [92]. This isotope is a β emitter, creating electromagnetic-type events within the detector. At high energies these events are not an issue and are easily separable from the nuclear recoil events. However, for β-decays with energy $\lesssim$ 15 keV, the separation of the event through PSD becomes less well defined. The ^{39}Ar low-energy leakage into the nuclear recoil band is what limits Ar-based experiments from reducing the detector threshold to look at sub-20-GeV WIMP mass. There is considerable effort in the Ar community to develop methods of extracting Ar from underground sources where it is not cosmogenically activated and the majority of the ^{39}Ar has decayed away [93].

Cherenkov Events

A secondary type of background that creates events in the WIMP ROI from low-energy leakage are LG Cherenkov events. Cherenkov light is generated when a particle travels faster within a medium than the phase velocity of light within a range of wavelengths [94]. This light is produced instantaneously along the particle's track. In a perfect detector, this would create an event with fPrompt=1.0. Due to PMT effects, however, such as afterpulsing, Cherenkov events can get pulled down into the nuclear recoil fPrompt region. Pure Cherenkov events are distinguishable from WIMP-like interactions due to the correlation between the early and late light in the events. Since afterpulsing generates all light in the late times of the event, there is a strong

correlation between the PMTs that see prompt and late light. In a WIMP-like event, some of the late light is due to uncorrelated triplet decays of Ar dimmers. This method, to separate the Cherenkov events via correlations, works well up to ∼100 photon events. As will be discussed in Chapter 8, no LG Cherenkov or pile-up of LG Cherenkov and ^{39}Ar is expected in the data set due to the MultiSite processor.

2.3.2 Surface Alphas

One of the primary tasks in the design and construction of the detector is selecting materials that are low in ^{238}U and ^{232}Th, as well as limiting the inner detector surfaces to exposure to Radon. This effort aims to reduce the number of α-decays within the active volume of the detector. As mentioned, this is why the acrylic vessel was resurfaced after the construction completion. Despite all of the care taken to reduce the U/Th contaminants in the materials, there persist trace amounts. Isotopes that α-decay and fully deposit the energy within the LAr are not a significant problem for the WIMP search; the alphas emitted in the decays are in the MeV energy range and will produce many thousands of photons, while WIMPs are expected to only generate a couple hundred photons. What is an issue for DEAP are α-decays that only deposit part of their energy within the LAr. This degraded deposition can occur if the α-decay happens within the TPB layer or a thin layer of acrylic on the inner acrylic surface. Figure 2.16 illustrates the scenarios where the measured scintillation is degraded due to partial or full energy deposition in materials other than the LAr. The events are numbered in order of increasing

light output. Because all of these events are happening on the surface of the LAr, they may be removed by select events with a high radius reconstructed vertex. Without a well-known position resolution at the outer radius and a good model for TPB scintillation, predicting the leakage becomes difficult. For this analysis, this will only be done qualitatively by verifying that any remaining events are inconsistent with leakage from events at high radii.

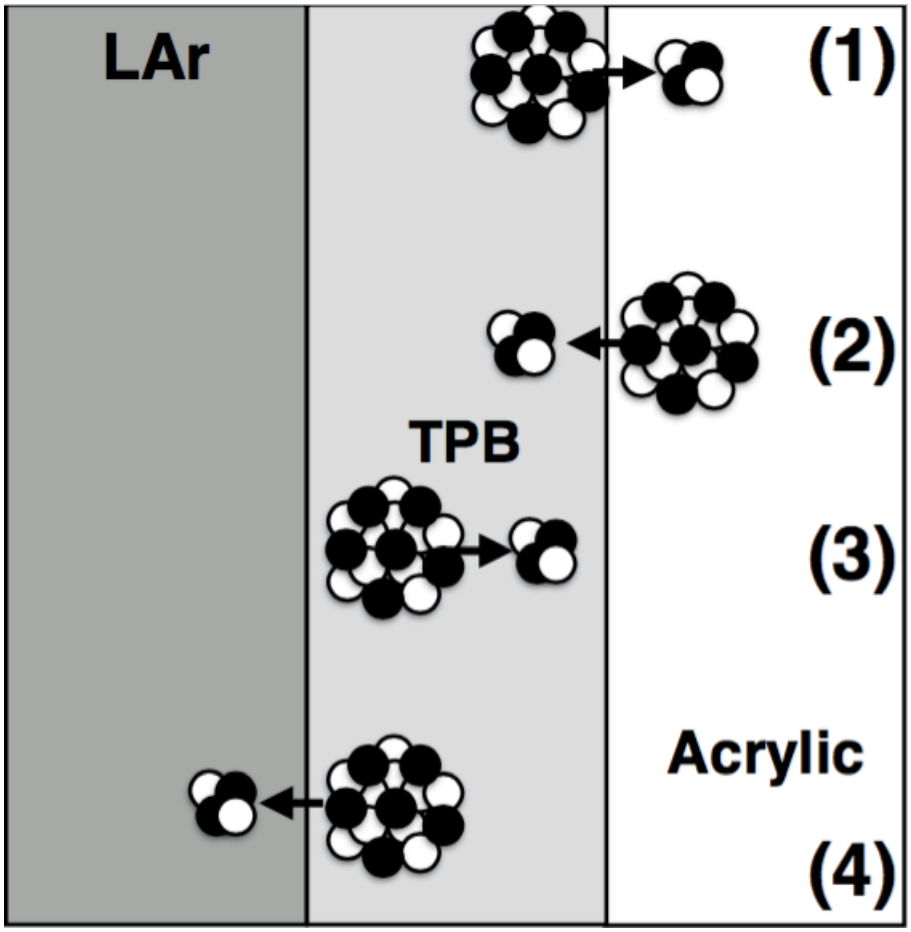

Figure 2.16: Diagram of various α-decay scenarios that would cause a degradation of the measured energy. Decays are arranged in order of the amount of light that would be given off.

Neutrons

Neutrons primarily elastically scatter off Ar nuclei, mimicking the expected WIMP signal. There are several sources of neutrons but the primary two that are substantial issues for DEAP are neutrons created by cosmogenic muons, and those produced through (α, n) interactions within detector materials. For the cosmogenically created neutrons, the most powerful method to remove them is tagging the muon that creates the neutron. This is done through the muon veto that surrounds nearly the whole detector. The second source of neutrons, radiogenically created, are much harder to remove from data. To reduce the impact that these neutrons have on the analysis, the detector was built with large amounts of plastic to thermalize the neutrons, and bring them to a low enough energy that they do not enter the signal region for the WIMP. Plastics can efficiently thermalize the neutrons due to the abundance of hydrogen atoms in the material. Hydrogen nuclei are kinematically optimal for maximizing the momentum transfer in nuclear collisions. With this massive amount of shielding, the primary sources of radiogenic neutrons that significantly contribute to the detector backgrounds are from the materials closest to the LAr: PMTs, filler blocks and acrylic. The number of neutrons is proportional to the radioactivity of the material; this makes the PMTs the most significant source of neutrons. The glass used to make PMTs necessarily contains radio-impurities with a relatively large amount of ^{232}Th. In total $\sim$5 neutron is expected within the WIMP ROI per year using the results from [95] with no vertex position cut. The 0.5-m length of the LGs was selected to sufficiently thermalize the neutrons coming from the PMT glass. One additional

discrimination that we have on removing neutrons and placing an upper limit on the number of neutrons in the final data set is through gamma tagging. As neutrons scatter within the detector they lose energy and eventually become thermalized. Once thermalized the neutron can be captured by a nucleus that emits a gamma ray in the process. By tagging events that have a gamma follower, neutron captures can be counted/removed from data. Gamma tagging has $\sim 30\%$ efficiency and will be discussed later in Chapter 9.

2.4 Detector Simulation and Data Structure

A Monte Carlo (MC) simulation was built using the Reactor Analysis Tool (RAT) software package developed by the Braidwood neutrino experiment [96]. At the heart of RAT is GEANT4, which performs all of the particle tracking and interaction computations [97]. Built on top of the GEANT4 simulation, is a simulation of our electronics and DAQ. The last aspect of the RAT program is the analysis of the data. RAT not only processes the data generated in the GEANT4 simulation but also data from the physical detector. The analysis of the data is divided into modules called processors; each performs a computation on the data and stores the output into the data structure (DS). The DS is a large C++ class built using the ROOT libraries [98]. The DS contains many subclasses that split the information about an event into subcategories including:

- MC: Contains the Monte Carlo information for GEANT4 produced data.
- TS: Trigger summary information; contains information about the event

from the DTM.

- RAW: The raw data consists of the PMT voltage traces produced by the digitizers and basic PMT pulse information generated in the frontend.
- CAL: The calibrated analysis of variables including; the processed raw PMT voltage traces in terms of pulse times and charges.
- EV: The event class; containing outputs from high-level analysis such as position fitters.

The DS is structured in such a way that we can selectively save specific parts into files using a ROOT [98] format called TTrees [99]. In the standard processing scheme, the detector's data is first saved with only the RAW and TS information, followed by a file containing the CAL and EV information that has been reduced by removing the PMT pulse information once the event has been processed. There is a database of detector information that is read by RAT to retrieve the detector configuration at the time of a run. The database is also used when generating MC data to simulate specific detector configurations, allowing better comparisons between detector data and MC data.

Chapter 3

Light Guide Bonding

The LGs are an integral part of the design of the DEAP detector. They allow the PMTs to operate at a warmer temperature than the cryogenic LAr [60] [100]. The 0.5-m of acrylic provides necessary shielding from neutrons that are created in the PMT glass through (α, n) interactions. The attachment of the LG; however, was a major R&D project with many non-trivial aspects. This chapter will go through the development of the method and implementation for attaching the LGs to the AV.

3.1 Light Guides

The DEAP LGs are made out of two 4 inch thick acrylic pieces that are bonded together to make a rectangular piece with a cross-section 20.5 x 20.5 cm^2. These pieces were machined at the Tri-University Meson Facility (TRIUMF) to the required dimensions as shown in Figure 3.1. The concavity on the back of the LG allows for better coupling to the convex PMT windows.

The LG length is sufficient to thermalize neutrons coming from the PMT as well as reduce the thermal gradient so the PMT can be held at -20°C without large thermal stress. After machining, the LG were annealed with a standard annealing cycle [101]. The final weight of each LG is $\sim$ 14 kg.

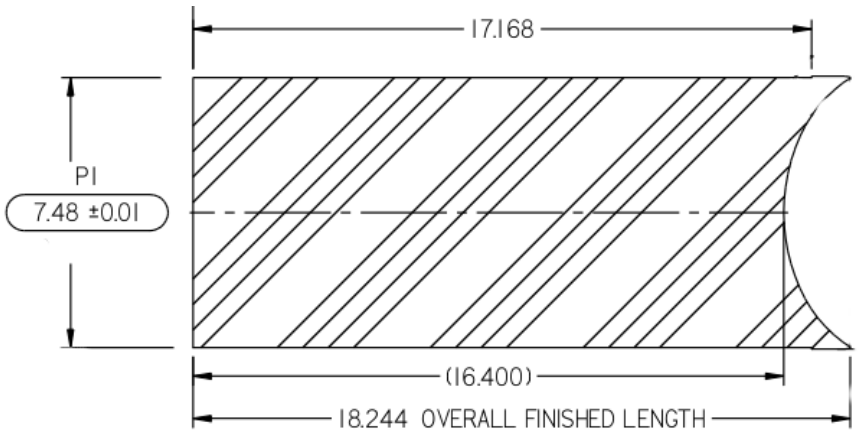

Figure 3.1: Diagram of the DEAP-3600 light guides. The concavity on the right is to couple the LG to the curvature of the photomultiplier tube. Dimensions are in inches. Figure from Ref. [102].

3.2 LG Attachment

There are several factors that influenced the decision to bond the LG to the AV verses a clamping attachment system. Firstly, bonding the LGs greatly increased the structural stability of the detector. SNOLAB is located within an active mine that experiences occasional rock quakes with the potential to introduce large forces on the vessel. Bonding the LGs to the acrylic vessel greatly increased the rigidity of the detector and kept the LGs from shifting during such an event.

The second factor arises from optical simulations showing that even with

the LGs fully pushed together, the light yield decreases by 50%. Figure 3.2 shows the reduction as a function of the air gap. Due to the cryogenic temperatures at the base of the LGs, optical coupling gels were are not a viable solution for improving the transmittance through the boundary.

Calculations of the stresses caused by the differential thermal expansion across the bond show that even a small difference in thermal expansion between the acrylic and bond material causes a significant amount of stress after the cool-down of the detector. To avoid this, the LGs were bonded using a methyl methacrylate (MMA) and poly-methyl methacrylate (PMMA) mixture to match the composition of the parent acrylic.

3.3 Thermal Stresses

The operating temperature of the DEAP detector is $\sim -188 \pm 2$°C. On the PMT end, the LGs will be at ~ -20°C. During steady state operation the thermal gradient along the LG is ~ 0.3 °C/mm. Finite element analysis show a peak stress of 1.5 MPa within the LG bond. The bonds connecting the 5 acrylic sections making the AV have a peak stress of 9.36 MPa. Initial tests performed at Los Alamos National Lab (LANL) showed that, at -196°C, the average tensile strength of acrylic is 129 MPa and that the RPT test bonds failed at 106.4 MPa [103]. This allowed for a large safety factor. The lower average tensile strength in the bond material is expected to be caused by intrinsic stress that is created during the polymerization of the bond material. Due to slight differences in polymerization rates through the bond, sections of the bond may be left in compression and others in tension, slightly weakening

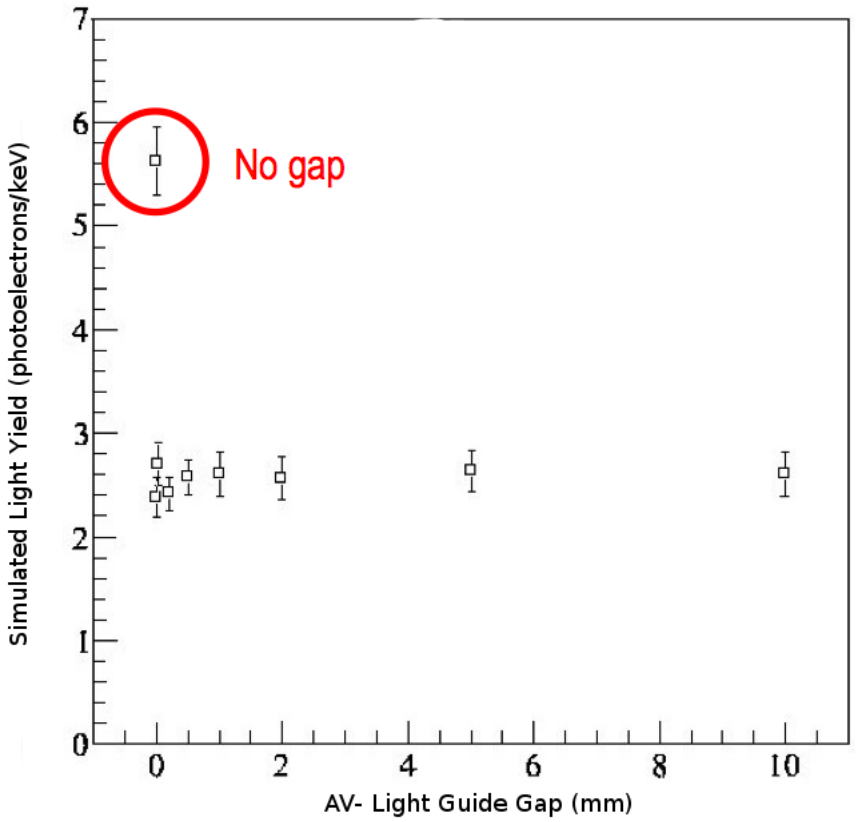

Figure 3.2: Initial simulations of light yield at different air gaps between the LG and the main AV. Plot provided by Eric Vazquez-Jauregui. Note: the light yield value does not represent the light yield in DEAP-3600.

the bond material.

3.4 Tests and Development

To test the feasibility of creating LG acrylic bonds that withstand the thermal stresses experienced within the DEAP detector, bond tests were performed at the University of Alberta. Bonds were created with two $\frac{1}{2}$" thick acrylic disks with a diameter matching the LG. There are several setups used to perform test bonds; however, they are all centred around two general ideas.

The first setup was a static fill where the gap and uniformity were strongly constrained and did not rely on the fill pressure and duration. With these bonds, the optimal gap and glue composition were identified. The next steps were a gradual progression from the static fill to a dynamic fill, where the bond thickness was controlled by the amount of syrup (see next Section) injected into the bond. These tests were directly testing the method used to bond the actual LG to the AV.

3.4.1 Bonding Syrup

The bonding syrup for the DEAP-3600 LG bonding consists of a mixture of MMA and PMMA. The ratio of these two components affects both the polymerization (kick) time as well as the viscosity of the syrup. The optimal viscosity is chosen to give the desired flow rate through $\frac{1}{4}$"(0.17"inside diameter) tubing. This allows bonds to be filled with syrup in $\sim$30 minutes from the start of the syrup push to the point that the target bond thickness was reached. It was observed that the properties of the syrup are dependant on the manufactures. Using MMA and PMMA from Polysciences, Inc. (080-62-6, 9011-14-7) a 70/30 mixture by weight gave the desired viscosity. For the final bond tests, the MMA and PMMA was selected to match that used for the RPT AV bonds (Lucite MMA, Lucite 6751 Resin). With the new compounds, the mixture had to be readjusted to 84/16 to obtain to the desired viscosity.

To speedup and improve the polymerization of the syrup, an initiator is added to the mixture. In order to have the bonds polymerize between bonding shifts, 2.5% by weight of Perkadox-16 was added to the base syrup as a cata-

lyst. With this glue mixture and the bond parameters described in following sections, bonds begin to polymerize in ~ 8 hours at 22ºC.

For the LG bonding, the bonding syrup was mixed on surface in the SNOLAB clean room environment. On surface and underground, the glue was stored in freezers (~ -10°C). It was found that storing the syrup this way almost entirely arrested the polymerization process. The syrup was transported underground in a cooler filled with ice over the span of 1 day. It was observed that 1 day at 0° C was roughly equivalent to 1 hour at ~ 22°C for the polymerization of the syrup.

3.4.2 Bond Thickness and Uniformity

There are several considerations that needed to be taken into account when working out the optimal thickness of the bond. Polymerization is an exothermic reaction. If too much syrup was injected in the bond, the MMA could over heat and vaporize, leaving voids in the bond [104]. The bond gap can't be made arbitrarily thin, it needs to be thick enough to afford variations in thickness over the bonding surface. This affects the intrinsic stress in the bond. For the DEAP LG bonding, a goal of ± 0.5 mm uniformity in bond gap over the full area of the bond was made based constraints on the bond equipment capable of achieving. The bond tests showed that with this uniformity, a bond with average thickness of 2.50 ± 0.25 mm was optimal for strong bonds without voids.

3.4.3 Bulge and Removal

It is important to allow a reservoir of syrup around the edges of the bond that allows glue to flow into the bond as the syrup shrinks during polymerization [101]. At the end of the process, the bond must be annealed to normalize the amount of stress over the bond area. A 2-3 mm radial bulge around the outside of the bond area also helps the stress to emerge from the primary bond area. Once the bond has been annealed, the bulge can be removed to eliminate of the high-stress boundary layer [101]. As long as the material remains cool during this machining, negligible amounts of stress will be introduced to the new boundary and no additional anneal is needed. The bulge is created by adding a feature to the shape of the plastic dam used to contain the syrup during the bonding (see Section 3.5.2). Due to the heat leakage at the bond's edge, the bulge area does not fully polymerize and must be heated to 40-60°C for an hour prior to disassembling the bonding equipment. It was important that the bulge was not disturbed while it was soft, as this can introduce large amounts of stress.

3.4.4 Bond Tests

To demonstrate the strength of the test bonds, a liquid nitrogen (LN) cryogenic test (cryo-test) was performed. The test was conducted by slowly cooling the bonded disks in N_2 vapour to ~ -50°C. The cold disks were then submerged in LN. This test produced thermal gradients that are more severe than those expected during the cool down and operation of the detector. This test was used in place of a pull test (pulling on sample cross-sections of bond material

until it brakes) as it allows for tests of the entire bond and can be performed with minimal equipment.

During the bonding tests, all bonds that met the uniformity criteria passed the cryo-test. Bonds that failed the cryo-tests resulted in cracks that ran through both the bond and 1/2" acrylic disks. This supported the hypothesis that the failures are caused by localized regions of stress with the majority of the bond having strength close to the parent material. Figure 3.3 shows an example of a bond that failed the cryo-test. The bond criteria that resulted in a bond that survives both cryo-tests are shown in Table 3.1.

Attribute	Description
bond thickness	2.50 ± 0.25
bond uniformity	± 0.5 mm over full diamerter
bulge	extends $\sim$2-mm outside of bond and remains un-disturbed until hardened with the post-cure.
annealing	the bond is thermally annealed to releave stress in the bond.
bulge removal	after annealing, the bulge is carefully removed without significant heating of the acrylic.

Table 3.1: Description of the bond criteria required for a bond to survive the cryo-tests.

3.5 DEAP-3600 LG Bonding Equipment

In order to bond the LG to the AV, special equipment had to be developed capable of producing bonds that meet the required criteria. This section will discuss some of the critical components of the bonding equipment as well as the method to optimize the bonding sequence.

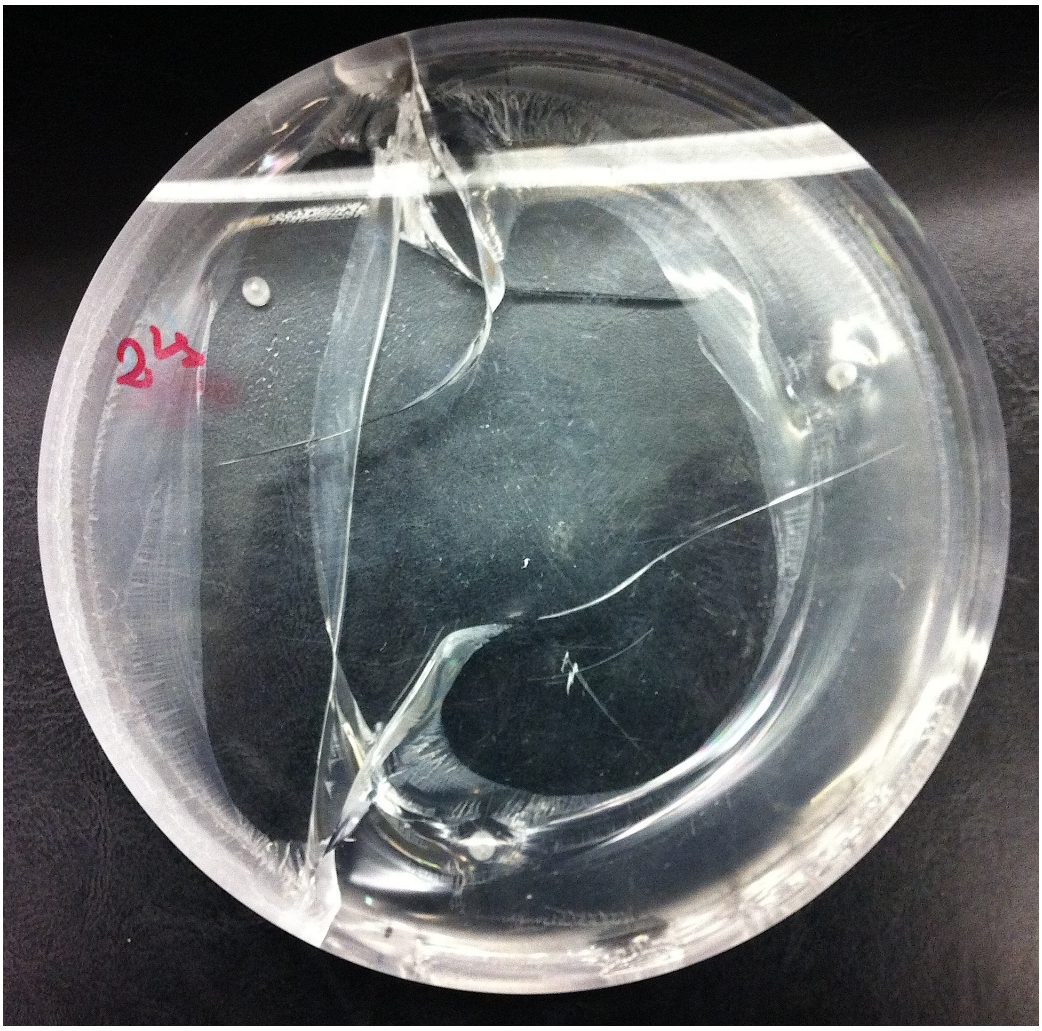

Figure 3.3: Early test bond that failed a cryogenic test resulting in fractures that propagate throughout the acrylic volume of the 1/2" disks.

3.5.1 Tripod

To reduce the risk of differential movement between the LGs and AV during the bonding, an AV supported tripod was used to hold the LG. Shown in Figure 3.4, the tripod legs clamp to neighbouring stubs and LGs. The tripod is aligned to a target stub using an cylinder that is attached to the back of the tripod, slipped over the stub, and held secure to the AV by applying vacuum to

the face of the stub. Once the tripod's joints are all tightened, the alignment cylinder is removed. During tests in Alberta, the shift of the tripod due to the load of the LG was measured to be on the order of 1 mm at the back support. To compensate for this, the alignment cylinders had a 1 mm tilt in the vertical direction. To avoid twisting of the tripod when the alignment cylinder was removed, the tripod joints were relaxed by individually loosening and retightening each joint after their initial tightening.

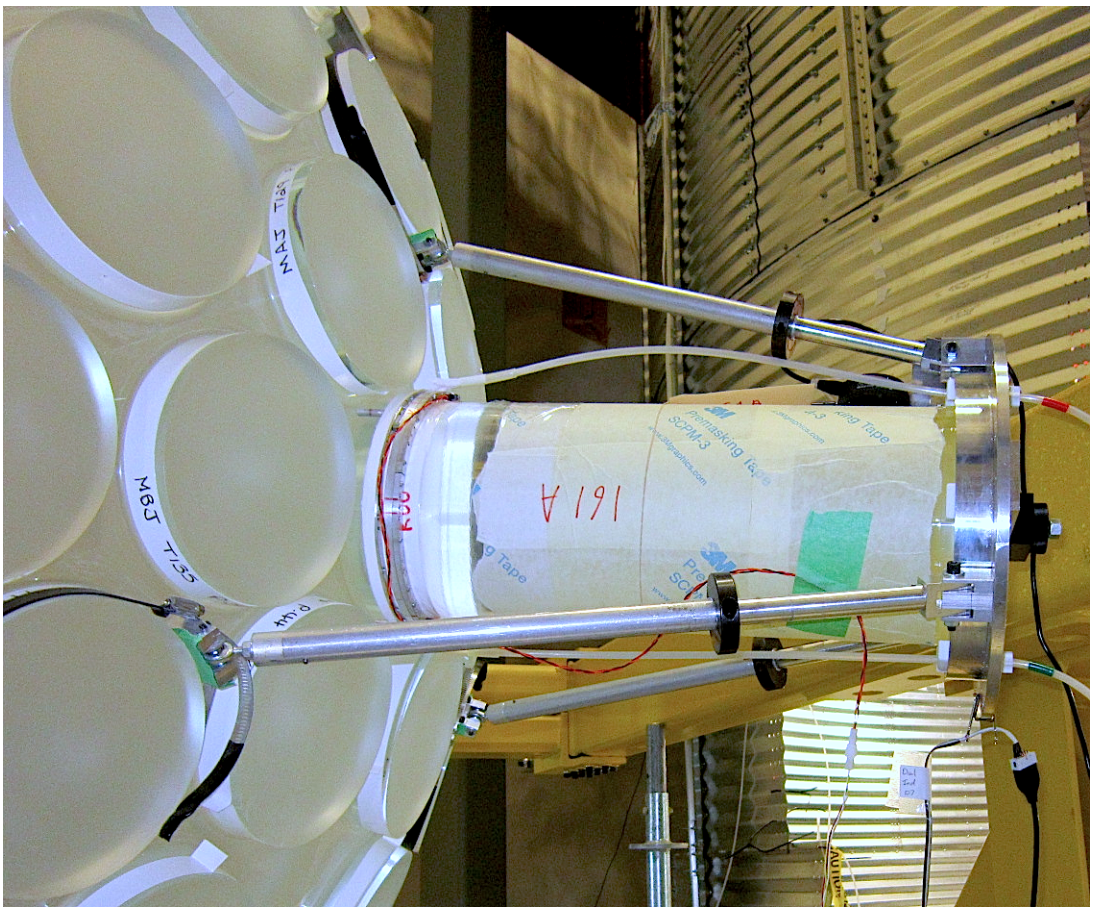

Figure 3.4: Tripod setup on the vessel holding a light guide in place.

3.5.2 Dams and Clamps

The photocathode coverage of the detector is $\sim$ 70%; as such, the spacing between neighbouring stubs is minimal. This makes it very difficult to perform technical work at the base of the stub. A dam was developed that could be installed onto the LG and slid over the stub. An example of a dam is shown in Figure 3.5. The widened base of the dam allows it to be folded over the back dam clamp. AV offset spacers, used to set the dam clamp's position on the stub, screw into the back dam clamp through the folded dam and holds the dam in place. This prevents the dam from getting jammed during installation. The dams have a bulge formed into the side that is aligned to the bonding gap and provides the excess bond material required for an optimal bond (see previous). Figure 3.6 shows an example of an assembled dam on a light guide. This is installed onto the LG with a front dam clamp. The back dam clamp is then held in place with additional alignment clamps during installation.

The dams are fabricated by first stamping two sheets of polyethylene together into a basic dam shape. The seams that resulted from the stamp are flattened with a commercial impulse sealer to avoid leaks. The polyethylene is then installed onto a mould and heat shrunk to the desired shape. Dam moulds made from thermal insulators, such as Delrin, were found to create dams with fewer wrinkles due to a slower cooling of the polyethylene film when making contact with the mould. A smoother dam, provide a better seal against the LG.

The dam clamps make a seal by compressing an o-ring that presses the dam against the acrylic. Each clamp consists of two aluminum rings that are split

Figure 3.5: Fully formed polyethylene dam pre-installation.

into 3 segments. When the front ring segments are tightened to the back ring segments, the internal o-ring is compressed. The screws for the back clamps are accessible through holes in the front clamp. There are 3 alignment pins on the front dam clamp, these alignment pins slide through holes in the back clamp, aligning the front and back clamps. The alignment pins held the front of the LG in place, taking half of the weight of the LG. As long as the dam is free of large wrinkles, the clamps seal the dam and allow no syrup to leak. The inlet and outlet syrup tubes are inserted into the two sleeves on the sides of the dam, and a piece of glue filled heat shrink is used to make a seal.

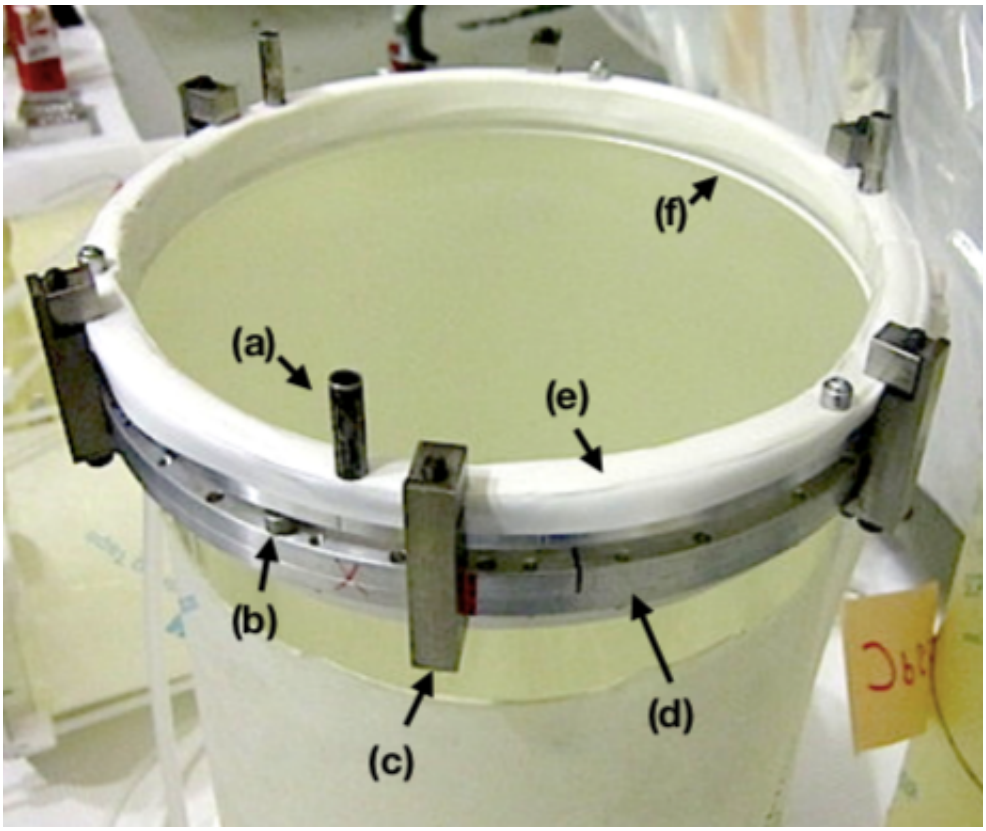

Figure 3.6: Dam installed on a light guide with dam clamps and alignment clamps installed. Identified in the photo is an AV offset spacer (a), the internal spacer (b), spacer clamp (c), light guide dam clamp (d), and dam folded over AV dam clamp (e). The position of the bulge of dam aligned with bond gap (f).

3.5.3 Bond Gap

As discussed previously, it is critical that the bond gap is adequately controlled. Since it is not possible to directly measure the initial bond gap without cutting and destroying the dam, all dimensions in the clamp assembly are strictly controlled so that the initial bond gap is known to within 0.2 mm. All front dam clamps are installed onto the LG using an alignment jig for consistent clamp alignment. The stub length is used to calculate an optimal AV offset spacer to provide an initial gap of $\sim$ 1 mm. It is critical during the bonding

that the AV offsets are checked to ensure that they are the correct length, installed on the correct stub, and touch the base of the stub. The bond gap is then monitored by measuring the movement of the LG from its initial position with a digital dial indicator mounted to the back of the tripod.

3.6 Auto-Fill System

To perform the LG bonding in an efficient manner and reduce the possibility of human error, an automated fill system was developed. The auto-fill system has 10 individually controlled bond channels. Figure 3.7 shows a diagram of the auto-fill system. In order to successfully perform a set of bonds, the auto-fill system performed a number of tasks described in the following sections.

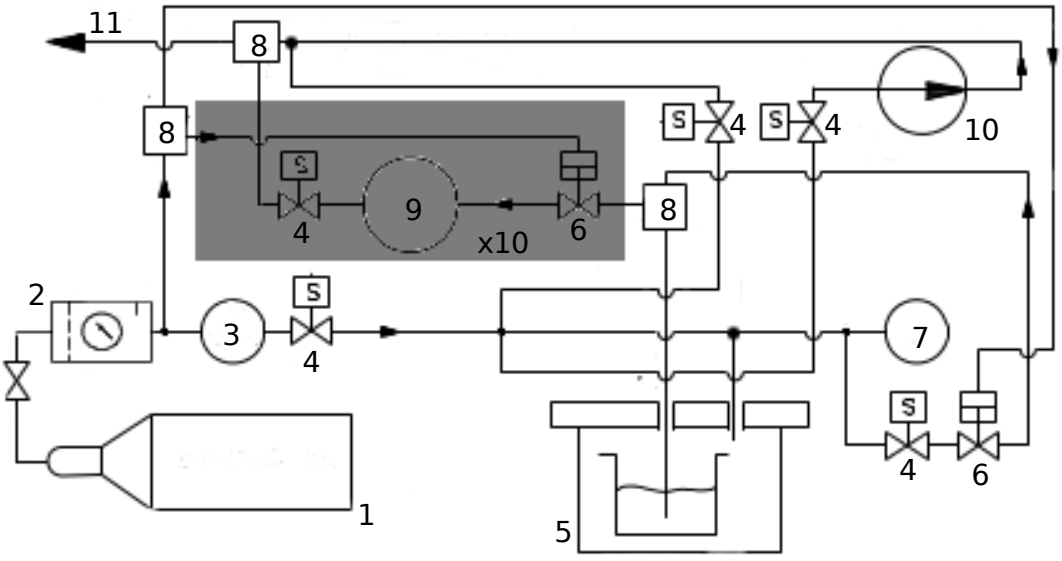

Figure 3.7: Auto-fill system schematic. Components shown in schematic are the nitrogen tank (1), pressure regulator set to 100 psi (2), a gas flow regulator (3), solenoid valves (4), pressure tank, air cylinder actuated pinch valve (6), pressure sensor (7), manifold (8), bond volume (9), vacuum pump (10), and the exhaust output (11).

3.6.1 Bond Gap Referencing

The motion of the LG is monitored using a digital indicator attached to the back of the LG and read by the bonding program. To adequately monitor the bonding gap, the auto-fill system must first reference the dial indicator reading to the expected initial bond gap value. The initial bond gap value is calculated from a calibrated formula that takes into account the stub length and AV offsets installed on the LG assembly incorporating a calibrated offset. The auto-fill system generates light vacuum (-0.5 psig) on the bonding channel that pulls in the LG to its minimal gap. Each LG is manually confirmed to have been fully pulled by checking the dam clamps touch spacers between the clamps guaranteeing a 1-mm initial gap between the LG and stud faces. Based on the variance in the calibrated offset, the 1-mm reference value is accurate to ~ 0.2 mm.

3.6.2 Dam Test

It is critical that the dam is fully sealed and does not leak syrup. The LG should also be capable of moving out to the desired gap and freely slide within the tripod. The auto-fill system is used to perform a dam test on each individual bond channel to check for poor dam setups. The dam test consists of two steps. First it pressurizes the dam with 1.3 psig of nitrogen gas to inflate the dam and check that it expands to the target bond thickness; it then fully releases the pressure and ensures that the LG moves back to its minimal gap. If the stub and LG are misaligned, the friction in the dam clamp's alignment pins impede the movement of the LG. Next, the dam is pressurized to 1.3 psig

and sealed. The deflation time is measured and checked against a minimum threshold time based on previous dam failures. The bonding software requires a bond to pass both parts of the dam test before allowing syrup to flow through the channel.

3.6.3 N_2 Purge

Oxygen inhibits polymerization. All the oxygen is thus removed from the bonding system. To flush the bonding system, an N_2 purge is performed, where N_2 is flowed through the system for 10 minutes at 0.5 psig. The N_2 purge is performed with the syrup already installed inside the pressure tank and this volume is not opened again until the fill is complete. N_2 is pumped into the bonding channels through a bypass valve that allows the gas to enter the inlet manifold without traveling through the primary syrup inlet line. Using a tank pressure of 0.5 psig, the pressure differential between the tank and manifold is too low to push syrup into the manifold while the bypass valve was open.

3.6.4 Degassing

To remove dissolved gasses and any bubbles in the bonding syrup, the auto-fill system degasses the syrup. The degassing sequence used for the LG bonding is to first cycle the pressure in the tank. Starting at -8 psig, the pressure in the tank is cycled between atmospheric and vacuum with the absolute pressure in the tank reduced by half every cycle. The pressure cycling is to prevent the syrup from exiting the container. Once the target vacuum pressure is around 1 psia, it is held for 10 minutes.

3.6.5 Bonding Syrup Injection

Once all the above procedures were completed, the auto-fill system injects syrup into the bond gap. The auto-fill system individually monitors each bond and controls the amount of syrup that is injected into each. The auto-fill system flows syrup through the desired channels with both the inlet and outlet clamps open. Once the syrup has filled up the initial bond gap and starts to exit the outlet port on the dam, the internal pressure in the dam increases, causing the LG to move back in the tripod. Once the gap has expanded to 2.0 mm, the outlet valve closes, increasing the rate of pressure build up within the dam. This reduces the amount of syrup needed. When the bond gap hits the target 2.5 mm gap, the auto-fill system clamps the inlet line, stopping the flow of syrup into the bond.

Due to the restriction for the amount of syrup that could be stored in a given container without overflowing during the degassing, the fills are performed in two groups, with a maximum of 6 bonds per group. Both glue containers are inserted and degassed at the same time in the pressure tank. Between filling the two groups, the pressure tank is re-evacuated to 1 psia for a minute to remove gas that is introduced while switching the syrup containers.

Doing multiple bonds in parallel allows individual bond channels to be cross referenced against each other. By comparing how the slopes of the bond gap changes as a function of time, the user can decide if a channel's expected initial gap is consistent with the fill rate observed from the other bonds. If the channel has the same fill slope, but started expanding later (earlier) than expected, the inlet would be clamped off early (late). If the slope of the bond gap graph

deviated from the others by a significant amount, thus indicating either a decrease or increase in flow, the bond is left to clamp off automatically. Over the course of the LG bonding, $\sim 10\%$ of the fills deviated from the expected fill rate and needed to be manually corrected. In general, the fill gaps of a bond set agreed to within 0.2 mm once the gaps start to expand. The length of the tubing is strictly controlled to allow the slopes of the individual fills to be accurately compared. If significant errors were seen, the injection was stopped and the syrup was extracted from the gap by putting vacuum on the pressure tank.

3.6.6 Bond Sequence Optimization

In order to bond a LG, the stub needs to be within $\pm 10^{\circ}$ of the AV's equator. This strongly restricts which stubs can be bonded at the same time. To minimize the amount of torque needed to rotate the AV, the AV must remain balanced. A method to optimize the order in which the LGs were bonded to the AV was developed allowing the least number of days and a uniform distribution over the AV.The applied sorting method first divides the detector into 5 symmetric groups and identifies the section with the fewest bonds. Within this section, the location that allows the most stubs to be simultaneously bonded is found. The algorithm then iterates through the available stubs, selecting the stub that is the farthest away from all previously selected stubs until either 10 stubs have been selected or all remaining stubs are less than the minimum allowed distance. The stubs are then checked by searching for a replacement stub that better maximizes the distance between all the other

stubs in the sequence. Without including additional constraints due to tripod placement, not all sequences are physically possible. However, the frequency of this is much less than the number of bonds that can not be completed due to the strict underground shift lengths. While it is not demonstrated that this method gives the absolute optimal solution, this method produces a schedule that is within a few days of the 26 day absolute minimum.

3.7 Cleanliness

The materials for the acrylic bonding were selected and monitored for their low ^{238}U and ^{232}Th contamination. To avoid adding any additional contamination to the acrylic bonding, the bonding syrup is mixed, stored and poured from the same ultrasonically cleaned glass jars. The syrup's exposure to air is minimized as was the amount of transferring between other containers when syrup batches are split.

While bonding, effort is made to ensure the cleanliness of the bonds. All work is done in SNOLAB's class 2000 clean room environment. Latex gloves are worn to reduce the possibility of contaminating the detector and bonding surfaces. In addition, all the equipment was ultrasonically cleaned and periodically wiped down to prevent dust accumulation. Prior to bonding, the surfaces of the stubs were wet sanded with 240 grit sanding pads to remove any accumulation of contaminates on the surface layer. The surface is then wiped with lint free cloths and vacuumed to remove remaining acrylic dust. For the LGs, this exercise was performed before the dams are installed.

3.8 On-Site DEAP Light Guide Bonding

Figure 3.8: The DEAP-3600 AV supported in the rotator stand after light guide bonding.

The LG bonding was carried out on site between July and November 2013.

Within this period a total of 44 days were spent on bonding, averaging 6 bonds per active day. A total of 6 LGs had to be removed and re-bonded due to failed bonds. The two reasons for failed bonds were un-parallel bonds (4/6) and thick bonds (2/6). There were several ways in which the bonds became un-parallel, the first being shifting in the tripod. It was found during the commissioning of the underground bonding that if the travel of the LG was restricted by the tripod, the force exerted on the tripod is large enough to cause significant shifts in the orientation (this was not observed during test due to the flexibility of the test support). The second circumstance occurs if there was a substantial leak of syrup from the dam during the polymerization stage. The last reason for un-parallel bonds is simply human error while checking the tripod alignment. It is suspected that the two bonds that failed due to the gap thickness are due to an improper initial measurement of the stub length and a failure of the operator to properly judge the correct point to manually stop the injection, as discussed in section 3.6.5. The failed bonds were machined off the AV and were re-bonded with new LGs. The remaining stub after removing the LG were shortened by 1mm to ensure the stub surface was not compromised by the previous bond attempt. The fully bonded AV is shown in Figure 3.8.

Chapter 4

Analysis Flow

When an event happens in the DEAP-3600 detector, there are many different stages in data processing that must occur before physics information can be extracted from the raw data. There are also many details that need to be considered in order to properly interpret the results and understand the event. This chapter discusses the steps in the data collection and analysis.

4.1 Trigger

The PMT signals are amplified and shaped by custom signal conditioning boards (SCBs). Each individual PMT channel is then measured by a CAEN V1720 digitizer while a summed signal of all the SCB channels is sent to a trigger module FPGA (DTM). The DTM integrates the current of the summed PMT signal computing a first estimate of the prompt energy (Trigger Eprompt) and fPrompt (Trigger fPrompt). It uses this information to trigger events. Physics data is split into 5 different triggers, roughly separating 3

different energy regions, and 2 PSD regions. Figure 4.1 shows the separation of the 5 trigger regions. The trigger region B contains the WIMP ROI. The trigger region C is pre-scaled to reduce the amount of saved data, this is further discussed in Chapter 6. There are also two periodic triggers: one injects current pulses into the SCB board for time calibration of the digitizers time offsets and a second trigger to take random snapshots of the PMT signals. In general the periodic triggers are set to a frequency of 20 Hz.

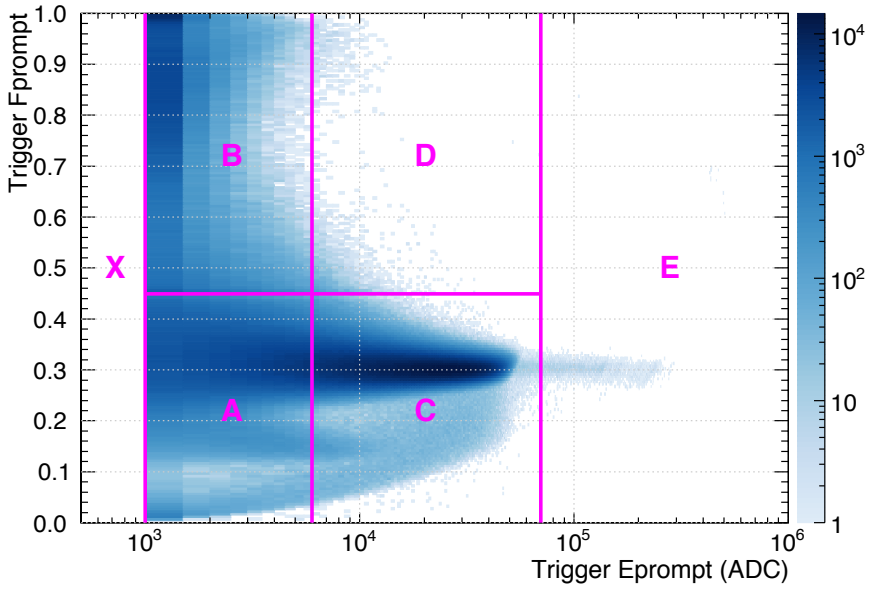

Figure 4.1: Division of the different physics triggers from the DTM's measurement of fPrompt and prompt energy. The Region X is below the trigger threshold. The low and high fPrompt, low energy triggers are shown in regions B and C respectively. The low and high fPrompt, medium energy triggers are shown in regions C and D. The high energy trigger is shown in region E. Figure taken from Ref. [84].

4.2 Front End Analysis

When the DTM measures enough current in the summed PMT signal to satisfy one of the triggers, a signal is sent to the digitizers to save the PMT waveforms. A front-end computer then retrieves the digitized PMT waveforms from the digitizers, and summary information from the DTM about the trigger, and stores the information into a MIDAS [105] format on disk. Due to high event rates dominated by ^{39}Ar decays, a data reduction method is applied to the data prior to saving the data to disk. This data reduction method is called SmartQT and will be discussed further in Chapter 6. Once the data are saved to disk and moved to the online storage, the data are converted from the MIDAS format into a ROOT format.

4.3 Low-Level Analysis

The next step in the data analysis is to process the PMT pulse information into physical time and charge. This is done with the SmartCal (Smart Calibration) processor, and will be fully explained in Chapter 5. The trigger information is also checked to make sure that the event is from a physics trigger and can be used for analysis. A 64-bit variable named CalCut is saved with every bit of the variable representing a boolean for a given low-level state. This variable allows for easy removal of events that are not caused by physics triggers or events that were improperly read out. The last step in the low-level analysis is to evaluate each event and determine how many individual particle interactions are contained in the event window. Events with more than one particle

interaction are called pile-up. Identification of pile-up is first performed by the Multi-Event processor (see detail in Chapter 8).

4.4 Mid-Level Information

The remainder of the analysis performed on the event assumes it comes from a single particle interaction (with the exception of the Multi-Site Processor discussed in Chapter 8). The next step is to find the start time of the event. This is done with the TimeFit processor.

4.4.1 TimeFit

The TimeFit algorithm first locates the beginning of the event by histogramming the pulse's charges into 100 ns time bins. Starting at the bin with the most charge, the algorithm scans backwards in time to find the first 100 ns bin with more than 3 pulses. The earliest pulse time that entered this bin is then used as the reference time for defining the prompt pulses that are used to fit the time and position of the event. The algorithm takes all the PMT pulse times from -50 ns to +200 ns and performs a fit to find a time and position that minimizes the time residuals between the measured pulse time and the time-of-flight (TOF) for a photon traveling on a direct path between the event position and centre of the PMT photocathode. The fit is done in 3 iterations. At the end of each iteration pulses with time residuals greater than 8 ns are removed from the fit. This is to reduce the contamination of non-singlet light from the TOF fit. The TimeFit algorithm splits events into 3 classes based on the fraction of charge measured in the highest charge PMT (fMaxPE). Events

that have an fMaxPE<0.2 are consistent with events that occurs within the LAr and are fit with the LAr TOF equation given by:

$$TOF = \frac{r_{LAr}}{v_{g,LAr}(128\text{nm})} + \frac{r_{GAr}}{c} + \frac{r_{Acrylic}}{v_{g,PMMA}(445\text{nm})} \tag{4.1}$$

where r_{LAr}, r_{GAr} and $r_{Acrylic}$ are the path lengths in the different mediums the photon passes through. The term $v_{g,i}(\lambda)$ is the group velocity for material i at wavelength λ. Events that have fMaxPE>0.25 are dominated by particle interactions that create light in a LG, and a LG TOF fitter is used. For the LG TOF fitter, only the time and radius of the event are varied, and the θ and ϕ orientations of the event are fixed to the axis of the PMT with the highest charge. If the radius of the event is within the AV or LG acrylic, the TOF equation is given by:

$$TOF = \frac{r_{LAr}}{v_{g,LAr}(445)} + \frac{r_{GAr}}{c} + \frac{r_{Acrylic}}{v_{g,PMMA}(445)}. \tag{4.2}$$

All light that originates in the acrylic is propagated from the interaction site in the LG to the boundary of the AV and LAr before taking the next direct path to the target PMT LG base. For events with $0.2 <$ fMaxPE < 0.25, the first pass reconstruction is performed with either fitter, and the TOF calculation with the lowest time residual is chosen for the remainder of the two passes. Figure 4.2 shows the flight paths for ideal LAr and LG events. As will be discussed later, due to the removal of events with high fMaxPE, only events fit purely with the LAr fitter are used in the WIMP analysis.

The minimum TOF times are saved for every PMT and are subtracted from the PMT's pulse times.

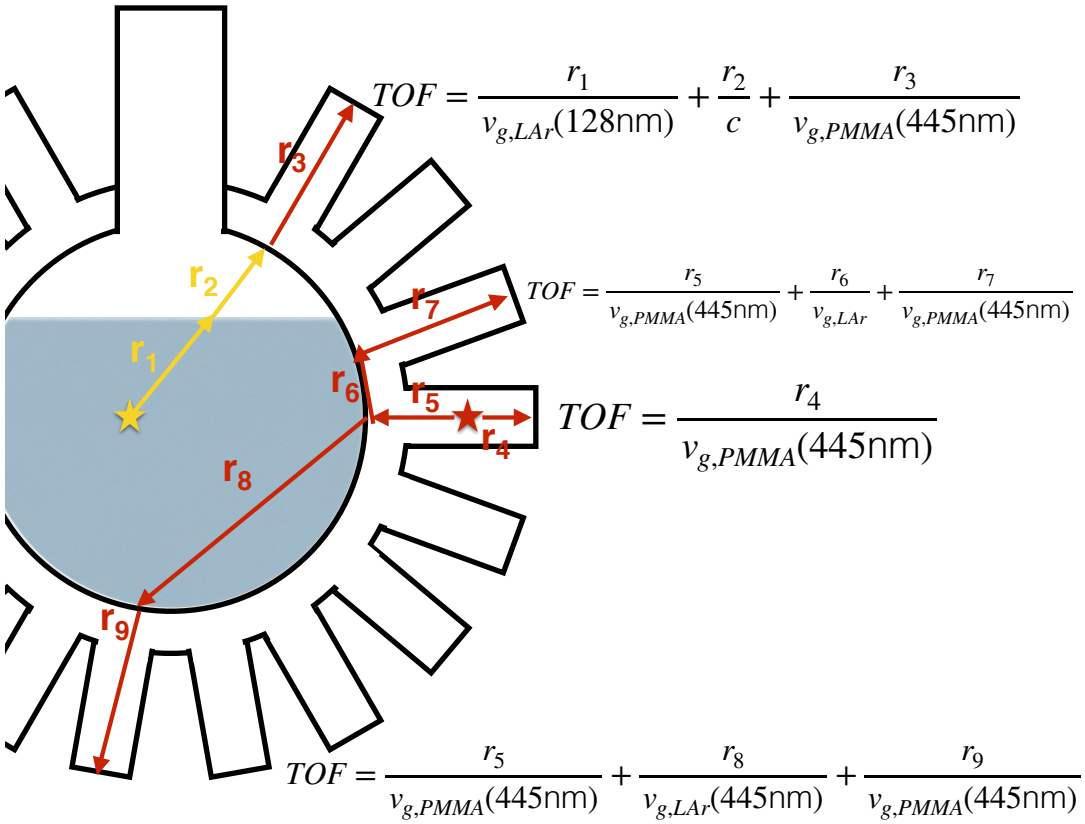

Figure 4.2: Diagram shows sample photon flight paths for different event positions and shows the corresponding TOF equation. Yellow arrows symbolize UV photons and Red arrows symbolize optical photons.

4.4.2 Afterpulse Identification

Not all of the pulses in the PMT's signal are due to photon interactions. There are a number of other ways in which pulses can be created, including darknoise (DN) and afterpulsing (AP). DN is a random emission of electrons from the cathode that create pulses in the PMT. The rate of DN pulses is highly dependant on the PMT's temperature. At -20°C, the average rate of DN in the DEAP PMTs is ∼500 Hz, meaning on average a 16 us window will have around 2 DN pulses between all 255 PMTs.

Afterpulsing is caused by residual gas in the PMT that is ionized during

the electron cascade. A positive ion will then slowly drift in the electric field and, in some cases, reach the photocathode. When the ion collides with the cathode it can release electrons, creating a secondary pulse. Due to the mass of the residual gas particle, the secondary pulses are delayed from the initial PE pulse by many micro seconds. Figure 4.3 shows an example of the time difference between the initial pulse and the AP, as well as the charge of the AP. As can be seen in the figure, the majority of the APs have charges equivalent to a SPE, although, there also exist many pulses that have many PE with a maximum near 35 PE. These high charge pulses have the possibility to greatly skew the variables computed for the physics event such as the energy and distribution of light. High charge APs are removed from the data in order to minimize the effect of AP on the result.

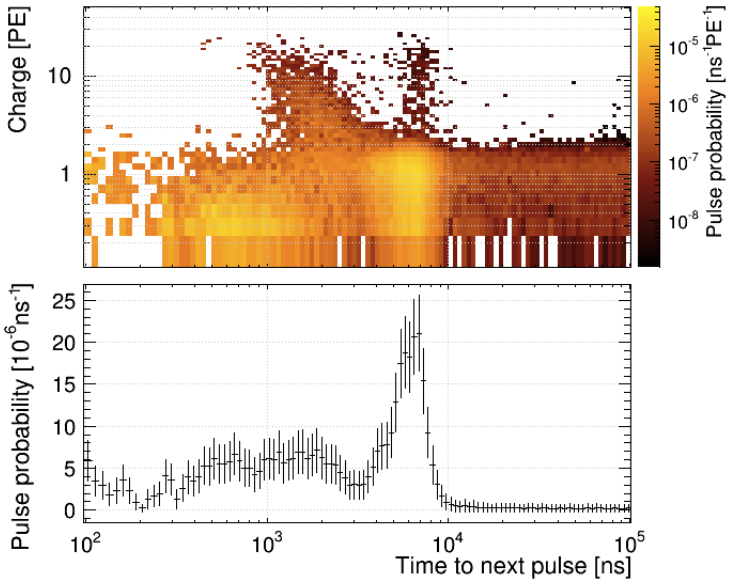

Figure 4.3: The Afterpulsing time and charge distribution (top). The time distribution for all afterpulse charges is shown (bottom). Figure taken from an early version of Ref. [106].

APs are identified in this analysis based on their pulse characteristics and timing. Since almost all of the observed APs occurs beyond 200 ns, no pulse can be identified as an AP if it happens within 200 ns of the start time of an event. In the late times of the event, the rate of pulses will exponentially decreases, as expected from the exponential decay of the triplet dimer state. This makes it increasingly unlikely for multiple photons to pile-up and create high charge pulses. When pulses do randomly pile-up to create a high charge pulse, they will typically have slightly wider widths than a SPE pulse scaled to the same charge. In contrast, since the electrons from an AP are released within an unresolved time window, the spread in time of the electrons released by the ion do not strongly affect the width of the pulse shape. Taking these considerations into account, AP pulses are selected and removed from an event if they satisfy the following conditions:

- High Charge (Q>3.5 PE)
- Isolated in time and charge (charge in other peaks within $\pm$ 10 ns is less than 6 times the pulse's charge)
- Narrow (width across the 20% height is between 24 and 31 ns and Q>25 pC)

This criteria has been seen to remove the majority of the large APs that are the most problematic for skewing the data variables. Figure 4.4 shows the average waveform for ^{39}Ar events, with separate curves showing the shape of the removed AP and the average pulse shape used in the analysis.

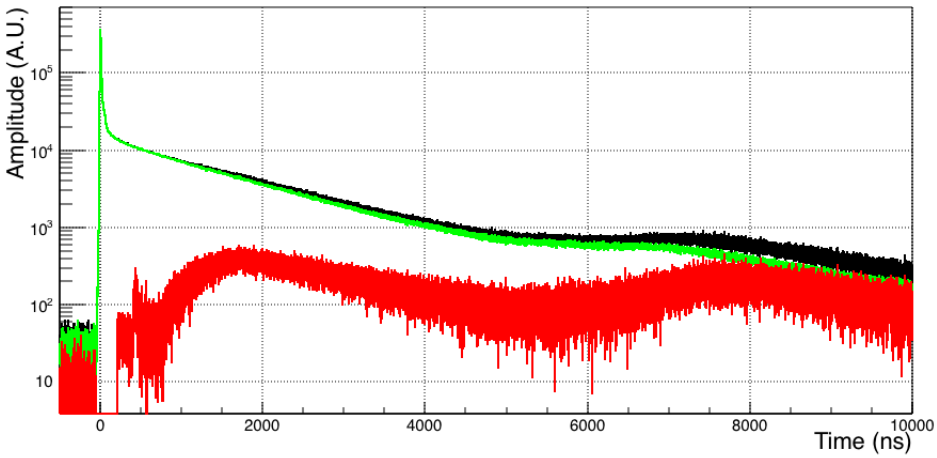

Figure 4.4: Accumulated waveforms for ^{39}Ar events. The waveform is shown with all pulses (black), only pulses not tagged as afterpulses (green), and only pulses tagged as AP (red).

4.4.3 Charge Integration

With the APs identified, the event can then be integrated over different windows that will then be used to do further analysis. The start time for all the integrals is 28 ns before the event time found by TimeFit. The stop times of the integration windows used in this analysis are 60 ns, 150 ns, 400 ns and 10 us. Each individual PMT signal is integrated in these windows. The individual PMT signals are all scaled by dividing the measured charge in pC by the mean charge of a single PE charge in PE (QPE_{pmt}). The scaled PMT integrals are then summed together to obtain the overall window integrals. These integrals are then used to compute the variables in Table 4.1, which are used for event identification and higher order position reconstruction.

Parameter	Definition	Description
$QPE(t_{\min}, t_{\max})$	$\sum_{255} QPE_i(t_{\min}, t_{\max})$	PMT charge integrated from from $t_{\min}$ to $t_{\max}$
QPE	$QPE(-28\text{ns}, 10\mu\text{s})$	Total event QPE
Prompt_{60}	QPE(-28 ns, 60 ns)	Total QPE up to 60 ns
Prompt_{150}	QPE(-28 ns, 150 ns)	Total QPE up to 150 ns
fPrompt_{60}	Prompt_{60}/QPE	PSD variable using Prompt_{60}
fPrompt_{150}	Prompt_{150}/QPE	PSD variable using Prompt_{150}
QPE_{400}	QPE(-28 ns, 400 ns)	Widest integration window free of AP contamination
$\text{fMaxPE}_{\text{prompt}}$	$\text{Prompt}_{60,iQ\max}$/QPE	Fraction of prompt charge in highest charge PMT
fMaxPE	$\text{QPE}_{iQ\max}$/QPE	Fraction of charge in highest charge PMT

Table 4.1: Definitions and descriptions of the different charge derived variables used in the analysis.

4.5 High-Level Analysis

With the detailed PMT-level information computed, a higher level analysis can be performed with this information including, pile-up selection, position reconstruction, and discrimination of events that occur in the neck of the detector (referred to as neck events). The following sections will give a brief overview of the higher level analysis steps that seed the WIMP analysis presented in Chapter 9.

4.5.1 Higher order Pile-up removal

An algorithm has been developed in order to discriminate pile-up that is unresolved by Multi-Event described in Chapter 8. This algorithm is called Multi-Site. The target pile-up events are those due to a LG Cherenkov events overlapping with an ^{39}Ar scintillation event. If the Cherenkov event overlaps

with the prompt time window of the event, then the pile-up event can mimic a WIMP recoil in fPrompt and QPE. Multi-Site will be discussed in Chapter 8.

4.5.2 Position Fitting

For this analysis, a position fitter (referred to as MBFitter) is used. This position fitter is run using the 400 ns integrated PMT charges to keep the largest amount of charge while not including any of the AP regions and avoiding the use of high-level AP removal techniques. The fitter compares the measured PMT charges with probability distribution functions (PDFs) created from RAT simulations to fit the event position. The fitter has been tuned using the latest version of the optical model, as discussed in Chapter 7. Figure 4.5 shows the distribution of events in a projected Z, ρ space, where ρ is the radius of the event in cylindrical space. The bins are weighted by $1/\rho$ so that uniformly distributed events show as a uniform colour in the colour scale. The slope towards the centre position for events on the LAr surface is expected to be due to the limitations of the fitter in handling the detector being only partially filled with LAr. The MBFitter uses spherical symmetry to rotate the training PDFs to other orientations. As such, a break in the spherical symmetry causes a bias in the position. Figure 4.6 shows the distribution of r^3, where r is the physical radius; in comparison, the expected r^3 distribution is shown in red. A discussion of the optical model used to create the PDFs used in the MBFitter algorithm will be given in Chapter 7.

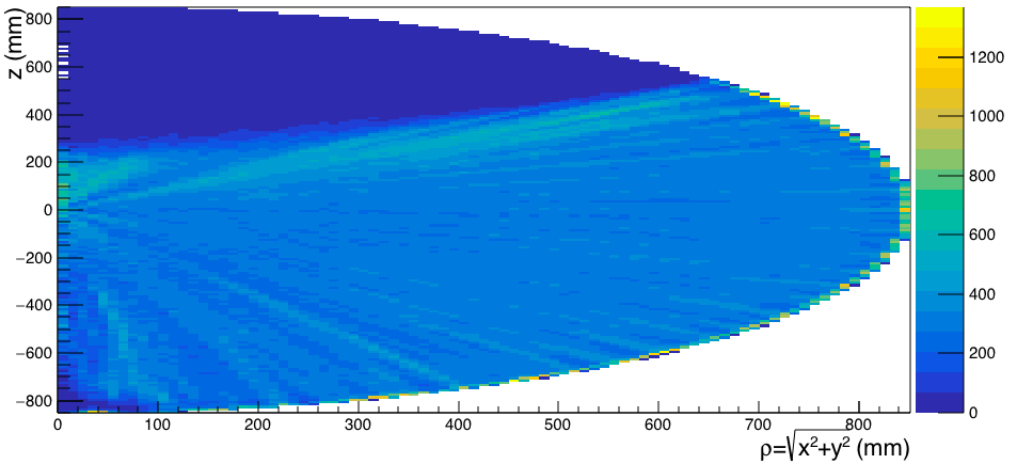

Figure 4.5: Fit position in cylindrical coordinates of ^{39}Ar events found using the MBFitter. The amplitude has been normalized by ρ^{-1} so that an isotropic distribution would give a flat amplitude (uniform colour).

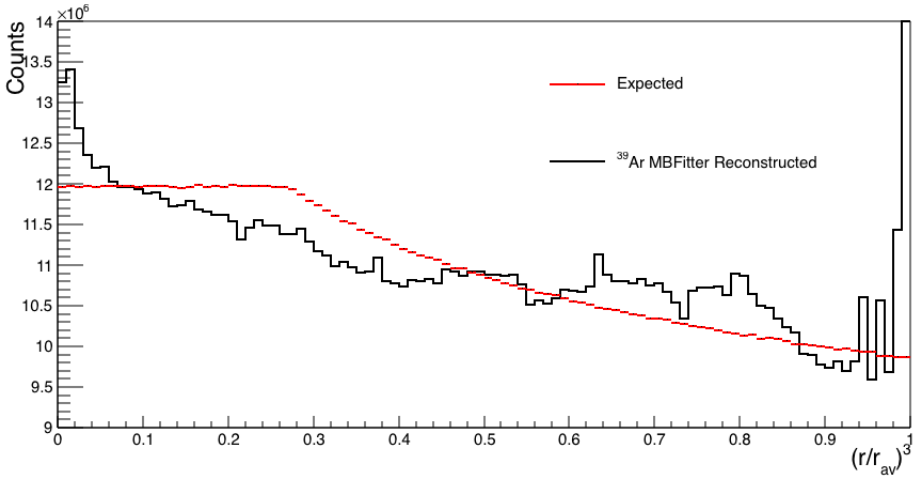

Figure 4.6: Distribution of the normalized cubed radius $(r_{mb}/r_{av})^3$ where r_{mb} is the radius of reconstructed vertex position from the MBFitter algorithm and r_{av} is the radius of the acrylic vessel (black). The expected distribution computed based on the liquid argon fill level is shown (red).

4.5.3 Neck Event Discrimination

Due to the lack of photocathode coverage in the upper detector, events that occur in the neck region have the potential to be shadowed by the Ar flow guides and appear in the data as lower energy events. This is an issue for α-decay events in the neck, as they will have a high fPrompt value and can leak into the low energy WIMP region of interest. There are several ways that we try to discriminate these events, including:

- measuring a large fraction of light in the PMTs above the LAr level
- light in the neck veto PMTs
- discrimination by the LRatio algorithm.

For more information on neck events and the LRatio algorithm, we refer the reader to [107].

4.5.4 Pure Cherenkov Removal

Gamma rays that Compton scatter within the LG and AV acrylic can release high energy electrons that emit Cherenkov light as they travel in the acrylic. This light is emitted within the prompt time window. However, due to after-pulsing, these events can appear within the WIMP ROI. These events can be statistically separated from a LAr event by looking at the fraction of PMTs in the event that measure both prompt light and late light. If the majority of the PMTs that see late light also have a prompt pulse then this event is likely a Cherenkov event with a high number of APs. In contrast, LAr scintillation events should not have a strong correlation between the PMTs that see prompt

and late light since they come from two uncorrelated decays of Ar dimer states. The measurement of this correlation is referred to as LateAPFrac. This identification criteria has been found to work well for events below 100 QPE. Above this energy, the correlation due to random pulse pile-up in single PMTs becomes too high to separate statistically.

4.6 Cuts

The event identifications previously discussed are all introduced as a series of cuts applied to the data. The cut flow is given in Table 4.2 and 4.3. The majority of these cuts are considered standard cuts from the first data analysis of DEAP [108]. The main difference between this analysis and the first analysis is the inclusion of Multi-Site, Position Fitting, and a switch to a PSD variable that uses a 60-ns prompt time window instead of a 150-ns prompt window. The TopRingFrac cut (described in Table 4.2) has also been modified to better discriminate events in the neck region. The WIMP acceptance and livetime of each of these cuts will be discussed in Section 9.4.

Cut	Description	Cut Value
Data Quality	Removes sub-runs where the detector was not in a stable state.	
CalCut	Removes non-physics events and events that could not be properly recorded.	
DeltaT	Imposes a software deadtime of 20 μs between events. This enforced deadtime removes events that likely have large	remove $\Delta T < 20\mu s$

	amounts of AP contamination from previous events.	
Multi-Event	Removes pile-up events in the data found by Multi-Event.	See Chapter 8
Early Pulses	Removes events with too many pulses in the first 2 μs of the raw event to cut pile-up of low-energy events that could put high charge AP in the prompt region of the triggered event.	remove $N_{early} > 3$
t_0	Removes events selected by timefit where the event time window would be truncated by the digitizers and the full event window would not be recorded.	Remove $t_0 < 100$ ns and $t_0 > 5900$ ns
TopRingFrac	Removes events that have a large fraction of light in the top two rings of PMTs. This helps remove events that happen in the gaseous Ar at the top of the AV and in the neck region of the detector.	Remove events with TopRingFrac> 0.03
Multi-Site	Removes events that are identified as potential pile-up, primarily from Cherenkov and LAr scintillation.	See Chapter 8
FMaxPE	Removes events that have too much of their total event charge in a single PMT. This removes events that happen at the	Remove $fMaxPE_{prompt} > 0.2$

	edge of the detector and within the LG.	

Table 4.2: Name and description of low-level used in this analysis.

Cut	Description	Cut Value
Position	Removes events that are outside the fiducial mass, as described by the MBFitter reconstructed event position.	Remove $r_{\mathrm{MB}} > 800$mm and $z_{\mathrm{MB}} > 450$mm
Muon Coinc	Removes Events that are close in time with a muon veto trigger. This is to remove neutron events that are caused by a muon interaction in the detector materials. There is also a cut of 3 minutes on seismic activity, as measured by the muon veto trigger rate.	Remove events within 4s
Gamma Coinc	This removes nuclear recoil events that have a gamma following close in time. The gamma may indicate a neutron capture.	Remove events within 1s
LRatio	This removes events that, based on a simulation built PDF, look more like a neck event than a WIMP event.	Keep events with $\mathrm{LRatio}_{\mathrm{GapB}} < 0$ and $\mathrm{LRatio}_{\mathrm{GapC}} < 0$
Neck Charge	Removes events with too much charge in the neck veto PMTs. This is to remove event that happen in the neck region of the detector.	Remove events with > 10 pC.

LateAPFrac	Removes events that have too much correlation between the PMT that measures prompt and late light. This removes Cherenkov events that slip into the WIMP ROI due to a large amount of AP.	Remove events with NHit < 100 QPE < 100 LateAPfrac > 0.75
PSD	Removes ^{39}Ar on the lower edge of the cut and removes Cherenkov events on the upper edge of the cut.	See Chapter 9

Table 4.3: Name and description of heigh level cuts used in this analysis.

Chapter 5

Pulse Finding

The information coming from the PMTs is the measured voltage across a capacitor on the base of the PMT. This analog signal is digitized into a trace of the pulse shape. The pulse finding algorithm is referred to as SmartCal. Figure 5.1 shows a collection of traces within an event for a single PMT.

The first step in the offline analysis is to take this digitized raw signal and convert it into more physical information by locating the time and size of each of the pulses. Extracting the precise times of each of the photons allows for a much more in-depth analysis of the event compared to simpler charge integration methods used in some other analysis [100]. This information extraction is called pulse finding. The following chapter will discuss the pulse finding method developed for the DEAP-3600 analysis.

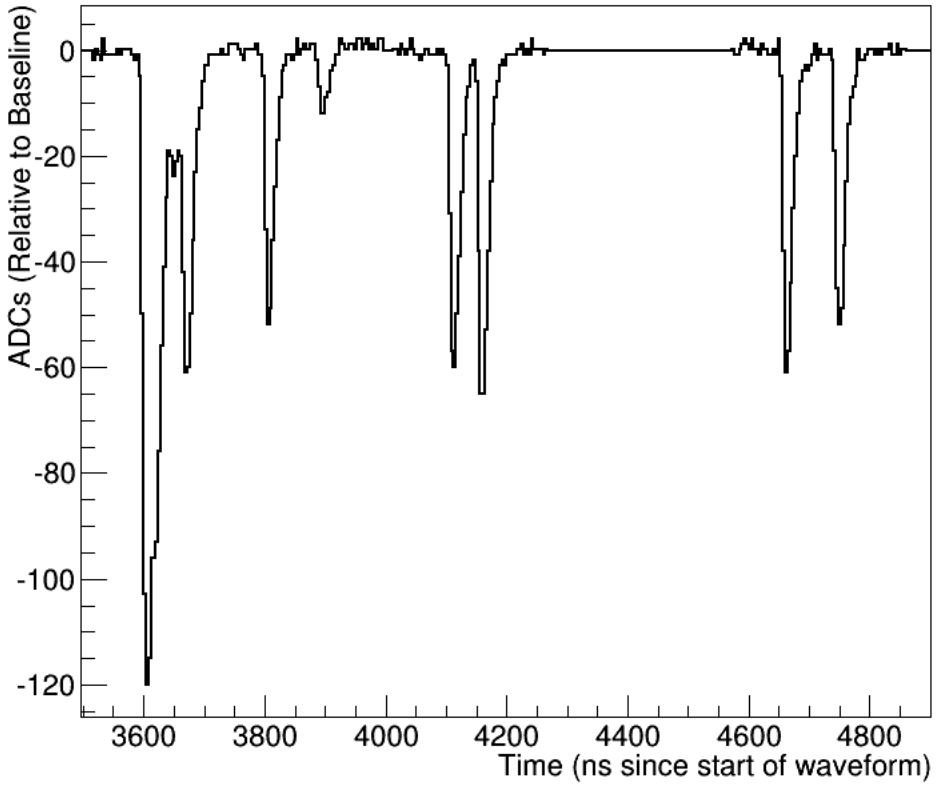

Figure 5.1: Example waveform for a single PMT in an event. Data is in ZLE mode, so only blocks of data that cross the digitizer's threshold of ~ 0.1 of the mean PE amplitudes are shown.

5.1 Pulse Finding Algorithm

Pulse finding is performed by looking at the derivative of the waveform. This reduces the dependence on a fixed and known voltage baseline before pulse finding, and is capable of handling fluctuations in the baseline over events, and entire runs, without modifying the pulse finding parameters. The first

step is to calculate the waveform's derivative defined with

$$\frac{dV}{dt}(i) = \frac{V(i+1) - V(i-1)}{2}. \tag{5.1}$$

Here $V(i)$ is the voltage in a 4-ns time bin, i is the bin number within the ZLE waveform. Figure 5.2 shows a typical SPE pulse and its derivative. The derivative is then scanned to find where the absolute value of the derivative exceeds 3 ADC triggering the start of a pulse, defined as three bins before the derivative threshold crossing. The voltage samples before the pulse are used to calculate a local baseline. If there are too few voltage samples to calculate an accurate local baseline, then the previously measured baseline for the channel is used. While the algorithm is evaluating a pulse, the integral of the current is calculated. The derivative of the pulse is monitored for zero crossings, signifying the location of minima (peaks) and maxima (valleys). A local minimum is considered a sub-peak if the peak is at least 5 ADC units below the previous valley. A pulse ends when the derivative returns close to zero (< 0.25 ADC/ns) and the voltage of the current is close to the local baseline (< 2 ADC from baseline).

The algorithm has been optimized for single PE (SPE) pulses with significant time separation since this the primary signal for WIMP events. However, there are background events with much higher energy that will create many PE pile-up pulses. To better handle such circumstances, the pulse finder will primarily separate pulses once the estimated charge from the local baseline exceeds 10000 ADC units. The pulse splitting is permitted at a local valley that has decreased within 3 ADC units of the local baseline.

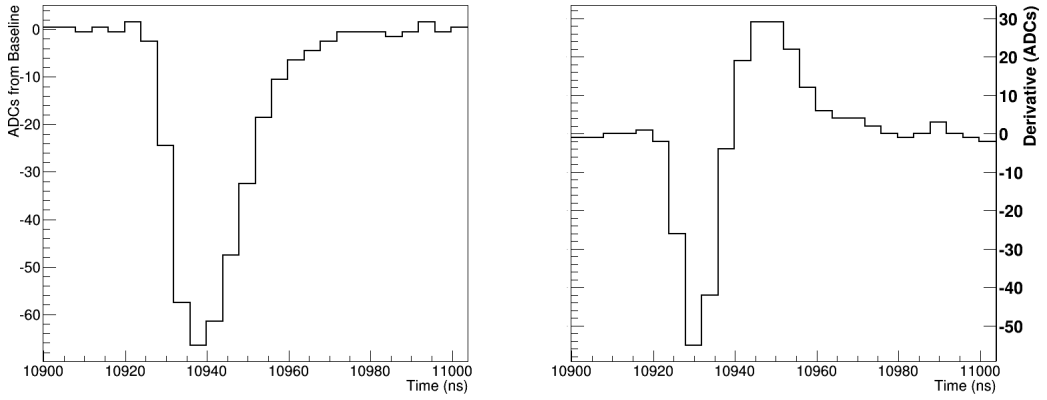

Figure 5.2: The voltage trace of a typical SPE pulse (left) and the derivative of the pulse is shown (right).

At the end of the pulse finding process, the event baseline is updated using voltage samples not contained within any of pulses and that a derivative less than 0.25 ADCs/ns.

5.2 Pulse Shape

An analytic approximation of the pulse shape was made by fitting single pulse shapes to a stretched log-normal function:

$$V(t) = -Q\frac{1}{\tau\sigma * \sqrt{2\pi}} \exp\left(log(\tau) - \mu\right)^2/2\sigma^2 + \beta, \tag{5.2}$$

$$\tau = (t - t_o)\eta. \tag{5.3}$$

Here σ and μ are the fit shape parameters, and t_o, Q and β are pulse time, charge and baseline, respectively. The η parameter was added to stretch the function to the time scale of the pulse. One full sub-run of the laserball

data was used to fit the shape parameters for individual pulses. From the distribution of fit parameters, the shape parameter was taken as the mean of each distribution. These fits were performed twice: the first pass of fits were performed over all the pulses to obtain the average pulse shape parameters by floating all pulse parameters, a second pass was performed fixing the shape parameters η, σ and μ to the mean values in the first round and only t_o, Q and β are varied. This second round of fits was to verify that variation in the pulse shape parameters did not significantly change the fit pulse time. The fit parameters are given in Table 5.1 with the RMS of the distribution and the average fit errors for the parameters. As can be seen in the table, the variation in the fit values of the shape parameters is dominated by the expected variation from the fit errors. This analytic pulse shape was found to perform better in the pulse analysis compared to the pulse shape derived from oscilloscope data discussed in Section 6.2.

Parameter	Mean Fit Value	RMS of Fit Results	Mean Error of Fits
μ	4.52	0.11	0.06
σ	0.42	0.04	0.03
η	4.64	0.31	0.26

Table 5.1: The pulse shape parameters fit to individual pulses to the log-normal function in Equation 5.2. The mean fit value is shown along with the RMS of the parameter distribution and the mean fit error.

5.3 Pulse Analysis

5.3.1 Sub-ns Timing and Sub-Peak Charge

Pulses are fit to the shape to calculate the precise time and charge of each sub-peak. For each sub-peak, four voltage samples around the peak are used to fit the peak to the template pulse function. The fit is performed in two consecutive χ^2 fits. The first is a coarse search with step sizes of 1 ns, followed by a fine grid search of 0.2 ns. The combination of grid sizes optimizes the efficiency at covering the full 12 ns search area with the fewest computations by minimizing N_{pass} in

$$N_{\text{pass}} = \frac{N_{\text{range}}}{\delta_{\text{coarse}}} + \frac{2\delta_{\text{coarse}}}{\delta_{\text{fine}}} - 2. \tag{5.4}$$

With a coarse grid size $\delta_{\text{coarse}} = 1$ ns, N_{pass} is minimized at only 19 passes instead of 60 (if performed with the fine grid search). For every pass, a sub-peak charge is computed assuming the peak position, and calculating the weighted average scale parameter. The χ^2 value is then calculated assuming constant error for the voltage samples. All previous sub-peaks in a pulse are accounted for during the fits by adding the previous fit pulses to the fit function. Figure 5.3 shows a single peak pulse fit and a multi-peak pulse fit. The shaded regions indicate the pulse voltage samples that were used in the fit. For pulses that fit to the central region of the peak bin (defined as bin phase = 0) the χ^2 distribution is shown in Figure 5.4. Fitting the χ^2 distribution and finding the time of $\chi^2_{min} + 1$ gives a rough estimate of the pulse time resolution, also shown in Figure 5.4. The χ^2 distribution gives a pulse finding time resolution

of ∼0.1 ns.

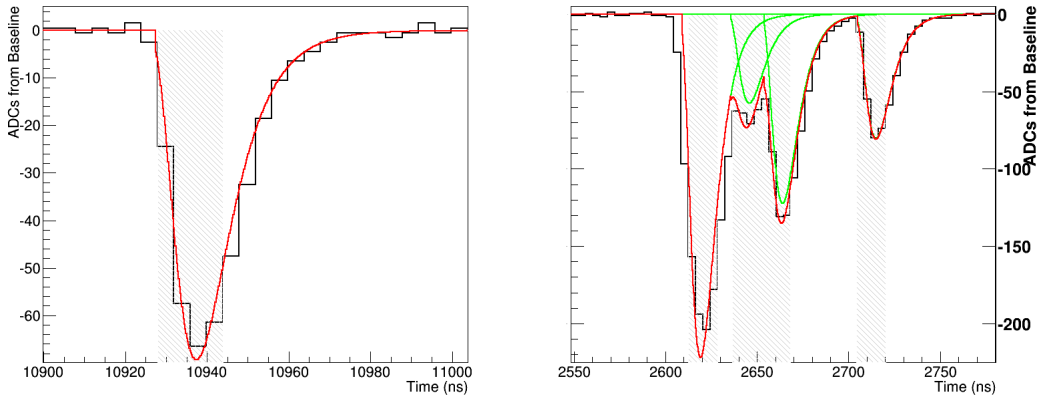

Figure 5.3: Examples of pulse fits for a single SPE pulse (left) and a multi-peaked pulse (right). For the multi-peak pulse the individual (dotted) and summed reconstructed pulse shapes (solid) are shown. The shaded regions indicate the voltage samples used in the fits.

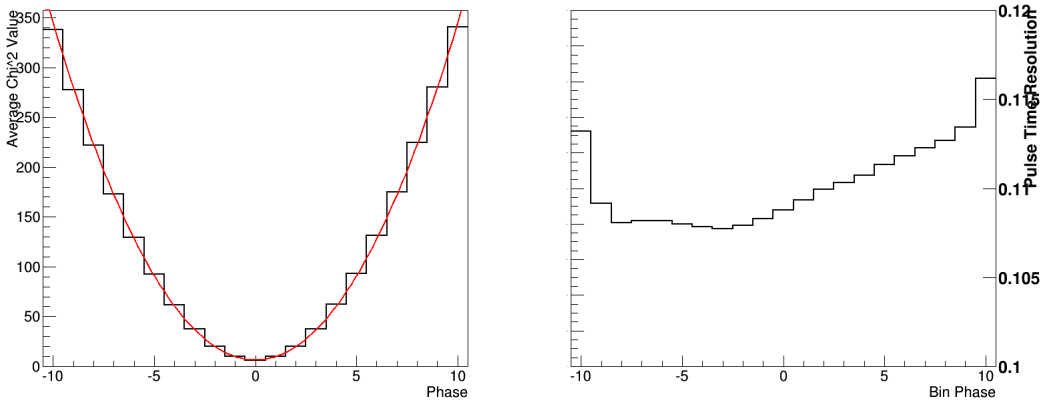

Figure 5.4: χ^2 Distribution for phase 0 pulses. The individual bin phases are fit to a polynomial and the resolution is computed by finding the phase of $\chi^2_{min} + 1$.

5.3.2 Pulse Cleanup

Due to random noise in the electronics, only pulses above 50 ADC units are saved, and only sub-peaks above 25 ADC units are saved. The fit charge of

the sub-subpeaks are uniformly scaled to match the measured pulse charge. This rescaling ensures consistence between the total pulse charge and the sum of the fit fit charges.

5.3.3 Large Pulses

Beyond 10 PE, the ability to accurately resolve sub-peaks is greatly diminished. This diminished performance is primarily due to loosing the ability at resolving the individual SPE peaks. For pulses with charge larger than 3000 ADC units ($\sim$10 PE), the charge integral between the valleys that separate the sub-peaks is used to define the charge of the sub-peaks. Figure 5.5 shows a large pulse with the reconstructed pulse shape overlaid. Despite the large discrepancy in the peak heights between the measured and reconstructed peaks, the total integral is conserved and thus does not degrade the energy resolution of the experiment.

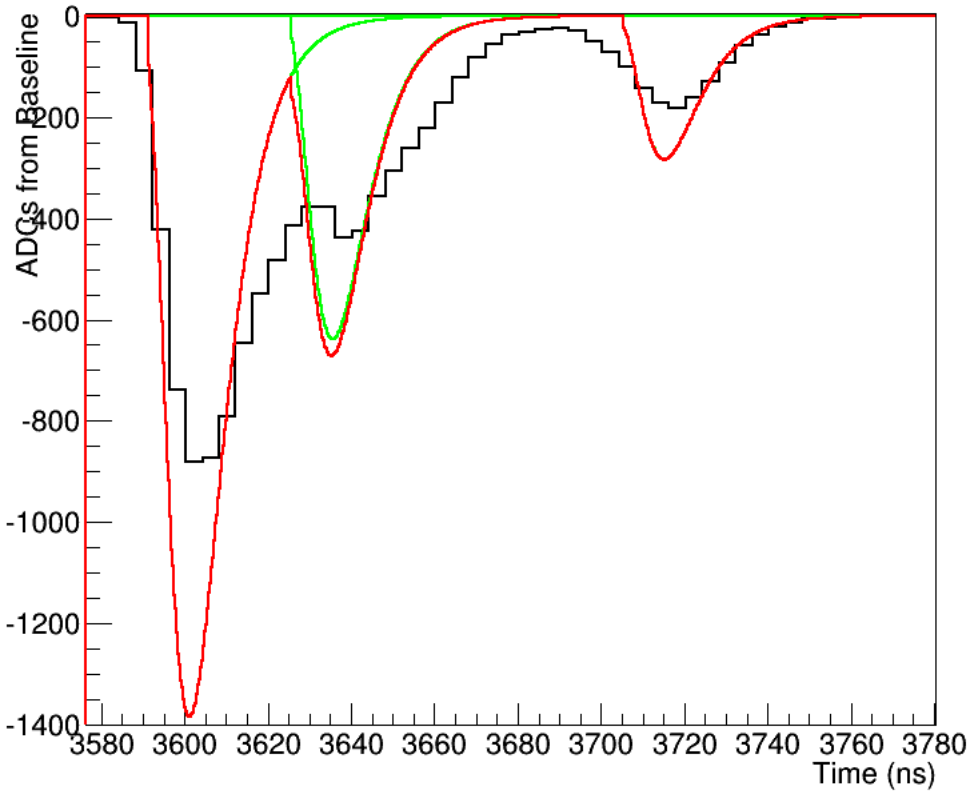

Figure 5.5: Example of a large pulse where the sub-peaks are not fit, instead the sub-peaks are given the charge of the pulse integrals from valley-to-valley.

Chapter 6

SmartQT Data Compression

With the sizeable ^{39}Ar event rate, the amount of data generated is substantial compared to the experiment's allocated storage. Classes of events that are outside our WIMP ROI are pre-scaled to reduce the amount of data and stay within the storage confinements. This pre-scaling means that only a fraction of the events that trigger the detector have their full information saved to disk. The amount of pre-scaling is minimized by first applying a method of data compression through SPE identification. This compression method is called SmartQT.

6.1 Overview

The SmartQT algorithm is executed within the event builder before data are written to disk. The algorithm performs a pulse finder search identical to the offline analysis as discussed in Chapter 5, with the exception that pulses are not split into sub-peaks. As the pulse finding is performed, five pulse

observables are measured: Charge, Minimum Voltage, Minimum Derivative, width, and ChargeFrac defined as:

$$\text{ChargeFrac} = \frac{\int_{t_{\text{start}}}^{t_{\text{max}}} f(t)}{\int_{t_{\text{max}}}^{t_{\text{end}}} f(t)}. \tag{6.1}$$

Here t_{start} is the pulse start time, t_{max} is the bin of the pulse's most significant peak, and t_{end} is the end time of the pulse. These variables are compared to cumulative distribution functions (CDF)s for SPE-like pulses to decide if the pulse trace or only simple pulse information is to be saved.

6.2 CDF Generation

An oscilloscope (LeCroy, WaveRunner) was used the average pulse shape and to characterize the shape parameters of SPE pulses. The average pulse shape is iteratively resolved by aligning the leading edge of the pulses with a linear extrapolation between the 0.4 ns samples. The first round of alignments were performed with all single peaked pulses. Subsequent iterations are performed where the individual pulses are compared to the average pulse shape from the previous iteration. Pulses with large charge residuals are excluded from the next average pulse. Figure 6.1 shows the resulting pulse shape.

Once the average pulse shape was defined, individual scope pulses are examined for the amount of deviation in the pulse shape by fitting each pulse to the sum of two average pulses. These double pulse fits were used to define the amount of variation in pulse shape for the average pulse. These fit parameters were fed into a MC where random pulses were generated and artificially digitized to reproduce digitized pulses. The pulse observables for these

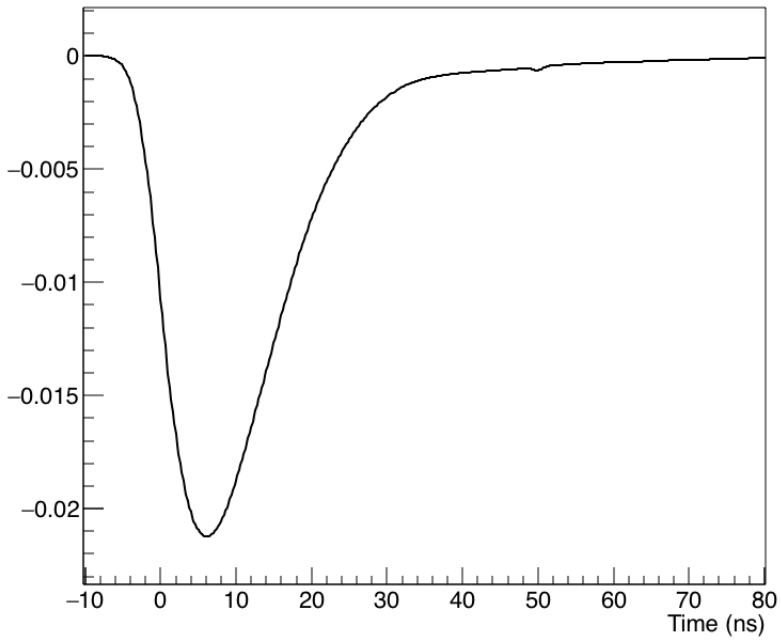

Figure 6.1: Pulse shape generated by aligning leading edge of individual pulses measured by a LeCroy WaveRunner oscilloscope.

artificial pulses were then measured and used to create CDFs for the pulse shape parameters. Figure 6.2 shows two example CDFs used in the SmartQT algorithm.

6.3 SmartQT performance

There are two critical factors for evaluating the performance of the SmartQT algorithm; the first is to determine how well the algorithm can tag pulses that are SPE pulses; the second is to determine how often a double pulse is labeled as a SPE pulse.

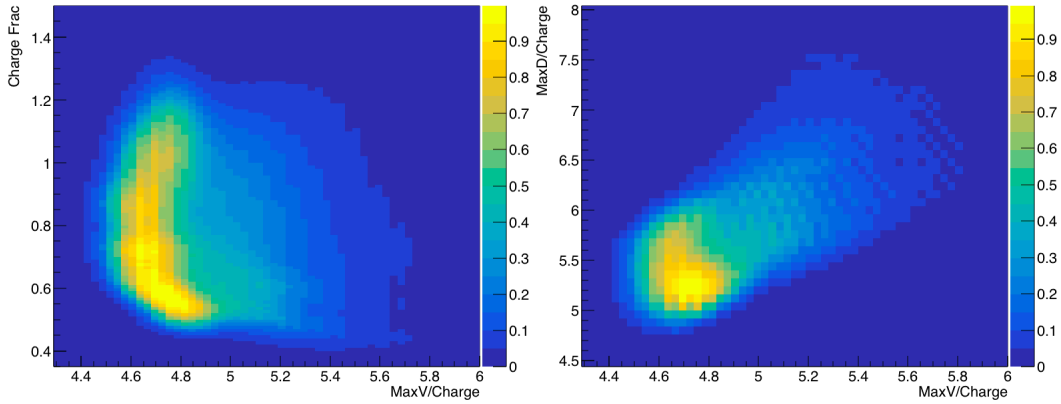

Figure 6.2: Examples of the 2D CDFs used in the smartQT data reduction algorithm. The CDF for the ChargeFrac vs. MaxV/Charge is shown (left) and the CDF for the MaxD/Charge vs. MaxV/Charge is shown (right).

6.3.1 SPE Identification Efficiency

The SPE identification efficiency for this study is the fraction of pulses SmartQT identified at the peak charge in the SPE charge spectrum. Using low-intensity data taken with the laserball, the charge of SPE identified pulses is compared to the charge of all pulses. Since the laserball was operated at low intensity, the amount of pulse pile-up that would generate a pulse at the SPE mean charge is very low. All pulses at the SPE charge peak will be considered to be SPE pulses. With this definition, the primary background is due to double pulsing in the PMTs, which is at the level of 3%. Figure 6.3 shows an example of the measured charge spectrum and the spectrum of SmartQT identified SPE pulses. Also shown is the distribution of the SPE identification efficiency for the PMTs.

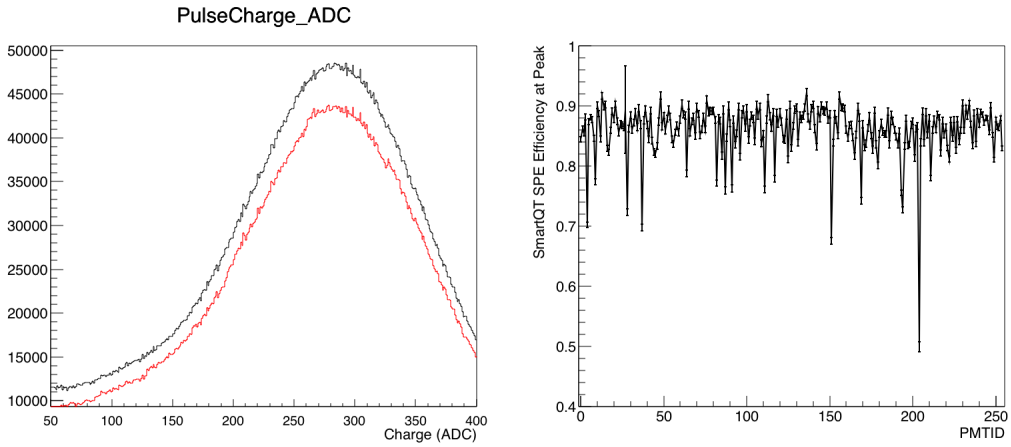

Figure 6.3: The ability of the SmartQT algorithm to identify SPE pulses. An example of a PMT's charge distribution for all pulses (black) and SPE identified pulses (red) is shown (left). The ratio between all pulses and SPE identified pulses, used as a measure of the SmartQT efficiency is shown (right).

6.3.2 SPE Misidentification Rate

To evaluate the types of pulse pile-up that are misidentified as SPE-like pulses, a MC was produced to overlap two pulses with varied charge and separation, to artificially digitize and then evaluate the pulses. Figure 6.4 shows the efficiency of the smartQT algorithm to correctly identify the pulses as non-SPE-like pulses. In contrast, the ability of the pulse finder algorithm to distinguish the two peaks is also shown. The bottom plot in Figure 6.4 shows an example standard single SPE pulses along with pulses separated by 7 ns and 18 ns; which are where SmartQT and SmartCal are respectively 90% efficient at tagging equally charged pile-up pulses. The significant differences in the resolution of the two algorithms for pulse pile-up identification provide confidence that the analysis will be identical with and without the SmartQT compression. The low efficiency of the upper and lower limits of the fractional charge is due to the pulse clean-up mentioned in Section 5.3.2.

6.3.3 Data Reduction

The goal of the SmartQT algorithm is to compress the data. On a pulse-level, for every pulse saved as a smartQT pulse, the size of the data is reduced by the size of the RawBlock data class. Comparing the total saved data size between a SmartQT and nonSmartQT pulse, there is on average reduction factor of $\sim$75%. On the event level, due to the actual rate of SPE pulses and efficiency of the algorithm, this provides an overall reduction of $\sim$45% for events below 500 QPE. Figure 6.5 shows the QPE spectrum for a data run with low-level cuts applied. The two curves show the energy spectrum with and without correction for the pre-scaling. With the SmartQT reduction, 100% of the events below $\sim$ 400 QPE are kept.

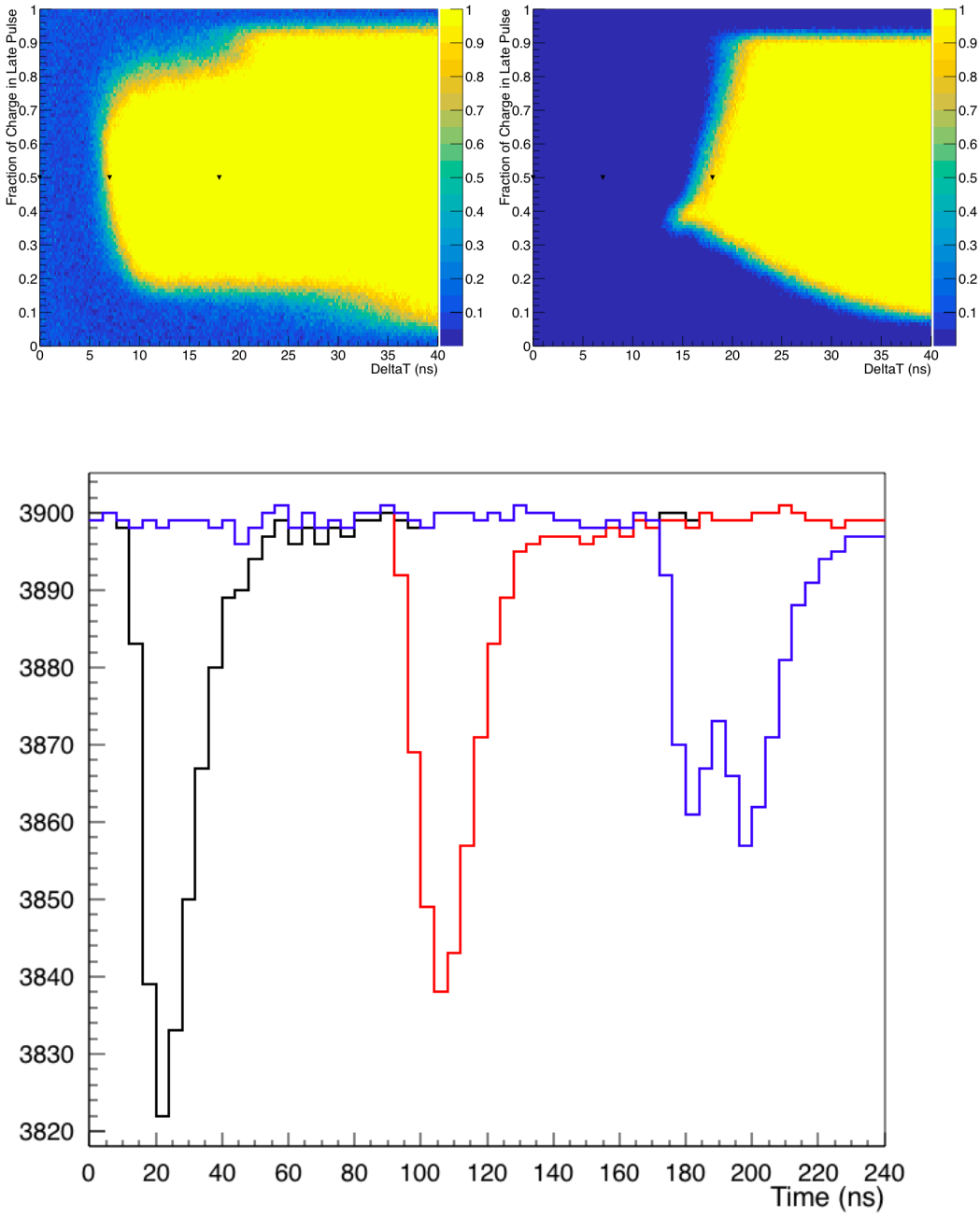

Figure 6.4: Efficiencies for the smartQT algorithm to identify pile-up pulses (top,left) as well as the efficiency for the peak finder to identify pile-up pulses (top,right). Sample pulse shapes for the pile-up parameters shown in the black triangles in the efficiency plots (bottom). The sample pulse pile-up is shown for zero time separation (black), 7 ns separation where SmartQT becomes 90% efficient (red) and 18 ns separation where SmartCal becomes 90% efficient (blue).

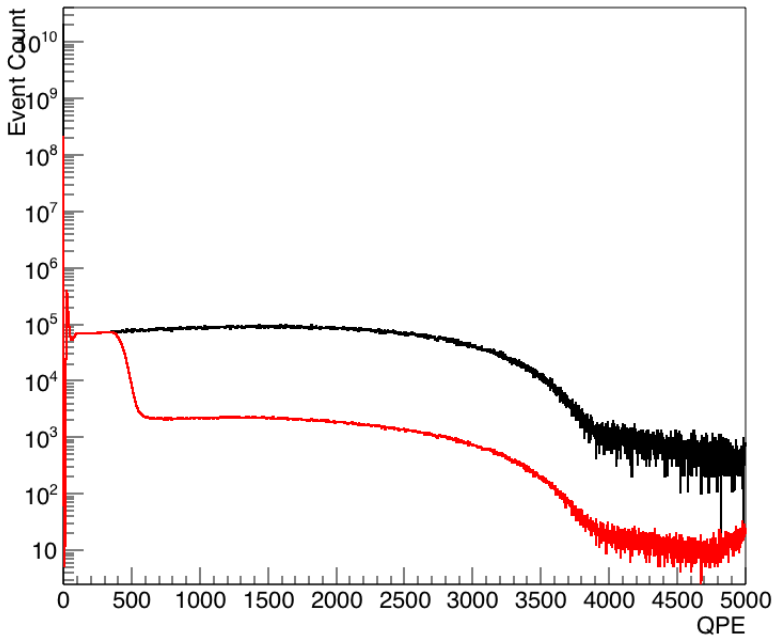

Figure 6.5: Raw event energy spectrum with only basic low-level cuts applied. The spectrum is shown with a correction for the amount of pre-scaling (black) and without correction (red).

Chapter 7

RAT Optics Tuning

The optical properties of the detector play an essential roll in being able to understand measured quantities in the data, and is therefore critical for the reconstruction of event positions. The main RAT simulation is used to model particle interactions in the detector. While this package accurately simulates particle interactions, the accurate propagation of optical photons requires many optical parameters which are not strictly defined. The optical parameters within the RAT code are difficult to decouple and isolate. For this reason, a simplified MC was created, starting from very basic parameterized optical model. This model was gradually improved until a full physical optical model was created. This toy MC was used to evaluate the optical parameters that strongly influence the characteristics of the detector. Once these key elements were identified, they were updated and tuned in the RAT simulation. By writing an optical model from first principles, every optical parameter that was put into the model was re-evaluated without any assumptions as to the validity of the parameters initially implemented in the RAT simulation. This

secondary validation of the critical optical parameters and models was a crucial process in improving the optical model. The focus of this chapter will be on this second round of optical tuning with RAT for the parameters that the Toy MC found to be highly influential in the characteristics of the optics. For detailed information on the Toy MC refer to Appendix A.

7.1 Optics in Data

There are several ways through which the optical behaviour of the detector can be viewed in data. One of our most robust handles on the optics is from the optical calibration sources. The original optical studies were performed entirely with the laserball data. However, the laserball was left out of the optical tuning once the optical model became too complicated to do simple parameter fits, as discussed in Appendix A. The optical tuning discussed here used the AARF data in both the empty and partially filled detector. The AARF data is particularly sensitive to changes in the optical behaviour of the LGs and the properties of the TPB.

The optics of the detector can also be seen in the ^{39}Ar data by looking at several key variables. The primary variable that was used to observe how the optics were behaving is the $\text{fMaxPE}_{\text{prompt}}$, a value highly dependent on the properties of the TPB. The second variable that is observed to correlate straight with the optical parameters is the measurement of NHit; the number of PMTs that observe light within the -28 ns to 10 μs time window around the event time. While $\text{fMaxPE}_{\text{prompt}}$ deals with the characteristics of the highest charge PMT, NHit looks at how the light fits the rest of the PMTs in the

detector, and is sensitive to the amount of and distribution of backscattered and back fluoresced photons from the TPB.

For the optical tuning, data and MC distributions were made for the following datasets:

- AARF in an empty vessel
- AARF with LAr level at 550 mm
- ^{39}Ar at the 550 mm fill level

The optical parameters were then tuned in the MC until a reasonable agreement between data and MC was achieved.

7.2 Parameter Tuning

The parameters that are updated in this study are split into two sets. There is a group of parameters that were merely updated to more recent literature values without additional manipulation. For these parameters, initial checks with the Toy MC were made that slight shifts in the scales of these parameters that did not strongly affect the optics. The primary group of parameters in this category are those of the optical properties of the LAr.

The second set of parameters that were updated in this study are those that the values are not explicitly known, or those where the literature value is believed to be unreliable. In general, these parameters were found to strongly influence the optical characteristics in the Toy MC. These parameters were related to the properties of the TPB and the LG reflectors.

The following sections will describe the updated optical parameters in the RAT Simulation and explain why specific values were chosen. At this point no errors have been assigned to the tuned optical values. This is a currently an on-going task in the collaboration; including assigning reasonable errors to the optical parameters and evaluating the result systematic uncertainty in the position reconstruction.

7.2.1 Liquid Argon Optics

The original optical parameters for the LAr were taken from relatively old references [109], and many of the parameters were extrapolations from a few data points. There were also some parameters with unknown origin and motivation that were updated to better reflect actual measurements.

The original values for the index of refraction of LAr were taken from [109] which were extrapolated down to 130 nm and assumed constant below this wavelength. The original Rayleigh scattering length for the LAr was 90 cm at 128 nm [110], which was then extrapolated assuming a pure $1/\lambda^4$ wavelength dependence. For the LAr scintillation spectrum, a Gaussian distribution with 20 nm standard deviation (σ) was assumed centred at 128 nm. No motivation for the chosen σ has been found. These values were all updated for the optics; the index of refraction in the LAr were taken from fits to the Sellmeier coefficients [111], allowing for a theoretical calculation of the index of refraction down to the VUV spectrum. The wavelength dependent index of refraction

could then be used to compute the Rayleigh scattering length via [94]

$$l_r^{-1} = \frac{16\pi^3}{6\lambda^4 N} kTNk_T(\frac{(n^2-1)(n^2+2)}{3}). \tag{7.1}$$

Here k_T is the compressibility of the LAr and N is the number density of Ar atoms (N in the numerator and denominator cancel in the limit of small compressibility). This equation results in a Rayleigh scattering length of 66 cm at 128 nm, consistent with the measured value 66±3 cm [112]. Figure 7.1 shows the old and new values for the index of refraction and Rayleigh scattering length in RAT.

The LAr scintillation spectral shape was updated to match the various measurements of the spectrum [71] [72]. Figure 7.2 shows a compilation of multiple measurements of the LAr spectrum. As can be seen, there is very little agreement between the measurements, particularly in the long wavelength tail. For this reason, the implemented spectral shape was taken merely to be a rough match to the peak of the spectra with a σ of 6 nm centred at 128 nm. It is likely that the majority of the long wavelength tail is dominated by the amount of contaminants in the measured Ar sample, particularly the levels of xenon and oxygen.

7.2.2 Light Guide Reflector Efficiency

The LG reflector efficiency (ϵ_{LGr}) represents the ability for the LGs to reflect photons back into the LG when they are not total internally reflected at the acrylic/air interface. The RAT simulation used the measured complex index of refraction to describe the reflection and absorption of photons from the

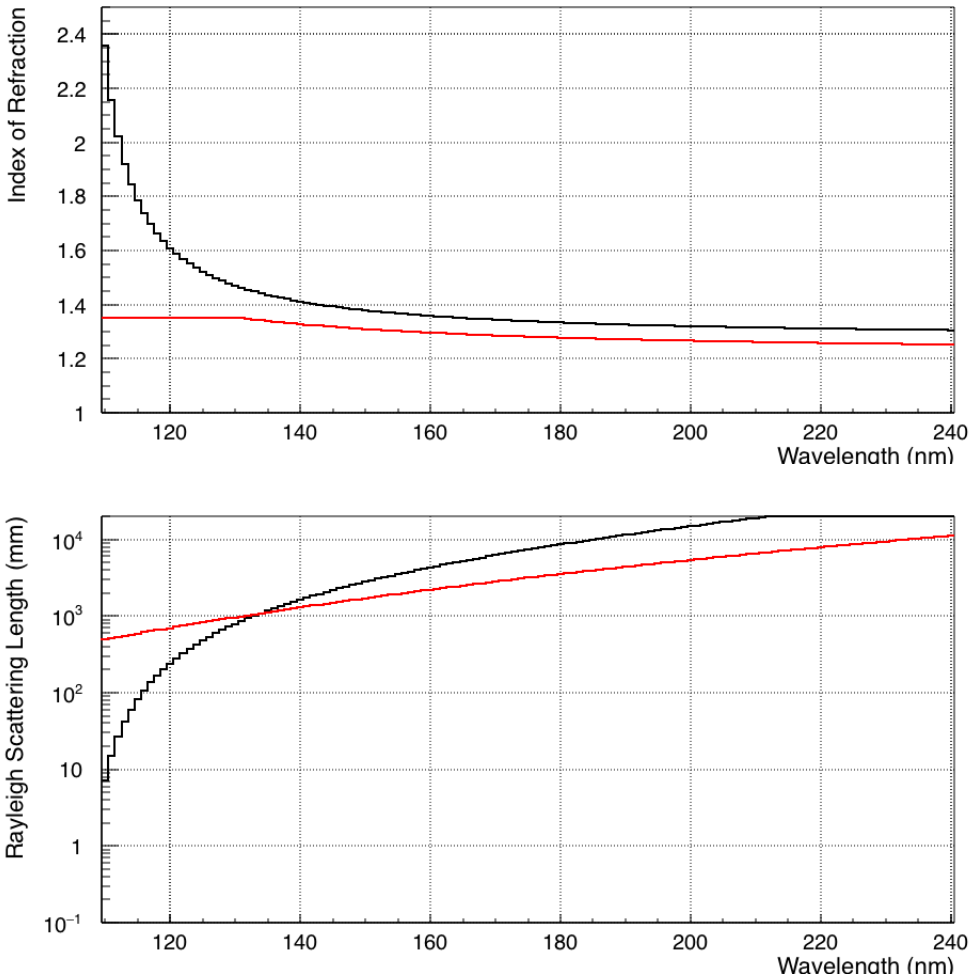

Figure 7.1: (Top) Index of refraction of the LAr (black) Index of refraction from 90K Sellmeier coefficients coefficients [111]. (red) extrapolated values from [109] and assumed constant below 130 nm. (Bottom) Rayleigh scattering length for LAr. (black) computed using 7.1 and the index of refraction from [111]. (red) extrapolated of 90 cm at 128 nm assuming a pure $1/\lambda^4$ wavelength dependence.

reflector. In early simulations, this was found to inadequately reproducing optical characteristics of the LG photon transport. It was instead switched to a simple single parameter probability for the light being reflected over being absorbed. This probability is then a tuneable parameter that can be adjusted to better match the optical parameters. It was found that a reflection prob-

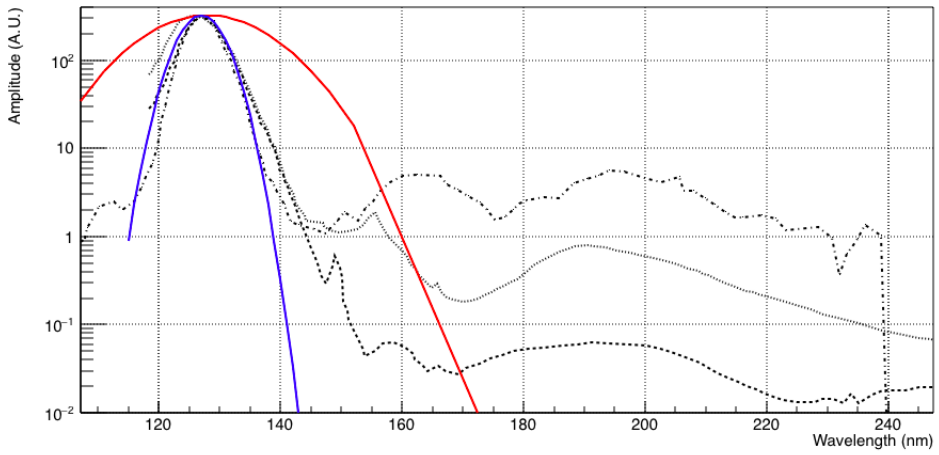

Figure 7.2: Measured spectra of Ar scintillation for (3x black) measured spectra from Figure 2.2, original LAr spectrum in RAT (red), and new spectrum implemented in RAT (blue).

ability $\epsilon_{LGr} < 0.6$ is preferred. Figures 7.3 and 7.4 shows the effect that ϵ_{LGr} has on the $FMaxPE_{prompt}$ and AARF intensity distributions. The plots show little effect on the characteristics of the LAr. For the AARF charge distributions, ϵ_{LGr} primary effects the ratio of light seen in the PMTs closest to the AARF PMT favouring; lower values of ϵ_{LGr}. Little difference is seen in the distributions for $\epsilon_{LGr} < 0.6$, in this study $\epsilon_{LGr} = 0.6$ is used.

7.2.3 TPB Scattering

The optical parameters of the TPB are challenging to constrain. Not all of the literature values agree on its properties, particularly the scattering of the optical light within the TPB. For the sake of simplicity, it is assumed that the scattering length is independent of wavelength. While this is not, in general, correct the primary light that passes through the TPB is between 400 nm and 500 nm over which the variation is expected to be small enough that

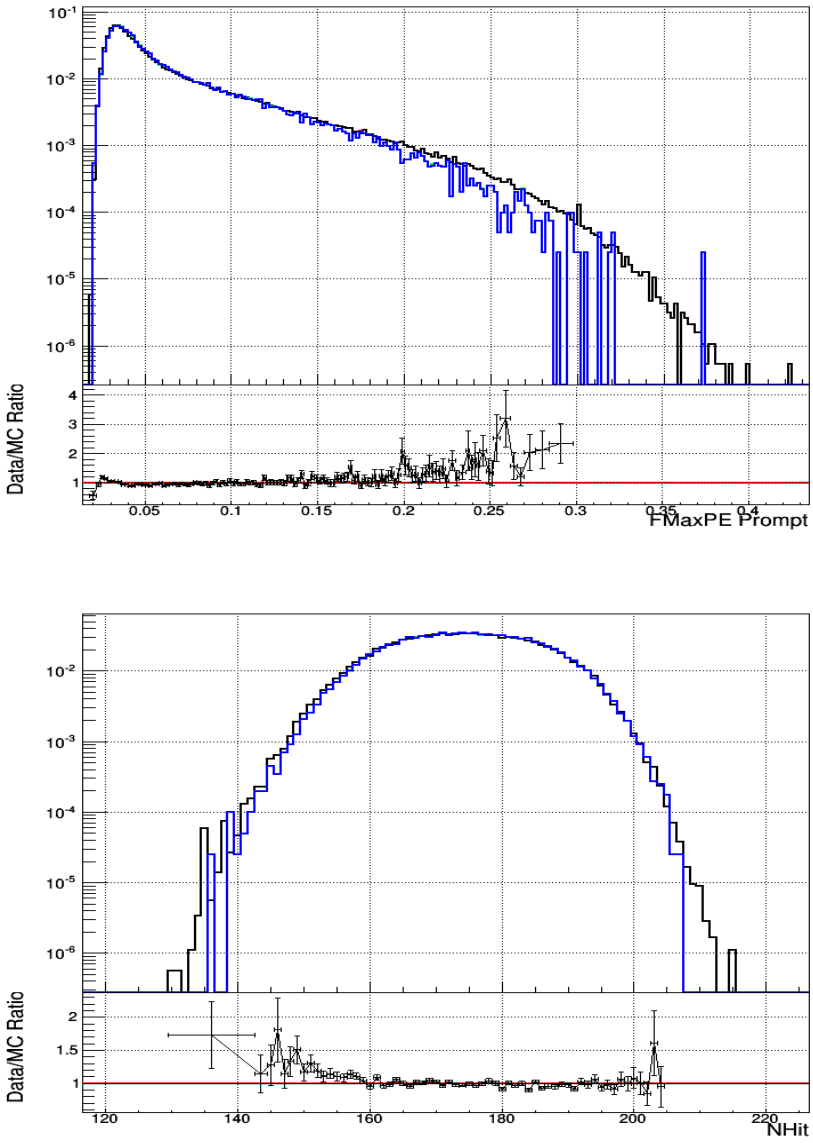

Figure 7.3: Comparison between ^{39}Ar data and RAT simulation for events with energy 390<QPE<410 PE with varied LG reflectivity. The FMaxPE$_{Prompt}$ distribution (top) and NHit (bottom) are shown. In both plots the data is shown in (black), $\epsilon_{LGr} = 0.6$ (red), $\epsilon_{LGr} = 0.3$ (green) and $\epsilon_{LGr} = 0.8$ (blue). The simulations show no difference in the FMaxPE$_{Prompt}$ and NHit distributions for the different ϵ_{LGr}. The data/MC plot is only plotted in the range that MC data exists.

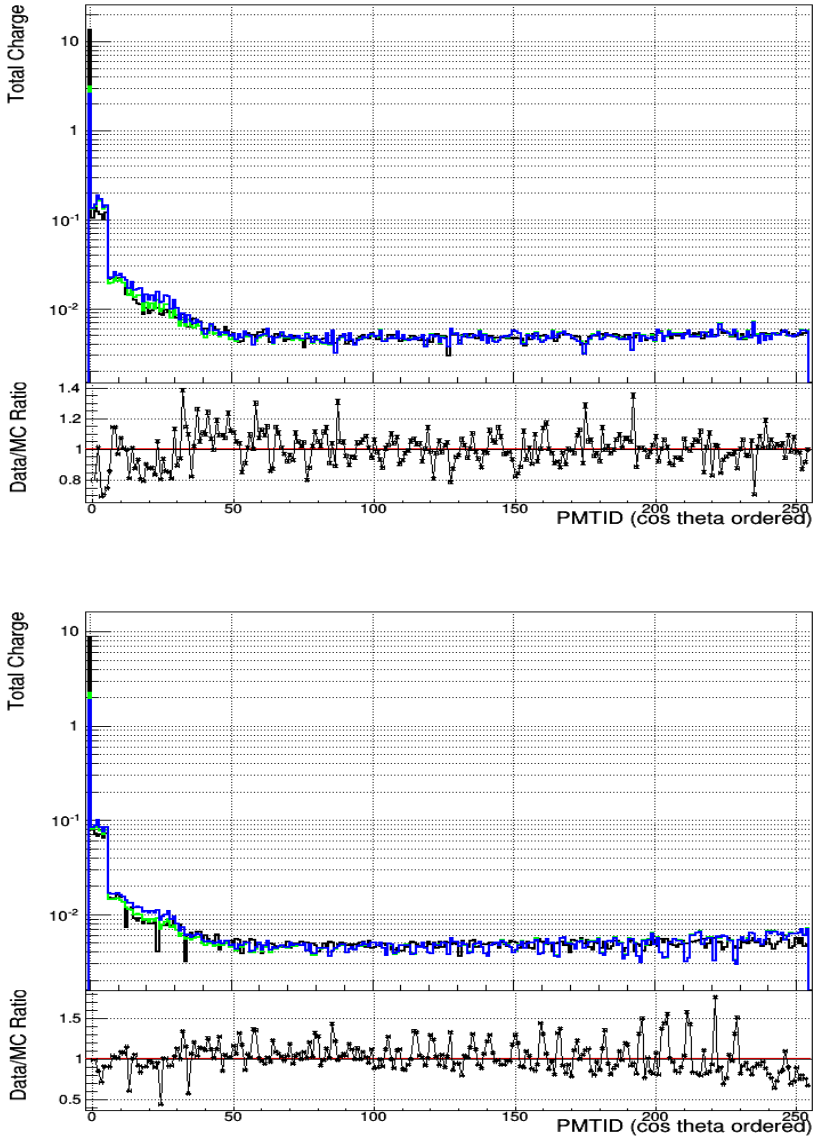

Figure 7.4: Comparison between AARF data and RAT simulation for the light distribution with various LG reflectivities. The AARF charge distribution in Empty vessel (top) and 550 mm LAr fill level (bottom). In both plots the data is shown in (black), $\epsilon_{LGr} = 0.6$ (red), $\epsilon_{LGr} = 0.3$ (green) and $\epsilon_{LGr} = 0.8$ (blue). AARF PMT is not included in the Date/MC ratio plot.

this approximation is valid. The scattering length in the TPB has not been widely discussed in the literature. The only dedicated analysis gives a scatter-

ing length between 2 and 3 μm at 420 nm [113]. However, there are a number of measurements of the relative transmittance of light through varying thicknesses of TPB that is highly coupled to the scattering length [114] [115]. These relative transmittance measurements suggest scattering values that are much longer than 3 μm. Running a simple MC for 420 μm light traveling through various thicknesses of TPB it quickly becomes apparent that, with a 3 μm scattering length, thick layers of TPB would appear opaque. This result is in sharp contrast to observations of relatively little difference in the transmittance between thin and thick TPB layers [114] [115]. Figure 7.5 shows the comparison between two measurements of the relative intensity and the results from the MC. The figure shows a scattering length on the order of $\sim$150 μm to be consistent. This is also in agreement with what was seen with the Toy MC as shown in Appendix A. The original value used in RAT was 1 μm for all wavelengths. The TPB scattering length is likely the primary cause of optical discrepancies in the initial simulations.

There are many reasons for why the effective scattering length of the TPB may vary for different samples. One possibility is that the scattering in the bulk of the TPB is highly correlated to how the TPB crystals grew during the vapour deposition. The crystal formation may also have strong correlations to the topology over which they are grown. Sanded acrylic vs a polished glass substrate. It is also likely that there is strong degeneracy between the observed behaviour being caused by reflections and scattering at the TPB surface over scattering within the TPB bulk volume. Since the two measurements are consistent with long bulk TPB scattering lengths are relative intensity measurements, the surface effects are normalized out while the mea-

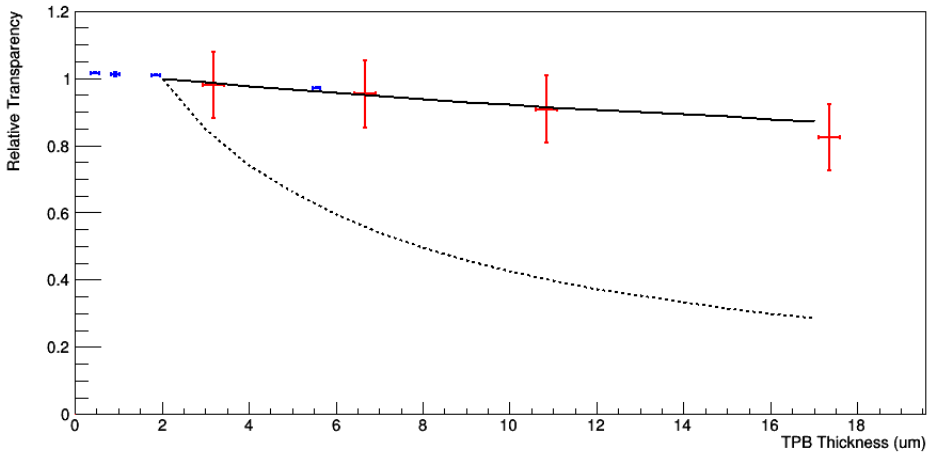

Figure 7.5: Measurements of the relative transparence of TPB layers at different thicknesses from (blue) [114] (red) [115] along with results from the simple scattering MC for (black solid) 150 μm and (black dashed) 3 μm scattering lengths.

surement done in [113], as well as the tuning done here, only the overall effect is observed. The final tuned value for the scattering length of TPB was 3 μm. Figures 7.6and 7.7 show the comparison between data and MC distributions for the different scattering lengths of TPB.

7.3 Remarks on PMT Timing and Optics

The detector optics tuning has in general, performed well in matching the key characteristics in the data. However, at this point this should only be seen as a first order accomplishment, that results in a greatly improved position fitting. Figure 7.8 shows the r^3 distribution comparing the position fitting with the new and old optical models. The prominent large radius bias has been removed.

There remain many features in the simulated optics that continue to dis-

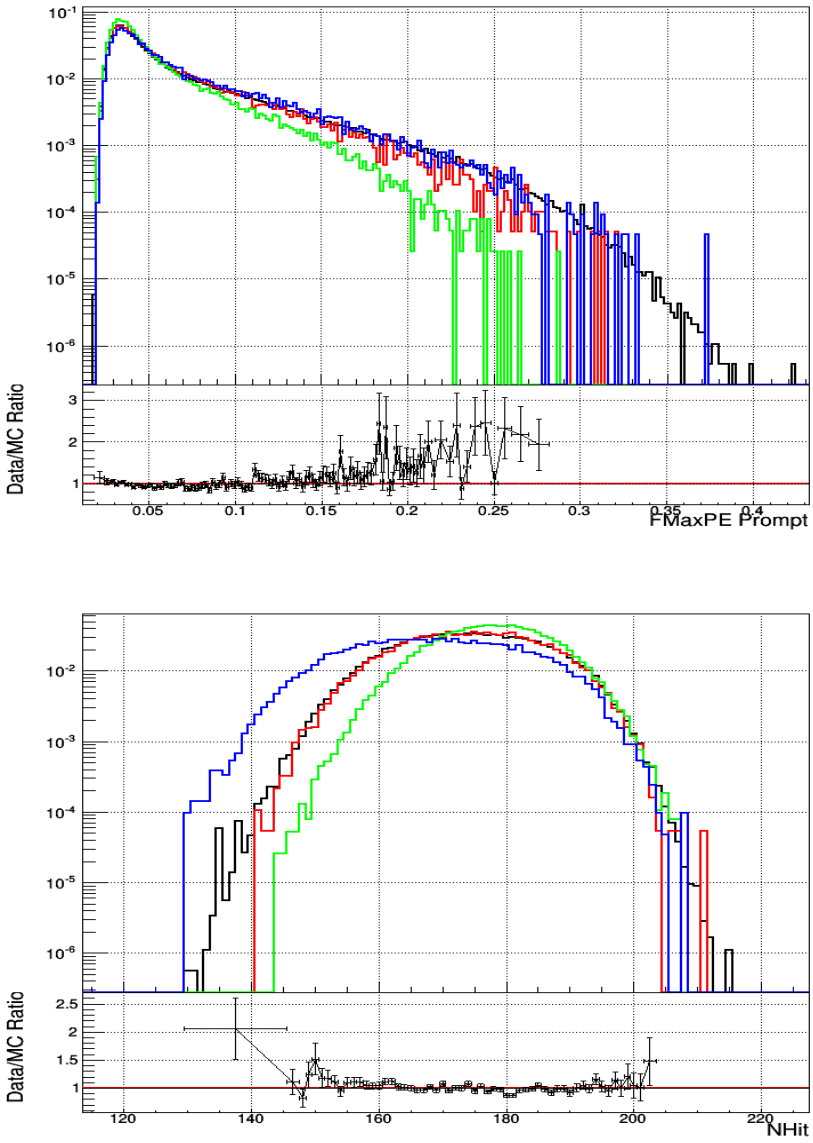

Figure 7.6: Comparison between ^{39}Ar data and RAT simulation for different variable distributions for events with 390<QPE<410 PE with various TPB scattering lengths. (top left) FMaxPE$_{Prompt}$ (top right) NHit (bottom left) AARF Charge distribution in Empty vessel (bottom right) AARF charge distribution with 550 mm LAr fill level. In all plots the data is shown in (black), 3 μm scattering length (red), 1 μm scattering length (green) and 150 um scattering length (blue). The data/MC plot is only plotted in the range that MC data exists.

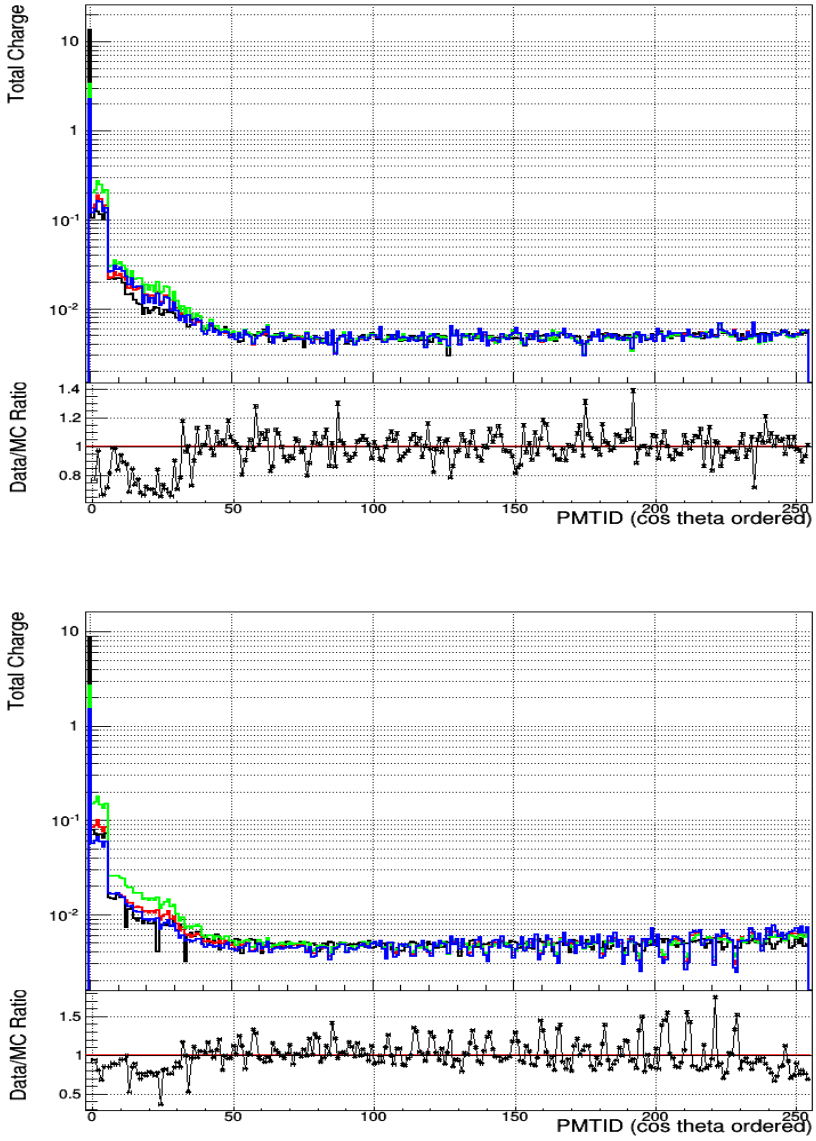

Figure 7.7: Comparison between AARF data and RAT simulation for charge distributions with various TPB scattering lengths. The charge distribution in the empty vessel (top) and with 550 mm LAr fill level (bottom). In both plots the data is shown in (black), 3 μm scattering length (red), 1 μm scattering length (green) and 150 μm scattering length (blue). AARF PMT is not included in the Date/MC ratio plot.

agree with data. One aspect that is currently in disagreement is the PMT time characterization. Much of the optics work performed to date was first motivated by a study of the Toy MC where the optical model only had two adjustable parameters, one for the probability of reflection from the TPB surface and one for the probability of reflection off the PMT face. With a simple PMT time profile, the full time distribution of the laserball data was able to be reproduced in good agreement (samples are shown in Appendix A). This study was repeated using the optical model in RAT. Even with the addition of a more generic PMT timing response function, the laserball timing characteristics were not able to be reproduced. As will be seen in the Section 9, there continues to be an unknown background that currently impedes the WIMP exclusion limit. The optics of the detector need to be further refined with all timing and spacial characteristics well understood to push forward with understanding this unknown background. Several key areas have been found that need further study. They include:

- LG to PMT interface: this detector region is simplified in the RAT simulation. It is likely that this geometry needs to be fully implemented with all materials and volumes. This is motivated by the discrepancy in the AARF PMT seen in the optical simulations, as shown in Figures 7.4 and 7.7. This has also been observed in other optical work performed by fellow collaborators who have had trouble matching the spatial distribution of Cherenkov light in LGs.

- TPB interface: it is expected that there is a strong degeneracy between the surface optical properties of the TPB and the scattering length in

the TPB bulk.

- Neck optics: no part of this study has focused on the optics of light coming from the neck region. Since one of the main candidates for the background events are alpha decays happening within a thin LAr layer on the neck flow guides, the optical properties in this region need to be carefully examined.

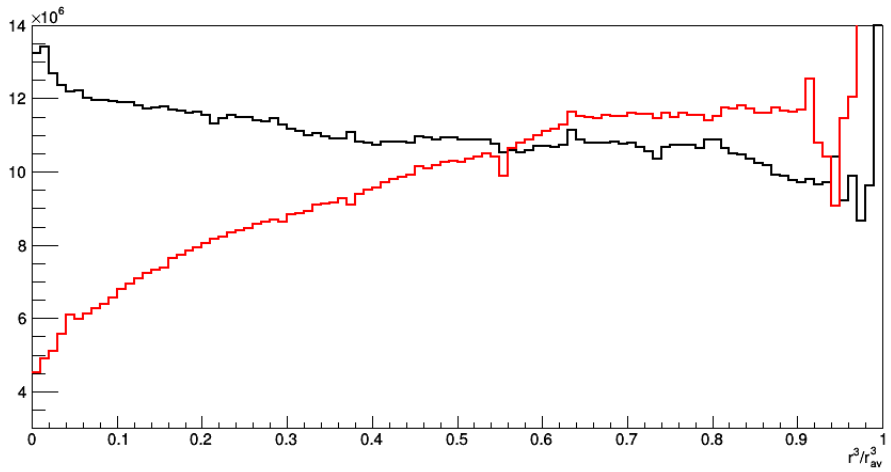

Figure 7.8: Comparison of the $(r/r_{AV})^3$ distributions of ^{39}Ar data using the MBFitter trained with new optics (black) and original optics (red).

It is likely that future optical model tuning, the timing of the photons will become critical in breaking the correlations and degeneracies in the optical model that arose from only using the spatial distribution to tune the parameters. A detailed description of the PMT time response function will need to be formulated, as described in Appendix A, but now using the full optical simulation.

Chapter 8

Multi-Event Identification

A complication due to the high rate of ^{39}Ar decays is pile-up. Pile-up occurs for overlapping multiple events within the same event window. Pile-up can create an issue with the analysis developed here since many of the methods assume only one event is contained in the event window. Some types of pile-up can lead to background events and need to be removed before a WIMP search can be performed.

Several methods have been developed to tag different types of pile-up event. There are two processors that identify pile-up: the first is named Multi-Event, primarily tuned to identify pile-up of two scintillation events. A second is Multi-Site, contains two sub-methods. One sub-method for tagging pile-up that is unresolved by Multi-Event due to a short time separation; a second is tuned to identify pile-up of Cherenkov events with a scintillation event. The following sections will explain these methods in more detail.

8.1 Multi-Event Algorithm

The Multi-Event processor searches for pile-up events by looking at the rate of PMT sub-peaks found in the waveform. All peaks, regardless of charge, are given the same weight in the algorithm. This reduces the false pile-up from large APs. PMTs that see more the 50 PE within the waveform are left out of the Multi-Event algorithm since PMT effects, such as overshoot (shift in the PMT baseline directly after large pulses), can create multi-event like features. The Multi-Event algorithm searches events for statistically significant increases in the pulse count. Binning the event's sub-peak times, the derivative of the binned data is then used to compute a significance value of:

$$\sigma_{dN/dt} = \frac{dN}{dt} / \sqrt{\langle N_{\text{ave}} \rangle} \tag{8.1}$$

Here $\langle N_{\text{ave}} \rangle$ is the average number of sub-peaks in a window around the time bin. The algorithm is first uses 100 ns bins, and later 10 ns bins for events that only have a single event after the coarse pass. In both the coarse and fine event searches, the time bins overlap with the bins on either side so that every sub-peak is added to two bins, slightly smoothing the waveform and reducing statistical fluctuations.

An event is triggered if dN/dt and $\sigma_{dN/dt}$ cross thresholds. A secondary event can be found after at least one bin with $dN/dt < 0$ has been reached after the last event. Figure 8.1 shows a sample event waveform and the derivative significance value. Although the secondary event is much smaller than the first event, Multi-Event identify see the second event without false triggers on the large pulses also in the event.

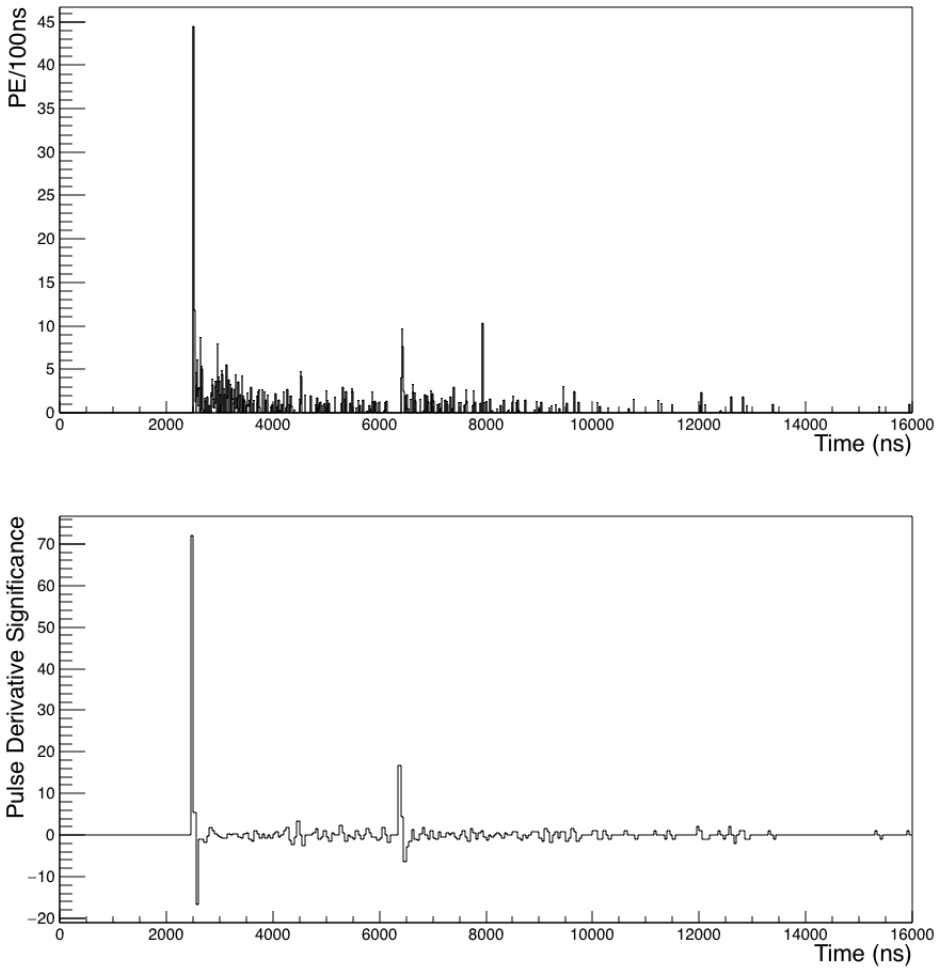

Figure 8.1: Pile-up example event that is seen by Multi-Event. The binned waveform with charge weighting on the pulses is shown (top). The significance of the derivative used to tag the start of events is shown (bottom). The third large peak in the waveform is due to afterpulsing and is not visible in the significance of the derivative due to it being from a single pulse.

In the case that no events are found within the first 3000 ns of the waveform, additional logic is applied. Since the trigger will typically put events at ∼2500 ns, there are only two scenarios that will not give an event before 3000 ns. The first is if the event is from a monitoring trigger; a periodic trigger where the event can be anywhere in the waveform. The other is the event was not

large enough to satisfy the event finding logic and was missed. In either case, an event is forced at the peak charge time if any charge was measured in the early part of the waveform. Note, this method is not for finding pile-up, but to avoid zero identified events if any charge exists in the waveform.

The last method that Multi-Event uses to tag pile-up is to look at the location of large pulses ($>$ 50 PE) that are larger than those of a typical AP and that are separated by at least 50 ns from the first event. This method is specifically intended to help tag the pile-up of large Cherenkov events. The 50 PE pulse charge limit is above the AP charge cuts off at near 35 PE so that false pile-up events are not created by AP pulses.

Method	Pile-up Description
Coarse Derivative	Standard pile-up finding, finds events with time separations >300 ns.
Fine Derivative	Second order pile-up identification for events that are closer in time. Finds events with time separations >50 ns.
Early Light	If an event is not found in first 3 μs using the derivative method, an event is placed at the bin with most charge. This reduces the occurrence of data events with zero software triggers.
Large Peaks	Single peaks with $>$ 50 PE and time separation $>$ 50 ns are triggered as secondary events. These events are primarily caused by pile-up of Cherenkov light in a single LG.

Table 8.1: Overview of the Multi-Event pile-up identification methods.

8.2 Multi-Site Finding

From the definition of the algorithm, Multi-Event performs poorly at identifying pile-up that is close in time or due to lower energy Cherenkov events. The Multi-Site processor was developed to improve pile-up identification for some fundamental event types that can be a particularly troubling background, mainly ^{39}Ar prompt pile-up with Cherenkov in a LG.

The Multi-Site processor has two methods for identifying prompt pile-up. The first is to compute the FWHM of the prompt pulse. Pile-up of two events that are too close to resolve with Multi-Event will have a broader prompt pulse FWHM, events with significantly broader FWHM prompt peaks can then be identified as pile-up. Figure 8.2 shows the distribution of the FWHM for a typical run with Multi-Event pile-up cuts applied. For slices of QPE, a gaussian is fit to extract the mean and standard deviation (σ), and a cut is placed at 3σ from the mean.

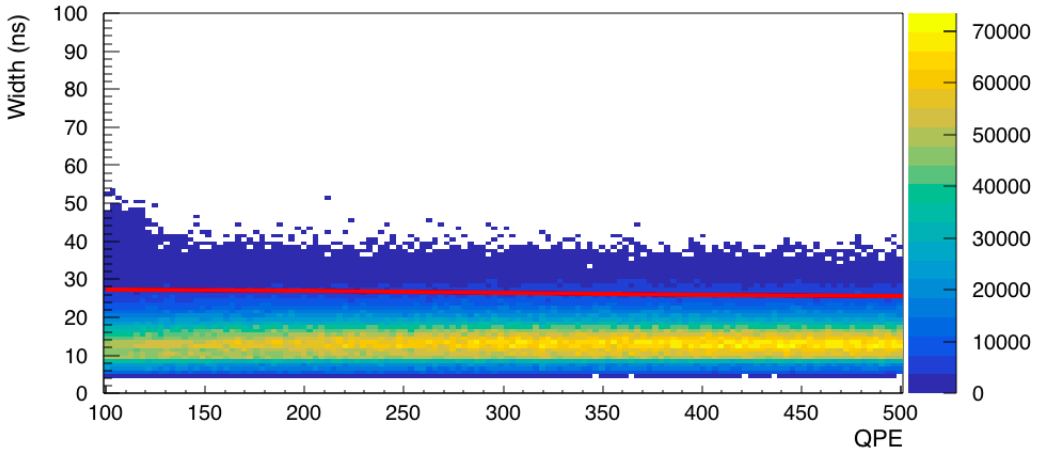

Figure 8.2: The FWHM of the prompt pulse. The cut line in green is the 3σ upper limit to the width distribution.

The second method that the Multi-Site processor uses to identify prompt pile-up exploits the localization of Cherenkov events. If pure Ar scintillation causes an event, then the time distribution of the photons should not vary with PMT location. In contrast, pile-up with a Cherenkov event will have the majority of the Cherenkov photons in a prompt time distribution and highly spatially localized around the interaction point, This makes the event's overall time and charge distribution have a position dependence.

Cherenkov event pile-up is therefore identified by finding localized regions of PMTs that strongly influence the fPrompt of the event. Every PMT is evaluated by removing it and it's nearest neighbouring PMTs from the fPrompt computation (see Figure 8.3). The absolute fractional shift of fPrompt from the exclusion of the PMTs is computed (see Figure 8.4 for events that passed Multi-Event). A cut is placed for 90% acceptance for these events.

8.3 Other Pile-up and Data Clean-up Cuts

Two other cuts are needed to clean the data. The first is to remove events that are piled-up with very-low-energy events. If the first event is from a low-energy interaction and does not register in the Multi-Event algorithm, but a second event occurs late in the event window and is cut off by the digitization window, this can create a false high-fPrompt event. This scenario has been almost entirely mitigated by adding extra logic to Multi-Event, but this secondary cut is kept. The second cut is LateAPFrac, used to remove pure Cherenkov events. This cut is in this study to remove essential high-energy Cherenkov events. This pile-up with low-energy ^{39}Ar events that fail

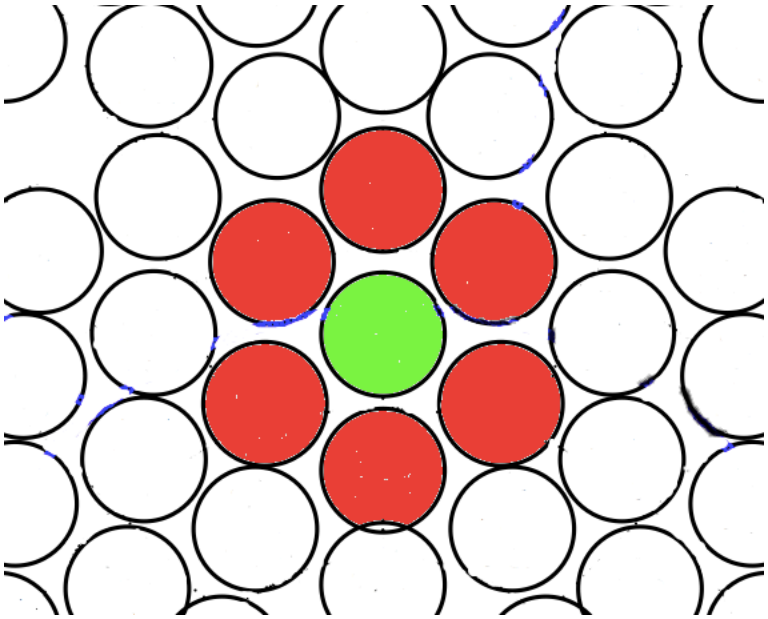

Figure 8.3: Diagram of the PMT nearest neighbours used in the Multi-Site algorithm. The target PMT is shown in green with the nearest neighbours shown in red.

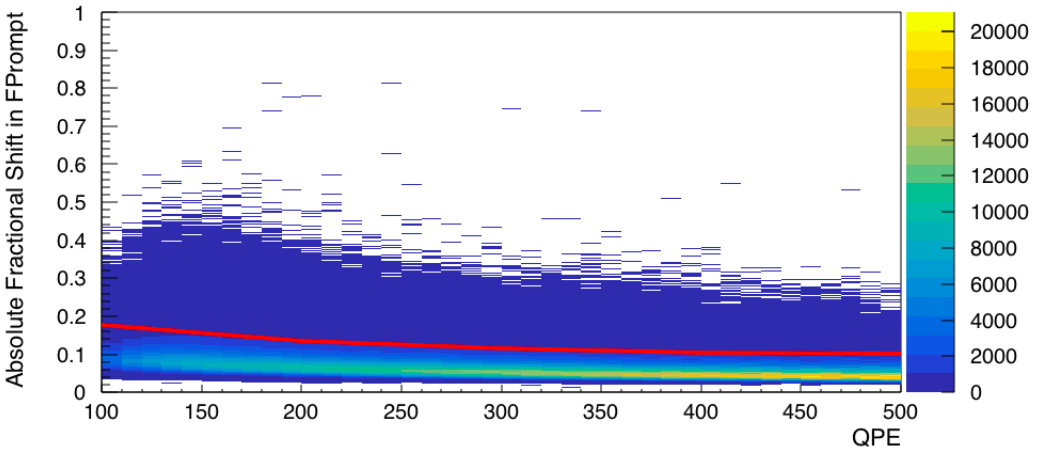

Figure 8.4: The absolute value of the maximum shift in fPrompt from the removal of a local group of PMTs for a sample of ^{39}Ar events. The cut function is shown in green.

to register in the Multi-Event algorithm and do not have enough influence on fPrompt to get cut in the Multi-Site algorithm. These events would appear as

a pure Cherenkov event and may be removed by other means.

A third cut maybe applied, Calibrated Trigger Time (CTT) is the 4 ns time bin with the most integrated charge. For a typical event, this should be within a narrow window around 2500 ns which is where the trigger attempts to place the event. Only accepting events with CCT within the expected window was used to remove some pile-up events before Multi-Event and Multi-Site were developed. This cut will only be included in the pre-Multi-Event pile-up cut to show the improvement over previous analyses.

8.4 Combine Event Pile-Up Simulation

Due to limitations with in the RAT simulation for generating pile-up, a data-driven method was used to evaluate the performance of the pile-up removal algorithms. Simulated pile-up events are created using a program called Combine Event. This program takes two data events and overlaps them with a known time offset. The two events are combined at the pulse-level by first adding pulses of one event to pulses of the other event with a given time offset. The pulses for the new combined event are then re-ordered in time. Sub-peaks that are too close to other sub-peaks are combined based on the double peak resolution (shown in Figure 6.4). The new combined event is then processed through the standard event analysis. The simulated pile-up is then used to evaluate the performance of the Multi-Event and Multi-Site algorithms.

8.4.1 Event Skimming

To simulate specific types of pile-up, "skim files" are made with clean samples of electromagnetic (EM) events and LG Cherenkov events. Events are removed that do not pass low-level cuts, and then specific event types are selected and stored into separate files. Combinations of event types are then run through the Combine Event program to evaluate the abilities of the Multi-Event and Multi-Site processors. To focus on the WIMP ROI, only events that had less than 500 QPE were included in the skim files.

8.4.2 ^{39}Ar-on-^{39}Ar Pile-up

With ∼3.26 kHz of ^{39}Ar events, the pile-up rate of ^{39}Ar within a 10 μs window is 4%, giving on the order of 5×10^9 pile-up events of ^{39}Ar-on-^{39}Ar per year. Of these events, only $\sim$ 2% are caused by two events that both have energy below 500 QPE, giving $\sim 10^8$ pile-up events per year. In total 5×10^8 events where generated totalling ∼5 years of data collection, Table 8.2 shows the results of applying Multi-Event, Multi-Site and additional cuts to the pile-up events. The table shows that the Multi-Event processor is $\sim$ 98.2% efficient at removing ^{39}Ar-on-^{39}Ar pile-up and, as expected, no events enter the WIMP ROI. Figure 8.5 shows the energy fraction of charge in the smaller event against the time difference between the two events at different stages through the pile-up cuts. Figure 8.5 also shows the fPrompt against QPE for the events after the pile-up cuts.

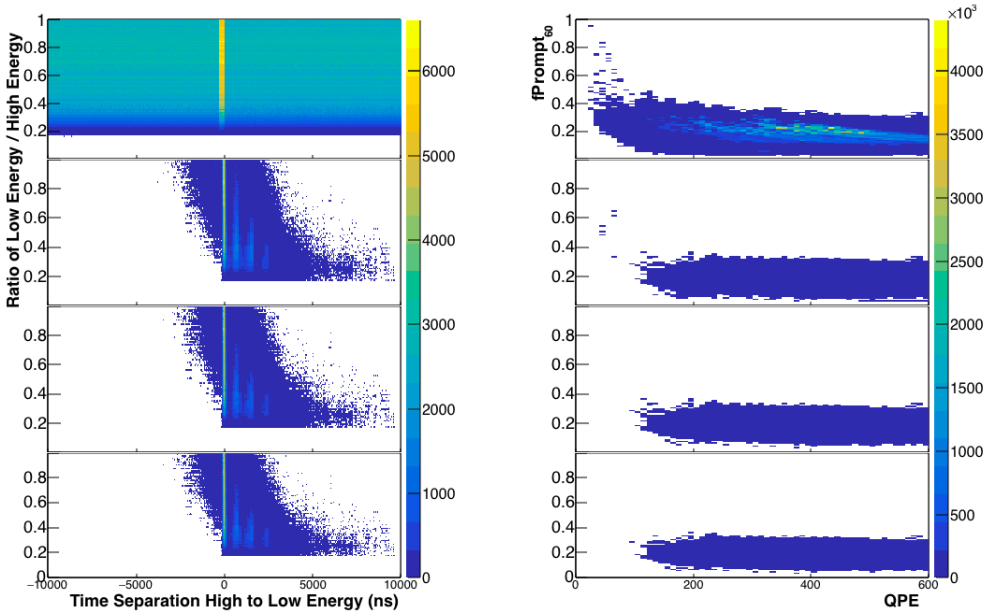

Figure 8.5: (Left) Shows the DeltaT vs relative event QPE for ^{39}Ar-on-^{39}Ar pile-up after different stages of pile-up removal. (Right) Shows the fPrompt vs measure QPE for for ^{39}Ar-on-^{39}Ar pile-up after different stages of pile-up removal.

	No Cuts	Multi-Event	Multi-Site	All Cuts	No Multi-Event or Multi-Site
All	101299479	1800036	1424114	1424105	54246665
0.5<fPrompt<0.9	25	4	0	0	0.4

Table 8.2: Leakage of ^{39}Ar-on-^{39}Ar pile-up per year after different levels of cuts.

8.4.3 Cherenkov on ^{39}Ar Pile-up

Pile-up of Cherenkov light with ^{39}Ar is particularly troubling as it can easily create WIMP ROI events that are difficult to distinguish from high fPrompt scintillation events. A total rate of $\sim$ 10 Hz of gamma ray events. This gives an upper limit of 2×10^6 Cherenkov events piling up with $>$ 500 QPE ^{39}Ar events within one year. In total 1.4×10^8 were generated totalling $\sim$ 54 years

of live exposure. Table 8.3 gives the number of events that survive the pile-up cuts for ^{39}Ar-on-Cherenkov pile-up. The table shows that with Multi-Site applied no leakage is seen. Without Multi-Site tens of events would be seen in one year of data. Figure 8.6 shows the energy fraction of charge in the smaller event against the time difference between the two events at different stages through the pile-up cuts as well as the fPrompt against QPE for the events through the pile-up cuts.

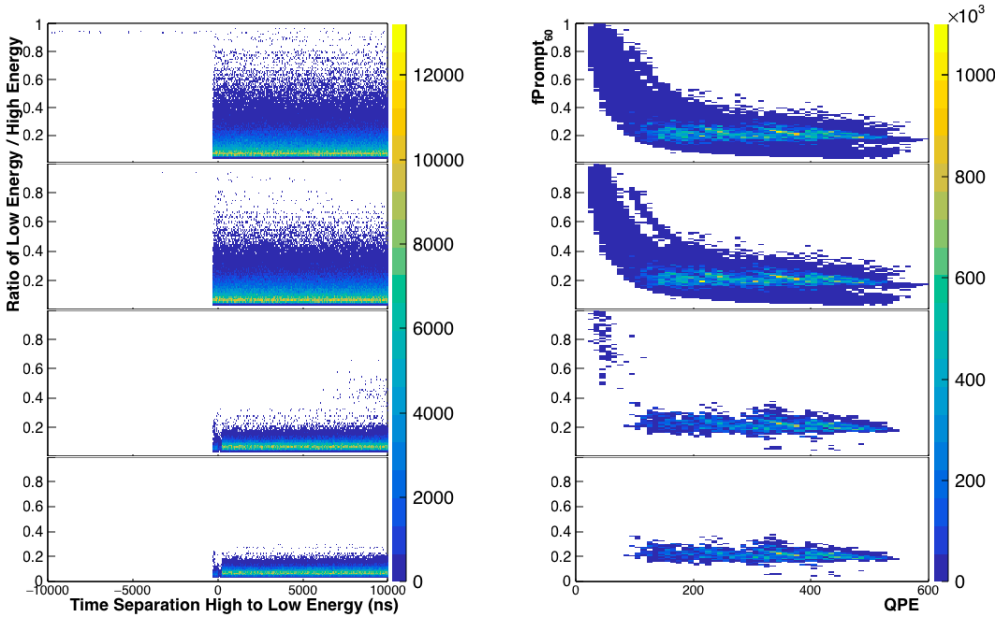

Figure 8.6: (Left) Shows the DeltaT vs relative event QPE for Cherenkov-on-^{39}Ar pile-up after different stages of pile-up removal. (Right) Shows the fPrompt vs measure QPE for for Cherenkov-on-^{39}Ar pile-up after different stages of pile-up removal.

	No Cuts	Multi-Event	Multi-Site	All Cuts	No Multi-Event or Multi-Site
All	2116766	2072051	1262947	1261053	2037132
0.5<fPrompt<0.9	22009	11488	641	0	16

Table 8.3: Leakage of Cherenkov-on-^{39}Ar Pile-Up per year after different levels of cuts.

8.5 Signal Acceptance after Pile-Up and Cherenkov Cuts

One last test on the pile-up removal methods is to evaluate the amount of non-pile-up events tagged and removed by these cuts. The RAT simulation is used to generate sets of ^{39}Ar events and ^{40}Ar recoil events to test the algorithm's rate of false pile-up identification. The pile-up cuts are applied to these events, and the remaining fraction is measured after each cut. Figure 8.7 shows the energy dependence of the acceptance to ^{39}Ar and ^{40}Ar recoil events. The Multi-Event algorithm shows to have an average acceptance of $99.8 \pm 3\%$ for ^{39}Ar and $100 \pm 1\%$ for ^{40}Ar and the Multi-Site cut has an average acceptance of $89 \pm 3\%$ for ^{39}Ar and $92 \pm 1\%$ for ^{40}Ar.

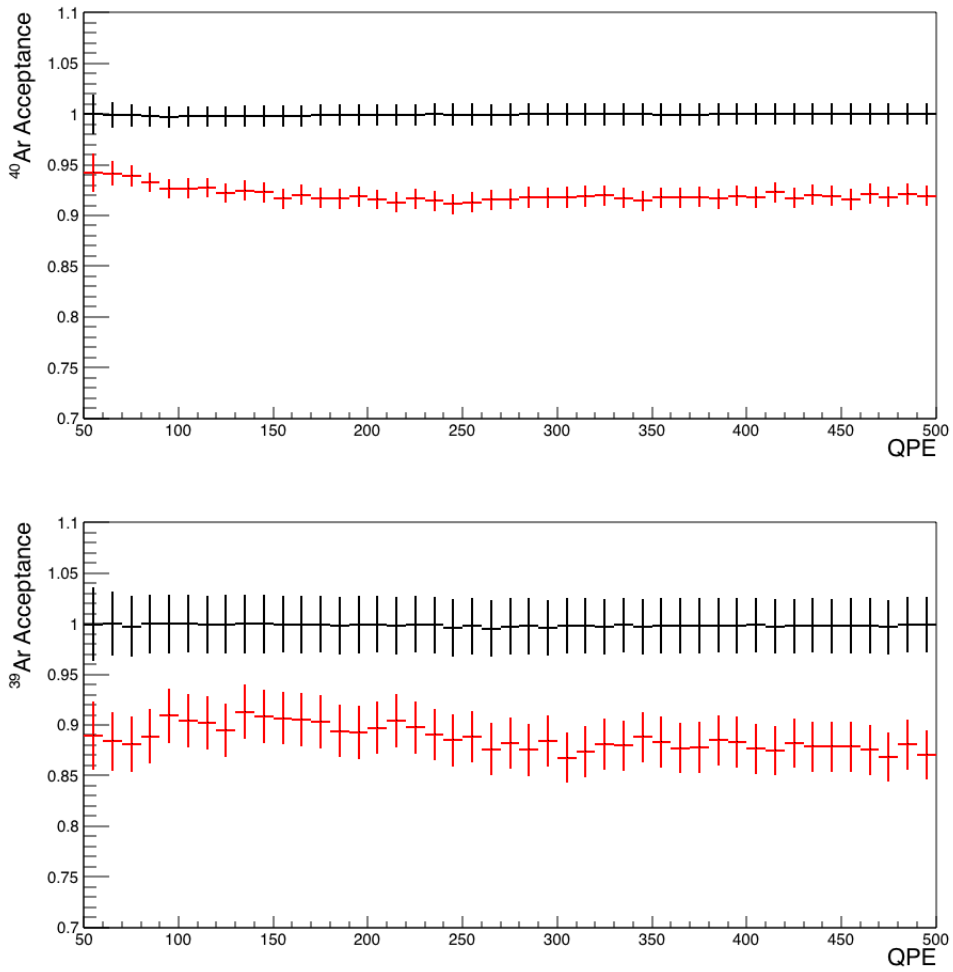

Figure 8.7: The acceptance of ^{40}Ar recoil events (top) and ^{39}Ar decays (bottom) after the Multi-Event (black) and Multi-Site (red) pile-up cuts on simulated data.

Chapter 9

Results and Conclusion

The WIMP analysis performed here considers a period of one year since the completion of the second LAr fill in the detector. The total mass of LAr in the detector during this period is 3257 $\pm$ 112 kg. The presented analysis is non-blind. This chapter will lay out the steps that have been done in taking the processed physics data after all of the cuts are applied to produce a Dark Matter search limit.

9.1 Energy Response

In order to relate the physical recoil energy spectrum to the measured QPE, the energy response function of the detector needs to be determined. Several things fold together to make up the total response. Using the ^{39}Ar spectrum, the components of the energy response function can be fit to the data. The

general response function is broken into three parts. The first is the LY:

$$LY = \alpha + \eta * E + \delta/E, \tag{9.1}$$

where α is the linear term, η is a small quadratic term to account for non-linear effects at high energies and, δ is a constant offset accounting for PMT dark noise and other sporadic sources of pulses. E is the total energy deposited in the LAr in the form of excitation and ionization in units keV. Here $LY \cdot E$ then gives the mean number of PE created (NPE). The mean number is then Poisson smeared to give the distribution of emitted PE (nPE). The last component of the response function is the resolution in measuring nPE. The resolution is included in a Gaussian term, where σ is defined as:

$$\sigma^2 = \sigma^2_{linear} nPE + \sigma^2_{const} nPE^2. \tag{9.2}$$

Here σ_{linear} accounts for things like the PMT SPE charge distributions, and σ_{const} accounts for e.g. the position dependence in the energy response. A fit is performed to ^{39}Ar data using the theoretical β-decay energy distribution from [116] was performed to evaluate the parameters in this response function. The fit considers a charge range between 300 and 4000 QPE. The data errors were determined from the number of events in each bin adjusting for the number of pre-scaled events via:

$$\sigma_{data} = \sqrt{n_1 + \xi^2 n_2}, \tag{9.3}$$

where n_1 is the number of events from non-pre-scaled triggers, and n_2 is the

number of events from the pre-scaled trigger. The pre-scale factor is $\xi = 100$ for this data. No penalty terms were added for any model variations in the theoretical ^{39}Ar spectrum. For the energy response, the data from the Multi-Site cut is used. It was verified that fit results do not vary by large amounts after each cut up to this point in the analysis flow. Beyond this, the energy dependence in the cut acceptances strongly influence the results. Table 9.1 gives the best fit parameters for the energy response. Figure 9.1 shows the fit response function compared to data. The δ term is in agreement with $\sim$500 Hz per PMT dark rate. An agreement to within $\sim$1% of the final fit function and data as seen in the ratio plot in Figure 9.1.

With the overall good agreement and low error on the energy response, the dominant systematic error in the energy spectrum for the WIMP analysis comes from the uncertainty in the quenching factor. The quenching factor is applied to the LY via:

$$LY' = LY \times \gamma(E), \tag{9.4}$$

where $\gamma(E)$ is the quenching factor between electromagnetic and nuclear events. In this analysis, the results of [78] are used. A constant 5% uncertainty is assigned to the data, as discussed in Section 9.5.

9.2 WIMP Region of Interest

As previously mentioned, WIMPs will recoil from a single Ar nucleus. The best method to mimic WIMP events is with a neutrons source. When neutrons interact with Ar, they create the same Ar nuclear recoils; unfortunately,

Parameter	Value	Fit Error
α (1/keVee)	7.146	0.004
η (1/keVee^2)	-79x10^{-5}	1x10^{-5}
δ	1.170	0.008
σ_{linear}	0.170	0.003
σ_{const}	0.0262	0.0004
χ^2/NDF	1275/933	

Table 9.1: Results of the energy response fit to the data using the theoretical spectrum in [116].

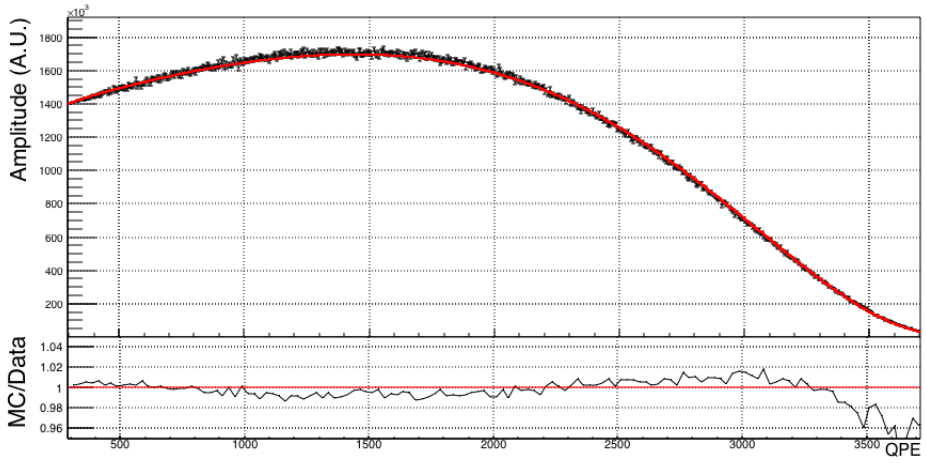

Figure 9.1: Comparison between ^{39}Ar data (black) and the expected distribution from the theoretical electron spectrum from Ref. [116] convoluted with the energy distribution (red).

neutrons most often do not just interact once within the detector; scattering multiple times and spreading out their energy. Furthermore, neutrons also scatter in-elastically with the Ar, creating gamma rays that decreases the fPrompt of the signal. All of this distorts the signal of single scatter events and makes it challenging to relate the neutron signal back to that expected for WIMPs. The RAT simulation is used to simulate the interactions of the

neutrons and the nuclear recoil response. The RAT simulation's response is tuned to match what we see in the neutron data [117] and is then used to simulate single ^{40}Ar recoils for the WIMP Signal.

Figure 9.2 (top) shows the full fPrompt/QPE distribution for neutron data with the 90% WIMP acceptance contour lines overlaid. Figure 9.2 (bottom) shows the projection of the neutron data above 110 QPE compared to the MC distribution of single ^{40}Ar scatters. The ^{40}Ar distribution was normalized to match the integral of the neutron distribution above $\text{fPrompt}_{60} = 0.6$. The figure shows reasonable agreement between the two distributions, with deviations at low fPrompt as expected from inelastic neutron scatters.

9.3 Pulse Shape Discrimination

The final cut applied in this analysis is the PSD used to remove unwanted Ar scintillation events from the data and leaving only the nuclear recoil type events. There are two parts to this cut. On the upper end of the cut is the 90% Ar40 recoil acceptance contour line (flat energy distribution). On the lower fPrompt edge is the maximum fPrompt value between the lower 90% ^{40}Ar recoil acceptance contour line and the ^{39}Ar exclusion limit.

The ^{39}Ar exclusion limit is set by taking 1-PE slices and fitting the tail of the ^{39}Ar fPrompt distribution to an exponential. The distributions are fit starting at 2×RMS past the distribution mean. The 2σ error is added to the parameters and then integrated to give 1 event in the final exposure. This line provides a 2σ upper confidence limit that 1 or fewer ^{39}Ar events are in the WIMP ROI. An example fit of the fPrompt distribution tail is

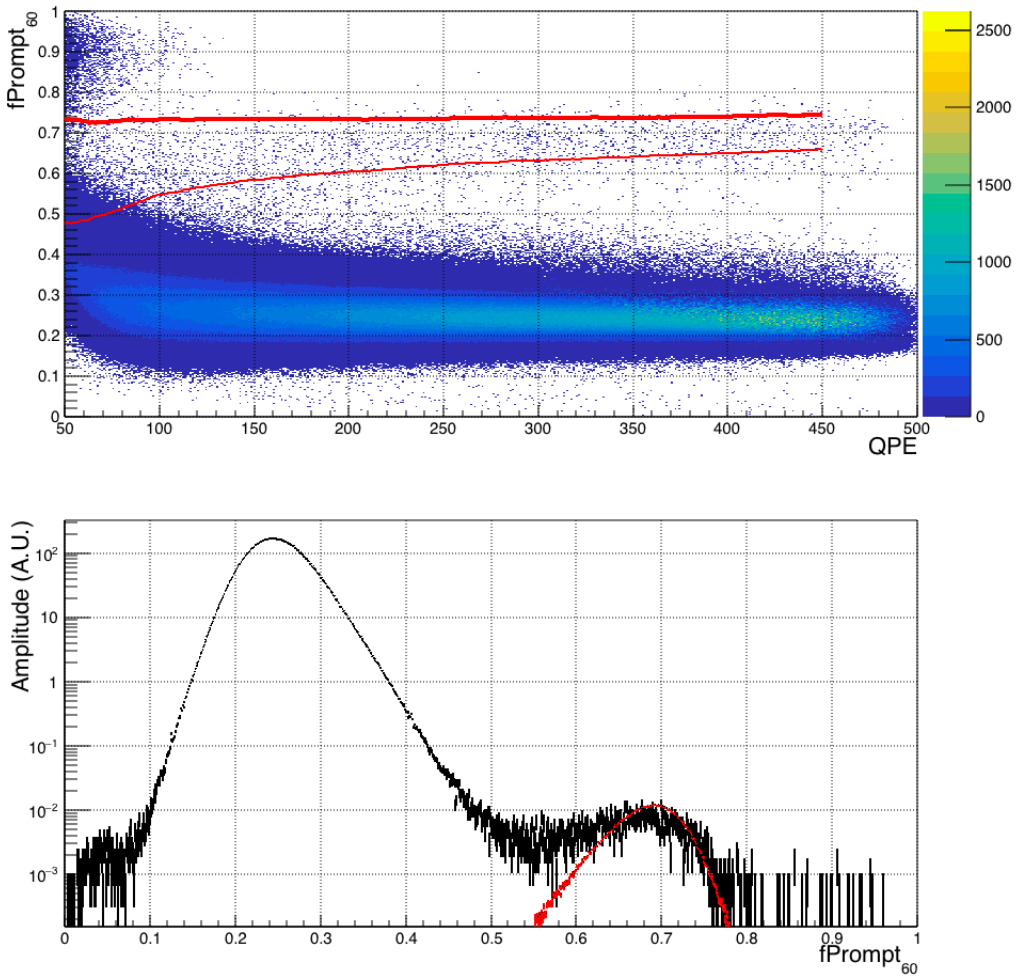

Figure 9.2: The comparison of the MC ^{40}Ar nuclear recoil with neutron data from AmBe calibration. (Top) The full fPrompt60/QPE distribution for neutron data from AmBe calibration. Outlined in yellow is the MC 90% contour lines for single Ar40 recoils. (Bottom) Comparison of the projected neutron fPrompt distribution with the MC ^{40}Ar single recoil distribution shown red.

shown in Figure 9.3 for the 120 QPE slice. The prompt window used for this analysis was chosen because it optimized the significance of the gap between the peaks of the electromagnetic and nuclear recoil fPrompt distributions. Figure 9.4 shows the acceptance of the WIMP signal region for the fPrompt$_{60}$ and fPrompt$_{150}$ PSD variables. This figure shows a clear preference to the

60 ns prompt window, giving significantly more acceptance to WIMPs for the same ^{39}Ar exclusion criteria.

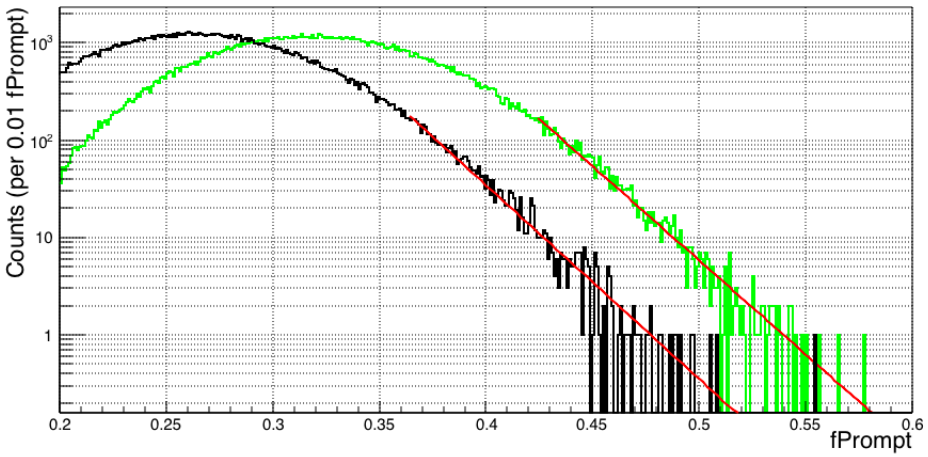

Figure 9.3: Sample fits of the fPrompt distributions at 120 QPE for setting the PSD cut. Shown is the fPrompt_{60} distribution (black) and the fPrompt_{150} distribution (green). Fit functions of the high fPrompt tails for both distributions are shown (red). The fits are performed starting at 2×RMS from the mean.

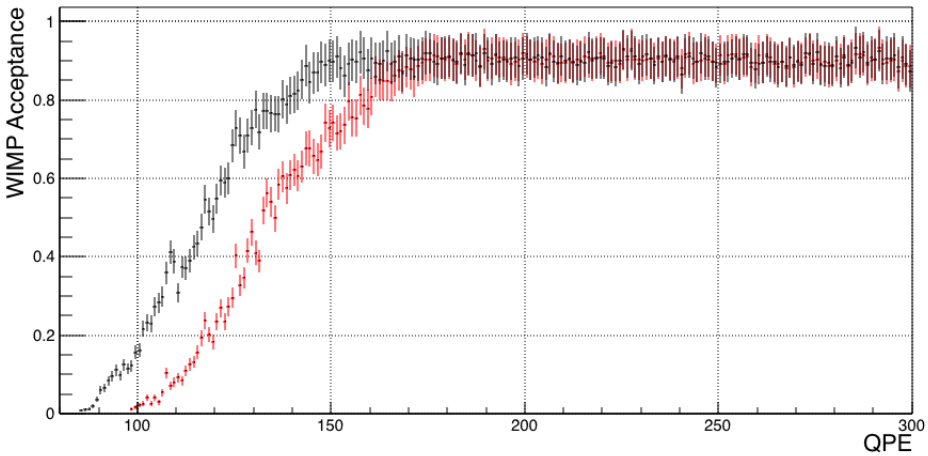

Figure 9.4: The acceptance of WIMPs from the PSD Cut using the fPrompt_{150} PSD cut (red) and the fPrompt_{60} PSD cut (black). The errors are purely statistical, largely due to a lack of statistics in the simulated ^{40}Ar distributions.

Due to a large number of background events, including the upper WIMP ROI energies is not advantageous. For this analysis The upper energy limit in the analysis is set to cut 50% of the measurable signal for a given WIMP mass. Figure 9.5 shows the endpoint QPE for the 50% signal cut for a given WIMP mass.

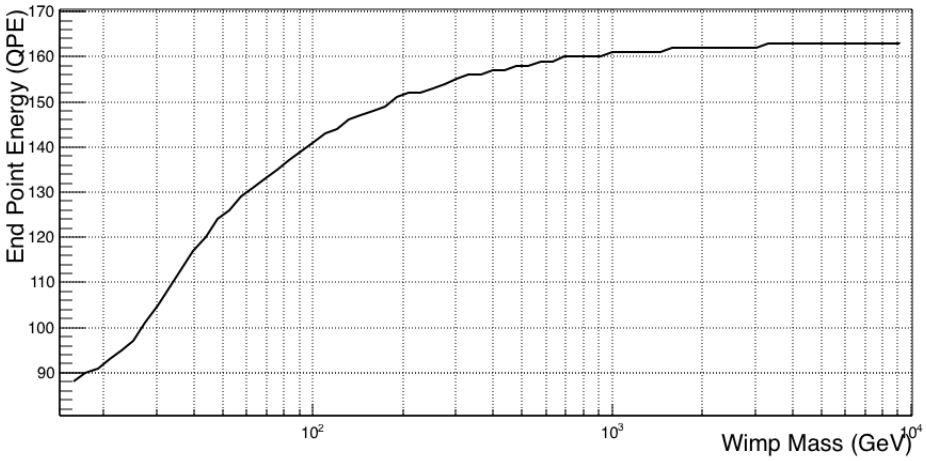

Figure 9.5: The endpoint energy used for the WIMP search for the different WIMP masses such that 50% of the measurable signal is cut away.

9.4 Cut Acceptance

At every stage in the cut flow, events are removed creating a data set with improved signal/background. While an effort is made to only remove the events that are not caused by WIMPs, inadvertently some of the WIMP ROI is sacrificed to exclude unwanted background events. The loss in ability to detect WIMPs is split into two factors that enter the WIMP limit. The first is exposure. Exposure, defined as the target mass multiplied by the total amount of time that the detector is live and can detect a WIMP recoil. The

exposure is reduced by any cut that blindly cuts away a window of the runtime. Exposure cuts include the Data Quality, CalCut, DeltaT, Multi-Event, Muon Coincidence and Gamma coincidence.

If a cut evaluates at the properties of the event before it decides to remove or keep the event, then the cut will affect the signal acceptance. The acceptance of a cut is computed in one of two ways. If the cut does not require pulse shape or time information to be applied then ^{39}Ar β-decays can be used to best estimate the cut acceptance for WIMPs, since the only difference between the WIMP signal and ^{39}Ar is the time distribution of the light. If the cut depends on the time structure of the signal, then ^{40}Ar recoil simulated data is used to evaluate the cut acceptance. The Multi-Event cut has both a reduction in exposure and a decrease in acceptance to account for the fact that we do not search for WIMP events on top of other events. In addition, a number of false pile-up triggers are expected for WIMPs. Table 9.2 shows the cut acceptance at 120 QPE and the total live time after every stage in the analysis. Due to the lack of precise fiducial volume definition, the reduction of this mass due to fiducialization cuts will be reported as a loss in signal acceptance rather than relating this reduction to an exact fiducialized mass. Figure 9.6 shows the energy-dependent acceptance after significant reductions in the WIMP signal acceptance due to the cuts.

9.5 WIMP Exclusion

Processing the data through the cut flow, a total of 8 events remain within the ROI for a 100 GeV WIMP. Figure 9.7 shows the events that remain after all the

Cut	Acceptance at 120 QPE	Exposure (tonne-years)	Method	Events (see capt.)
Data Quality	-	2.20 ± 0.07	-	-
Cal Cut	-	-	-	-
Delta T	-	-	-	-
Multi-Event	0.99 ± 0.08	2.07 ± 0.07	MC	11945751
Early Pulses	1.000 ± 0.003	-	^{39}Ar	11945751
t_0	1.000 ± 0.003	-	^{39}Ar	11945551
FMaxPe	0.954 ± 0.003	-	^{39}Ar	102135
Multi-Site	0.96 ± 0.03	-	^{40}ArMC	89899
Top Ring Frac	0.679 ± 0.002	-	^{39}Ar	404
Position	0.742 ± 0.002	-	^{39}Ar	122
Muon Coinc	-	2.07 ± 0.07	-	117
Gamma Coinc	-	2.05 ± 0.07	-	117
LRatio	0.756 ± 0.003	-	^{39}Ar	63
Neck Charge	0.998 ± 0.004	-	^{39}Ar	57
Late AP Frac	1.00 ± 0.05	-	^{40}ArMC	57
PSD (60 ns)	0.55 ± 0.04	-	^{40}ArMC	46
Total	0.19 ± 0.02	2.05 ± 0.07	-	46

Table 9.2: Cut Acceptance and exposure through the different cuts applied to data. The total acceptance of the cut sequence is 19±2% at 120 QPE. The method used to determine the cut acceptance, being either ^{39}Ar events in Data where the cut does not have an fPrompt dependance, or ^{40}Ar events from a RAT simulation. The number of events quoted in the events column is the number of events in the full data set that persist after additionally applying the lower fPrompt PSD cut.

cuts are applied in the ROI region. The expected WIMP rates are computed using the fit energy spectrum and quenching factor. The 90% C.L. exclusion curve is calculated accounting for the uncertainty in the signal acceptance and energy response using the method in [118]. The uncertainty in the signal acceptance is the weighted average defined by

$$< \sigma_{acceptance} >= \int \frac{\sigma_{acceptance}(QPE)S(QPE)}{\int S(QPE)}, \tag{9.5}$$

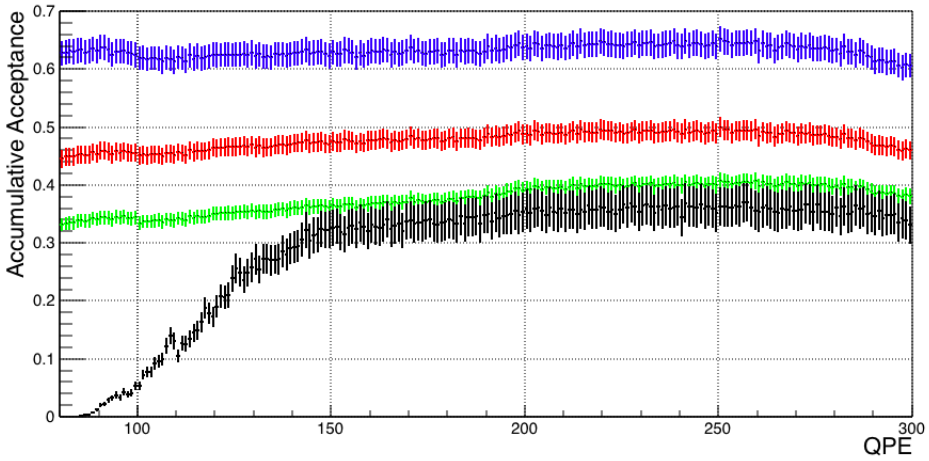

Figure 9.6: The accumulative cut acceptance after major cuts in the analysis. The acceptance after (Blue) Top Ring Frac, (Red) Position, (Green) LRatio and (Black) PSD is shown. Errors in the acceptance are purely statistical, dominated by the limited statistics of ^{40}Ar recoils.

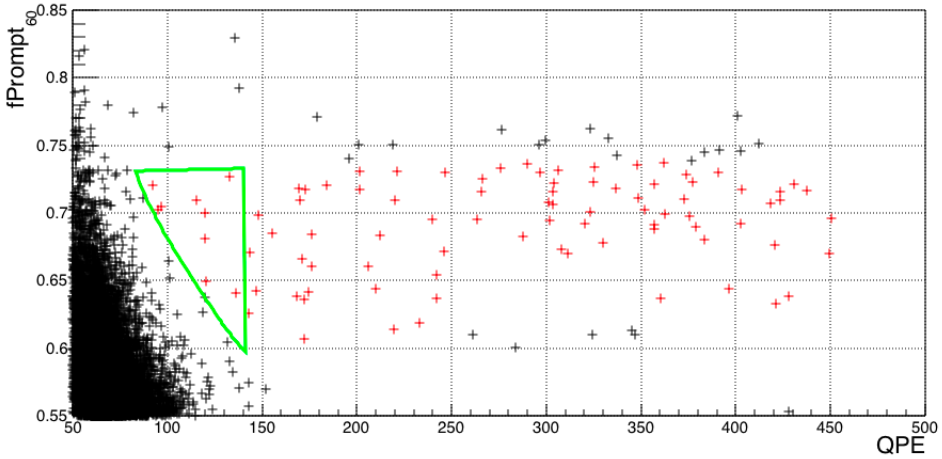

Figure 9.7: Events that survive the cuts up to the LateAPFrac cut are shown (black). Also shown are the events that pass the PSD cut (red). The ROI region for a 100 GeV WIMP is outlined (green).

where $S(QPE)$ is the expected signal rate, and $\sigma_{acceptance}(QPE)$ is the uncertainty in the acceptance. The integral runs over the ROI for a given WIMP mass. The uncertainty in the acceptance is then added in quadrature with

the uncertainty in the signal rate due to the energy response function. The dominant uncertainty in the energy response function is the uncertainty in the quenching factor. To include this, an 5% uncertainty (based on the error in the ARIS result shown in Figure 2.3) is assigned to the quenching factor, and the expected signal is computed for the $\pm 1\sigma$ quenching limits. The uncertainty is taken as:

$$\sigma_{energy} = \frac{|S_{+\sigma} - S_{-\sigma}|}{2} \tag{9.6}$$

This gives an exclusion for the WIMP-nucleon cross-section of $\sigma_0 = 9.24$ x 10^{-45} cm^2 for a 100 GeV WIMP (90% C.L.). Figure 9.8 shows the full result in comparison to the first 4-day DEAP result along with several other curves from competing experiments. As can be seen from the result, only a marginal improvement is made over DEAP's 4-day result of 1.2 x 10^{-44} cm^2 despite having $\sim$ 75 times the exposure. Further exclusion of the WIMP-nucleon parameter space is stalled due to a large background from a currently unknown origin that is dominating the ROI. It is currently the focus of the DEAP collaboration to characterize and understand these events.

9.6 Surviving Events

There are currently 46 events that fill the WIMP ROI between 80 and 300 QPE. These events pass all the applied cuts that are aimed at removing known background sources. One of the most probable source of events are surface alphas that only partially deposit their energy within the LAr; the rest being deposited within the TPB or acrylic. These 'degraded' alpha events would

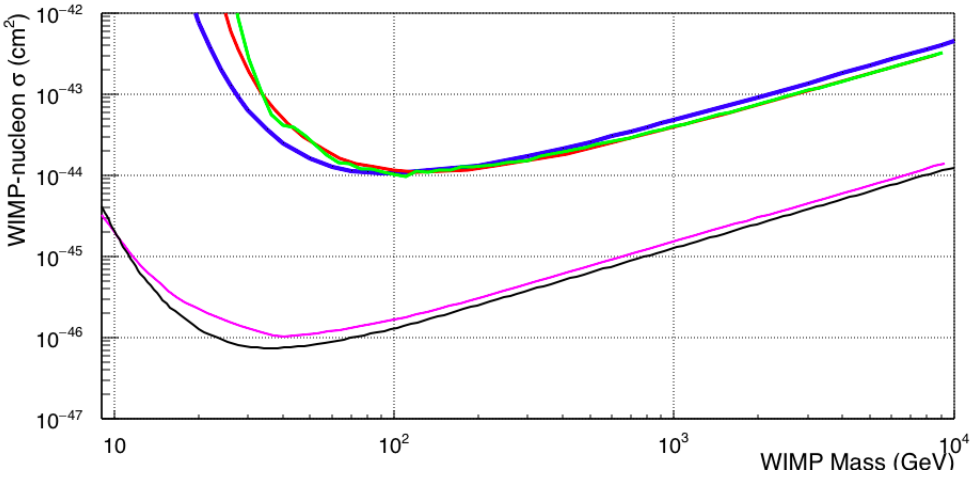

Figure 9.8: The (90% C.L.) confidence limit for the exclusion of WIMPs for this result (), DEAP-3600 first result (blue) [108], DarkSide(2018) (red) [119], LUX(2017) (purple) [120] and XENON1T(2017) (black) [60].

originate on the edges of the detector and we would expect the leakage of these events to be from high radius events. Figure 9.9 shows the r^3 distribution for the ROI events as well as the cylindrical coordinates of the vertex position given by the position fitter. As can be seen, the events are dominated by low radii positions and cutting harder on the event radius would not remove a significant fraction of these events while reducing the potential WIMP signal region.

Another possibility is that the WIMP ROI events are due to a source of neutrons that is leaking into the detector. A neutron candidate is inconsistent with the fraction of events that are removed by the gamma coincidence cut. No events are removed by the gamma coincidence cut in the physics data. In contrast, 31 ± 1 % of neutron events in a neutron source run are removed by tagging the following gamma ray. The absence of gamma tagged events gives an upper 90% C.L. of 8 events in the energy band out to 500 QPE being from

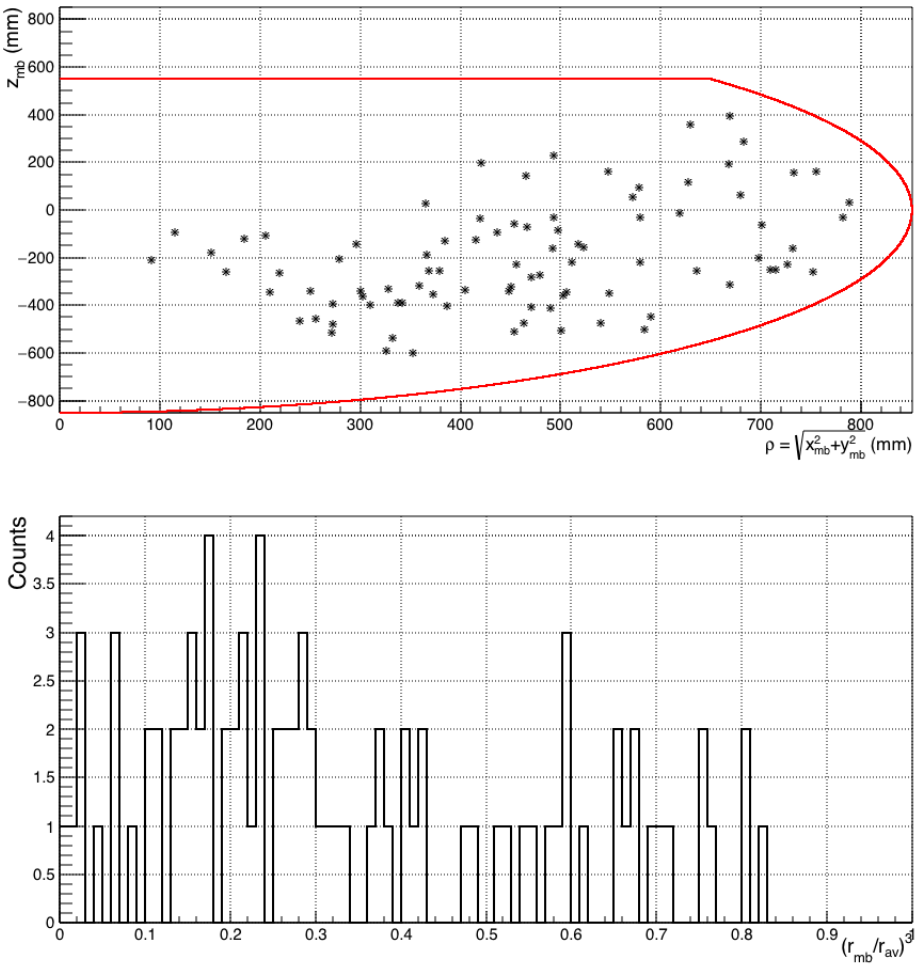

Figure 9.9: Position distributions of the ROI events that survive all cuts. (Top) Position of the events in cylindrical coordinates. The LAr boundary is outlined in red. (Bottom) The normalized r^3 distribution of the events.

neutrons.

These ROI events have been examined in the full list of variables used to remove unwanted events. In all distributions, the ROI events appear to be consistent with high fPrompt events in the ROI. These events are not expected to be WIMPs due to the large disagreement with the LUX and XENON1T experiments.

9.7 Conclusion

Since the first release of the 4-day result, the DEAP collaboration has focused efforts on understanding and discriminating a source of background events. While significant progress has been made in improving our understanding of the detector, the exact origin of these events continues to be a mystery. In the absence of a new cut that can discriminate this background source, DEAP-3600 has ultimately reached its WIMP sensitivity. However, as the calibration of the detector improves, our ability to interpret the data advances. With a first round of optical model tuning complete, we are brought one step closer to fully reproducing the characteristics of the detector. The next series of optical model tuning focused on the PMT timing will likely provide the ability to distinguish the unknown background based on the time-of-flight event position fitting. While the limit reported in this thesis is not world-leading, it is the author's opinion that DEAP may produce a competitive limit on the WIMP-nucleon spin independent cross-section in the near future.

Bibliography

[1] Bradley W. Carroll and Dale A. Ostlie. *An Introduction to Modern Astrophysics*. 2nd (international) edition, 2007.

[2] F. Zwicky. Die Rotverschiebung von extragalaktischen Nebeln. *Helv. Phys. Acta*, 6:110–127, 1933. [Gen. Rel. Grav.41,207(2009)].

[3] Vera C. Rubin and W. Kent Ford, Jr. Rotation of the Andromeda Nebula from a Spectroscopic Survey of Emission Regions. *Astrophys. J.*, 159:379–403, 1970.

[4] T. Albada et al. Distribution of dark matter in spiral galaxy ngc 3198. *Astro. Phys. Jour.*, 295:305, 1985.

[5] Edvige Corbelli and Paolo Salucci. The Extended Rotation Curve and the Dark Matter Halo of M33. *Mon. Not. Roy. Astron. Soc.*, 311:441–447, 2000.

[6] G. Bertone and D. Hooper. A history of dark matter. *FERMILAB-PUB-16-157-A*, 2016.

[7] E. Hubble. A Relation between Distance and Radial Velocity among Extra-Galactic Nebulae. *Proceedings of the National Academy of Science*, 15:168–173, March 1929.

[8] Cormac O'Raifeartaigh and Simon Mitton. Einstein's "biggest blunder" - interrogating the legend. 2018.

[9] Wendy L. Freedman and Barry F. Madore. The Hubble Constant. *Ann. Rev. Astron. Astrophys.*, 48:673–710, 2010.

[10] R. A. Alpher, H. Bethe, and G. Gamow. The origin of chemical elements. *Phys. Rev.*, 73:803–804, 1948.

[11] C. Patrignani et al. Review of Particle Physics. *Chin. Phys.*, C40(10):100001, 2016.

[12] R. WILSON. The cosmic microwave background radiation. Nobel Lecture, 1978.

[13] P. A. R. Ade et al. Planck 2015 results. XIII. Cosmological parameters. *Astron. Astrophys.*, 594:A13, 2016.

[14] P. A. R. Ade et al. Planck 2013 results. XVI. Cosmological parameters. *Astron. Astrophys.*, 571:A16, 2014.

[15] Cmb photo from planck. http://astrog80.astro.cf.ac.uk/Planck/Allsky-imgs/PlanckFig_map_columbi1_IDL_HighDR_colbar_1000px_CMB_moll.png. Accessed: 2018-09-09.

[16] Scott W. Randall, Maxim Markevitch, Douglas Clowe, Anthony H. Gonzalez, and Marusa Bradac. Constraints on the Self-Interaction Cross-Section of Dark Matter from Numerical Simulations of the Merging Galaxy Cluster 1E 0657-56. *Astrophys. J.*, 679:1173–1180, 2008.

[17] Julio F. Navarro, Carlos S. Frenk, and Simon D. M. White. The Structure of cold dark matter halos. *Astrophys. J.*, 462:563–575, 1996.

[18] Gerard Jungman, Marc Kamionkowski, and Kim Griest. Supersymmetric dark matter. *Phys. Rept.*, 267:195–373, 1996.

[19] Bradley J. Kavanagh and Anne M. Green. Improved determination of the WIMP mass from direct detection data. *Phys. Rev.*, D86:065027, 2012.

[20] Anne M. Green. Astrophysical uncertainties on direct detection experiments. *Mod. Phys. Lett.*, A27:1230004, 2012.

[21] Benoit Famaey and Stacy McGaugh. Modified Newtonian Dynamics (MOND): Observational Phenomenology and Relativistic Extensions. *Living Rev. Rel.*, 15:10, 2012.

[22] Riccardo Scarpa. Modified newtonian dynamics, an introductory review. *AIP Conf. Proc.*, 822:253–265, 2006. [,253(2006)].

[23] M. Markevitch, A. H. Gonzalez, L. David, A. Vikhlinin, S. Murray, W. Forman, C. Jones, and W. Tucker. A Textbook example of a bow shock in the merging galaxy cluster 1E0657-56. *Astrophys. J.*, 567:L27, 2002.

[24] D. Clowe et al. A direct empirical proof of the existence of dark matter. *The Astrophysical Journal Letters*, 648(2):L109, 2006.

[25] P. Tisserand et al. Limits on the Macho Content of the Galactic Halo from the EROS-2 Survey of the Magellanic Clouds. *Astron. Astrophys.*, 469:387–404, 2007.

[26] George R. Blumenthal, S. M. Faber, Joel R. Primack, and Martin J. Rees. Formation of Galaxies and Large Scale Structure with Cold Dark Matter. *Nature*, 311:517–525, 1984. [,96(1984)].

[27] J. Maneira. Combined Analysis of all Three Phases of Solar Neutrino Data from the Sudbury Neutrino Observatory. In *Proceedings, 13th ICATPP Conference on Astroparticle, Particle, Space Physics and Detectors for Physics Applications (ICATPP 2011): Como, Italy, October 3-7, 2011*, pages 360–366, 2012.

[28] Marco Drewes. The Phenomenology of Right Handed Neutrinos. *Int. J. Mod. Phys.*, E22:1330019, 2013.

[29] J. M. Conrad and M. H. Shaevitz. Sterile Neutrinos: An Introduction to Experiments. *Adv. Ser. Direct. High Energy Phys.*, 28:391–442, 2018.

[30] Marco Drewes and Jin U Kang. Sterile neutrino Dark Matter production from scalar decay in a thermal bath. *JHEP*, 05:051, 2016.

[31] Michael S. Turner. Windows on the Axion. *Phys. Rept.*, 197:67–97, 1990.

[32] David J. E. Marsh. Axions and ALPs: a very short introduction. In *Proceedings, 13th Patras Workshop on Axions, WIMPs and WISPs, (PA-*

TRAS 2017): Thessaloniki, Greece, 15 May 2017 - 19, 2017, pages 59–74, 2018.

[33] Denis Wouters and Pierre Brun. Constraints on axion-like particles from γ-ray astronomy with H.E.S.S. In *Proceedings, 48th Rencontres de Moriond on Very High Energy Phenomena in the Universe: La Thuile, Italy, March 9-16, 2013*, pages 145–148, 2013.

[34] Ron Mayle, James R. Wilson, John R. Ellis, Keith A. Olive, David N. Schramm, and Gary Steigman. Constraints on Axions from SN 1987a. *Phys. Lett.*, B203:188–196, 1988.

[35] N. Du et al. A Search for Invisible Axion Dark Matter with the Axion Dark Matter Experiment. *Phys. Rev. Lett.*, 120(15):151301, 2018.

[36] Edward W. Kolb and Michael S. Turner, editors. *THE EARLY UNIVERSE. REPRINTS*. 1988.

[37] Annika H. G. Peter. Dark Matter: A Brief Review. 2012.

[38] STEPHEN P. MARTIN. *A SUPERSYMMETRY PRIMER*, pages 1–98. 2011.

[39] Morad Aaboud et al. Measurement of the Higgs boson mass in the $H \to ZZ^* \to 4\ell$ and $H \to \gamma\gamma$ channels with $\sqrt{s} = 13$ TeV pp collisions using the ATLAS detector. *Phys. Lett.*, B784:345–366, 2018.

[40] S. Martin. A supersymmetry primer. *arXiv:hep-ph/9709356*, 1997.

[41] Diptimoy Ghosh, Monoranjan Guchait, Sreerup Raychaudhuri, and Dipan Sengupta. How Constrained is the cMSSM? *Phys. Rev.*, D86:055007, 2012.

[42] R. Bernabei et al. First results from DAMA/LIBRA and the combined results with DAMA/NaI. *Eur. Phys. J.*, C56:333–355, 2008.

[43] C. E. Aalseth et al. Search for an Annual Modulation in a P-type Point Contact Germanium Dark Matter Detector. *Phys. Rev. Lett.*, 107:141301, 2011.

[44] R. Agnese et al. Silicon Detector Dark Matter Results from the Final Exposure of CDMS II. *Phys. Rev. Lett.*, 111(25):251301, 2013.

[45] K. A. Olive et al. Review of Particle Physics. *Chin. Phys.*, C38:090001, 2014.

[46] Jan Conrad. Indirect Detection of WIMP Dark Matter: a compact review. In *Interplay between Particle and Astroparticle physics (IPA2014) London, United Kingdom, August 18-22, 2014*, 2014.

[47] M. G. Aartsen et al. Search for dark matter annihilations in the Sun with the 79-string IceCube detector. *Phys. Rev. Lett.*, 110(13):131302, 2013.

[48] S. Archambault et al. Constraints on Low-Mass WIMP Interactions on ^{19}F from PICASSO. *Phys. Lett.*, B711:153–161, 2012.

[49] E. Behnke et al. Improved Limits on Spin-Dependent WIMP-Proton Interactions from a Two Liter CF_3I Bubble Chamber. *Phys. Rev. Lett.*, 106:021303, 2011.

[50] C. Amole et al. Dark Matter Search Results from the PICO-60 C_3F_8 Bubble Chamber. *Phys. Rev. Lett.*, 118(25):251301, 2017.

[51] C. Amole et al. Dark matter search results from the PICO-60 CF_3I bubble chamber. *Phys. Rev.*, D93(5):052014, 2016.

[52] C. Amole et al. Improved dark matter search results from PICO-2L Run 2. *Phys. Rev.*, D93(6):061101, 2016.

[53] E. Behnke et al. Final Results of the PICASSO Dark Matter Search Experiment. *Astropart. Phys.*, 90:85–92, 2017.

[54] M. Felizardo et al. The SIMPLE Phase II Dark Matter Search. *Phys. Rev.*, D89(7):072013, 2014.

[55] Changbo Fu et al. Spin-Dependent Weakly-Interacting-Massive-Particle–Nucleon Cross Section Limits from First Data of PandaX-II Experiment. *Phys. Rev. Lett.*, 118(7):071301, 2017. [Erratum: Phys. Rev. Lett.120,no.4,049902(2018)].

[56] M. G. Aartsen et al. Search for annihilating dark matter in the Sun with 3 years of IceCube data. *Eur. Phys. J.*, C77(3):146, 2017.

[57] T. Tanaka et al. An Indirect Search for WIMPs in the Sun using 3109.6 days of upward-going muons in Super-Kamiokande. *Astrophys. J.*, 742:78, 2011.

[58] K. Choi et al. Search for neutrinos from annihilation of captured low-mass dark matter particles in the Sun by Super-Kamiokande. *Phys. Rev. Lett.*, 114(14):141301, 2015.

[59] Leszek Roszkowski, Roberto Ruiz de Austri, and Roberto Trotta. Implications for the Constrained MSSM from a new prediction for $b \to s\gamma$. *JHEP*, 07:075, 2007.

[60] E. Aprile et al. First Dark Matter Search Results from the XENON1T Experiment. *Phys. Rev. Lett.*, 119(18):181301, 2017.

[61] D. S. Akerib et al. Results from a search for dark matter in the complete LUX exposure. *Phys. Rev. Lett.*, 118(2):021303, 2017.

[62] Andi Tan et al. Dark Matter Results from First 98.7 Days of Data from the PandaX-II Experiment. *Phys. Rev. Lett.*, 117(12):121303, 2016.

[63] E. Aprile et al. XENON100 Dark Matter Results from a Combination of 477 Live Days. *Phys. Rev.*, D94(12):122001, 2016.

[64] J. D. Lewin and P. F. Smith. Review of mathematics, numerical factors, and corrections for dark matter experiments based on elastic nuclear recoil. *Astropart. Phys.*, 6:87–112, 1996.

[65] Richard H. Helm. Inelastic and Elastic Scattering of 187-Mev Electrons from Selected Even-Even Nuclei. *Phys. Rev.*, 104:1466–1475, 1956.

[66] Tadayoshi Doke, Akira Hitachi, Jun Kikuchi, Kimiaki Masuda, Hiroyuki Okada, and Eido Shibamura. Absolute Scintillation Yields in Liquid

Argon and Xenon for Various Particles. *Jap. J. Appl. Phys.*, 41:1538–1545, 2002.

[67] A. Wright. Optical attenuation in liquid argon. Internal Collaboration Analysis Note.

[68] M. Hishida S. Kubota and J. Raun. Evidence for a triplet state of the self-trapped exciton states in liquid argon, krypton and xenon. *Journal of Physics C: Solid State Physics*, 11(12):2645, 1978.

[69] W. H. Lippincott, K. J. Coakley, D. Gastler, A. Hime, E. Kearns, D. N. McKinsey, J.A. Nikkel, and L. C. Stonehill. Scintillation time dependence and pulse shape discrimination in liquid argon. *Phys. Rev.*, C78:035801, 2008. [Erratum: Phys. Rev.C81,039901(2010)].

[70] T. Heindl, T. Dandl, A. Fedenev, M. Hofmann, R. Krücken, L. Oberauer, W. Potzel, J. Wieser, and A. Ulrich. Table-top setup for investigating the scintillation properties of liquid argon. *JINST*, 6:P02011, 2011.

[71] W. Brown C. Reimann and R. Johnson. Electrically stimulated sputtering and luminesence from solid argon. *Phys Rev B*, 37:1455, 1988.

[72] T. Heindl, T. Dandl, M. Hofmann, R. Krucken, L. Oberauer, W. Potzel, J. Wieser, and A. Ulrich. The scintillation of liquid argon. *EPL*, 91(6):62002, 2010.

[73] D. Grosjean et al. Absolute luminescence efficiency of ion-bombarded solid argon. *Phys Rev B*, 56:6975, 1997.

[74] S. Kubota, A. Nakamoto, T. Takahashi, T. Hamada, E. Shibamura, M. Miyajima, K. Masuda, and T. Doke. Recombination luminescence in liquid argon and in liquid xenon. *Phys. Rev.*, B17(6):2762–2765, 1978.

[75] M. Scharff J. Lindhard and H. E. Schiøtt. Range concepts and heavy ion ranges. *Mat. Fys. Medd. Dan. Vid. Selsk.*, 33(14), 1963.

[76] T. Doke A. Hitachi and A. Mozumder. Luminesence quenching in liquid argon under charged particle impact: Relative scintilation yield at different linear transfers. *Phys Rev B*, 46:11463, 1992.

[77] Ö Şahin, İ Tapan, E. N. Özmutlu, and R. Veenhof. Penning transfer in argon-based gas mixtures. *JINST*, 5(05):P05002, 2010.

[78] P. Agnes et al. Measurement of the liquid argon energy response to nuclear and electronic recoils. *Phys. Rev.*, D97(11):112005, 2018.

[79] Akira Hitachi, Tan Takahashi, Nobutaka Funayama, Kimiaki Masuda, Jun Kikuchi, and Tadayoshi Doke. Effect of ionization density on the time dependence of luminescence from liquid argon and xenon. *Phys. Rev.*, B27:5279–5285, 1983.

[80] P. A. Amaudruz et al. Design and Construction of the DEAP-3600 Dark Matter Detector. *Submitted to: Astropart. Phys.*, 2017.

[81] Corina Nantais. *Radiopurity measurement of acrylic for the DEAP-3600 dark matter experiment.* PhD thesis, Queen's University, 2014.

[82] Low background counting at snolab. SNOLAB LRC Presentation by Ian Lawson, https://www.snolab.ca/users/services/gamma-

assay/Talks_Presentations/lrt_2010_Ian_Lawson.pdf. Accessed: 2018-09-09.

[83] Chris Jillings. Control of contamination of radon-daughters in the DEAP-3600 acrylic vessel. *AIP Conf. Proc.*, 1549:86–89, 2013.

[84] P. A. Amaudruz et al. Design and Construction of the DEAP-3600 Dark Matter Detector. *Submitted to: Astropart. Phys.*, 2017.

[85] B. Broerman et al. Application of the TPB Wavelength Shifter to the DEAP-3600 Spherical Acrylic Vessel Inner Surface. *JINST*, 12(04):P04017, 2017.

[86] V. M. Gehman, S. R. Seibert, K. Rielage, A. Hime, Y. Sun, D. M. Mei, J. Maassen, and D. Moore. Fluorescence Efficiency and Visible Re-emission Spectrum of Tetraphenyl Butadiene Films at Extreme Ultraviolet Wavelengths. *Nucl. Instrum. Meth.*, A654:116–121, 2011.

[87] Light guide acrylic attenuation measurement. Internal Collaboration Measurement.

[88] Hamamatsu large photocathode area photomultiplier tubes datasheet. https://www.hamamatsu.com/resources/pdf/etd/LARGE_AREA_PMT_TPMH1286E.pdf. Accessed: 2018-09-09.

[89] A.G. Wright, editor. *The Photomultiplier Handbook*. 2017.

[90] Hamamatsu pmt handbook. https://www.hamamatsu.com/resources/pdf/etd/PMT_handbook_v3aE.pdf. Accessed: 2018-09-09.

[91] Alistair Butcher. *Search For Dark Matter With DEAP-3600.* PhD thesis, Royal Holloway, University of London, 2017.

[92] P. Benetti et al. Measurement of the specific activity of 39ar in natural argon. *NIM A*, 574:83 – 88, 2007.

[93] D. Acosta-Kane et al. Discovery of underground argon with low level of radioactive 39Ar and possible applications to WIMP dark matter detectors. *Nucl. Instrum. Meth.*, A587:46–51, 2008. [J. Phys. Conf. Ser.120,042015(2008)].

[94] J.D. Jackson. *Classical Electrodynamics*. Wiley, 2012.

[95] Deapstr2017x008_v6. Collaboration Technical Report, Eric Vazquez-Jauregui. Accessed: 2018-09-09.

[96] Braidwood neutrino experiment. Rat documentation. http://rat.readthedocs.io/en/latest/index.html. Accessed: 2018-09-30.

[97] S. Agostinelli et al. Geant4—a simulation toolkit. *Nuc. Instrum. Meth. A*, 506(3):250 – 303, 2003.

[98] R. Brun and F. Rademakers. Root - an object oriented data analysis framework. *Nucl. Inst. and Meth. in Phys. Res. A*, 389:81–86, 1997.

[99] Root user guide. https://root.cern.ch/root/htmldoc/guides/users-guide/ROOTUsersGuideA4.pdf. Accessed: 2018-09-09.

[100] P. Agnes et al. First Results from the DarkSide-50 Dark Matter Experiment at Laboratori Nazionali del Gran Sasso. *Phys. Lett.*, B743:456–466, 2015.

[101] J.D. Stachiw and Marine Technology Society. *Handbook of acrylics for submersibles, hyperbaric chambers, and aquaria*. Best Pub. Co., 2003.

[102] Qudo-dec-d-7202-03_rev_0. DEAP Technical Drawing, Koby Dering. Accessed: 2018-09-09.

[103] C. Hirschi J. Oertel, B. Bourque and F. Lopez. La-ur-07-8170. Los Alomos Internal Document.

[104] D.W. Fowler D.R. Paul and J.T. Houston. Polymerization of methyl methacrylate by catalyzed peroxide decomposition without applied heat. *J.APP. POLY. SCI.*, 17:2771–2782, 1973.

[105] MIDAS midaswiki page. `https://midas.triumf.ca/MidasWiki/index.php/Main_Page`. Accessed: 2018-09-09.

[106] P. A. Amaudruz et al. In-situ characterization of the Hamamatsu R5912-HQE photomultiplier tubes used in the DEAP-3600 experiment. 2017.

[107] Courtney T. Mielnichuk. A likelihood ratio algorithm for removing localized alpha particle backgrounds in the deap-3600 detector. Master's thesis, University of Alberta, 2017.

[108] P. A. Amaudruz et al. First results from the DEAP-3600 dark matter search with argon at SNOLAB. *Phys. Rev. Lett.*, 121(7):071801, 2018.

[109] A. Sinnock and B. Smith. Refractive indices of the condensed inert gases. *Phys. Rev.*, 181:1297–1307, May 1969.

[110] G. M. Seidel, R. E. Lanou, and W. Yao. Rayleigh scattering in rare gas liquids. *Nucl. Instrum. Meth.*, A489:189–194, 2002.

[111] Emily Grace and James A. Nikkel. Index of refraction, Rayleigh scattering length, and Sellmeier coefficients in solid and liquid argon and xenon. *Nucl. Instrum. Meth.*, A867:204–208, 2017.

[112] N. Ishida et al. Attenuation length measurements of scintillation light in liquid rare gases and their mixtures using an improved reflection suppresser. *Nucl. Instrum. and Meth. A*, 384(2):380 – 386, 1997.

[113] D. Stolp, O. Dalager, N. Dhaliwal, B. Godfrey, M. Irving, K. Kazkaz, A. Manalaysay, C. Neher, S. Stephenson, and M. Tripathi. An estimation of photon scattering length in tetraphenyl-butadiene. *JINST*, 11(03):C03025, 2016.

[114] V. Alvarez et al. SiPMs coated with TPB : coating protocol and characterization for NEXT. *JINST*, 7:P02010, 2012.

[115] R. Francini et al. VUV-Vis optical characterization of Tetraphenyl-butadiene films on glass and specular reflector substrates from room to liquid Argon temperature. 2013.

[116] Andrew Hime. The MiniCLEAN Dark Matter Experiment. In *Particles and fields. Proceedings, Meeting of the Division of the American Physical Society, DPF 2011, Providence, USA, August 9-13, 2011*, 2011.

[117] Nuclear recoil acceptance band str. Internal Collaboration Document, J. Walding.

[118] Robert D. Cousins and Virgil L. Highland. Incorporating systematic uncertainties into an upper limit. *Nucl. Instrum. Meth.*, A320:331–335, 1992.

[119] P. Agnes et al. DarkSide-50 532-day Dark Matter Search with Low-Radioactivity Argon. 2018.

[120] D. S. Akerib et al. Results from a search for dark matter in the complete LUX exposure. *Phys. Rev. Lett.*, 118(2):021303, 2017.

[121] Dario Motta and Stefan Schonert. Optical properties of Bialkali photocathodes. *Nucl. Instrum. Meth.*, A539:217–235, 2005.

[122] J. Calvo et al. Measurement of the attenuation length of argon scintillation light in the ArDM LAr TPC. *Astropart. Phys.*, 97:186–196, 2018.

[123] A. Bansal and A. Penzkofer. Spectroscopic and travelling-wave lasing characterisation of tetraphenylbenzidine and di-naphtalenyl-diphenylbenzidine. *Applied Physics B*, 91(3):559–569, Jun 2008.

[124] S. Wallace-Williams et al. Excited state spectra and dynamics of phenyl-substituted butadienes. *J. Phys. Chem.*, 98:60–67, 1994.

Appendices

Appendix A

Toy Optical Model

To cross-reference the RAT simulation and provide a faster method for testing optical parameters, a Toy Optical model (Toy MC) was created. This Model was a stand-alone piece of code which computed the propagation of VUV and optical photons through the detector. This model was created to build PDFs to fit the response of the PMTs from the laserball data. The original optical model only had two parameters. The success of this original study prompted for further development of this optical model to describe the AARF and Ar scintillation data. The model progressively became more advanced until it was modelling the majority of the optics through the microphysics. Once this model was in reasonable agreement with data, the optical model was ported into the RAT simulation. Once in RAT, a subsequent round of optical parameter tuning was performed as described in Chapter 7. This appendix will quickly outline the original PMT characterization study and will then go through the mechanics of the Toy MC and show comparisons between data and MC parameter distributions.

A.1 PMT Characterization

For the PMT characterization, the optical model only consisted of two parameters that could be modified to match the optics. There was the reflectivity of the TPB (r_{TPB}) which was wavelength and angle independent. This probability was also identical for photons hitting the gas/TPB interface and the acrylic/TPB interface. There was also a probability for reflection off the PMT face. The specific geometry of the PMT was not modelled, instead just a flat surface at the end of the LG was assumed. The laserball is not fully isotropic; instead, it illuminates the bottom of the detector more than the top. To account for this the initial $cos\theta$ direction of the photons were binned into eight regions. PDFs were then made, split by the number of reflections at each surface and by the initial $cos\theta$ direction of the photon leaving the laserball. When the PDFs are generated, the probability of reflection at each interface is set to 50%, and the photons are emitted from the laserball isotropically. The PDFs are rescaled in the fit function according to the reflection, and laserball uniformity fit parameters. The PDFs are then convoluted with a PMT response function. In this way, the PMT timing response function, laserball uniformity, and optical parameters were extracted from the laserball data. Figure 1.1 shows three sample comparisons of the laserball data and fit function for three laserball z locations.

The PMT response function used in the fit was a gaussian prompt distribution, an exponential convoluted with a gaussian for the late pulsing and the double pulsing time distribution was measured from data and convolved with the prompt gaussian.

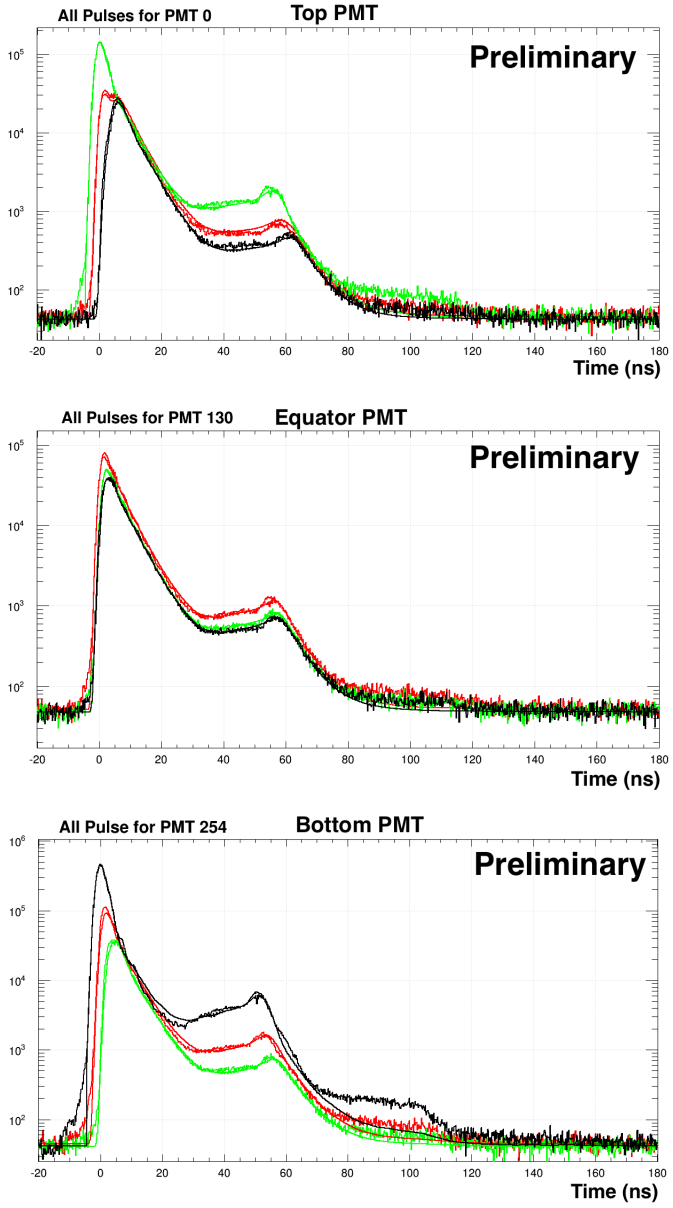

Figure 1.1: Samples comparisons between the generated laserball response compared to the data. This is shown for (Top) PMTID 0, (Middle) PMTID 130 and (Bottom) PMTID 254. The Laserball data at laserball Z locations (Red) Centre, (Green) -550 mm and (Black) +550 mm. Data is in solid lines and model in dashed.

The parameters for the PMT response were in good agreement with what was expected based on the Hamamatsu specifications for the R5912 PMTs,

giving a average transit time spread of ∼1 ns. The measured transit time for the PE followed the expected voltage dependence as shown in Figure 1.2. The probability of reflection off TPB was found to be ∼ 40%, and the probability of reflecting off the PMT found to be ∼ 20%. The PMT reflectance is consistent with the expected PMT reflections [121]. The laserball uniformity was also found to be within reasonable agreement with ex-situ measurements.

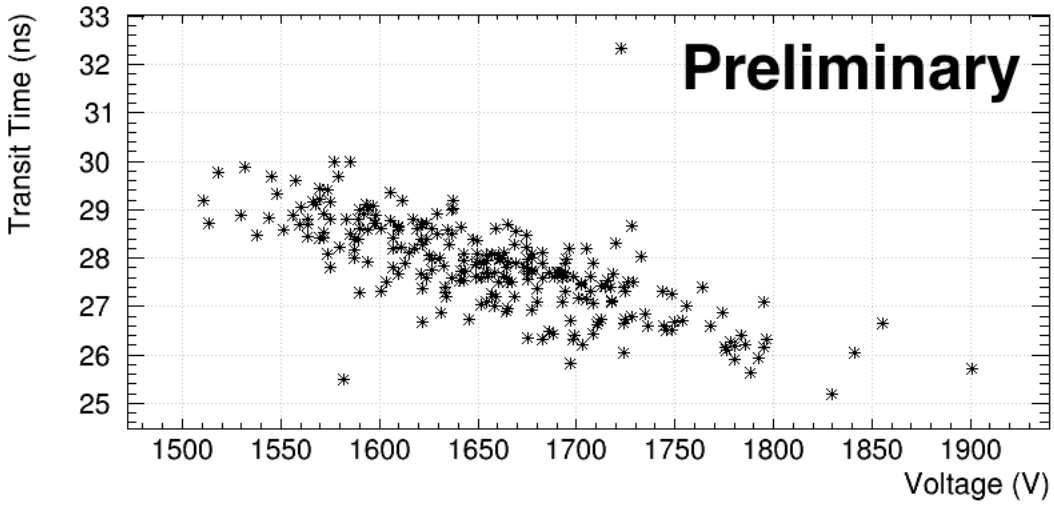

Figure 1.2: Fit Transit times vs the applied voltage to the base of the PMT.

While the PMT fits were in good agreement with the data, there was a concern that the amount of reflection was correlated with possible tails in the PMT prompt response. This study was repeated using the full optical model discussed in Chapter 7; however, even with the inclusion of additional degrees of freedom in the PMT response function, very poor agreement has been made in describing the exponential nature of tail of the laserball data with the RAT optical model.

A.2 Simulation Geometry

As the toy model matured, the simple effective parameter optical model was replaced with one that attempted to compute the optics from the macro-physics happening within the materials and at each of the boundaries. The physical model allowed for a much more in-depth look at the critical parameters that govern the optical characteristics of the detector. This made it possible to almost entirely adopt the optics from the Toy MC into the RAT simulation code. What follows is a detailed overview of how the toy optical model and how the propagation of the photons was handled.

The Toy model uses a reduced geometry with six main volumes:

- ArGas: r<850mm and Z> Ar Level)
- ArLiquid: r<850mm and Z< Ar Level)
- TPB Coating: 3-micron layer at r=851mm.
- AVAcrylic: 850mm<r<900mm
- Light Guides: 900mm<r<125000mm
- PMT Volume: 12500 mm to the PMT Face.

Photon propagation is carried out within a volume by computing the straight path length to the next encountered boundary. This path length is then compared to the distance for different physics processes. The list of physics processes varies for the different materials.

A.3 Materials

A.3.1 Ar Gas

The Ar gas is considered to be equivalent to vacuum thus does not contain any physics processes other than straight photon propagation. As such, the materials index of refraction is 1.0, and all photons propagate at c.

A.3.2 Liquid Ar

In the liquid Ar (LAr) there are four physics processes that are simulated: straight photon propagation, Rayleigh scattering, photon absorption and VUV emission from singlet and triplet dimer states. The optical properties of the LAr are calculated using the Sellemeier coefficients fit in [111] via:

$$n^2 = a_0 + \frac{a_{uv}\lambda^2}{\lambda^2 - \lambda_{uv}^2} + \frac{a_{ir}\lambda^2}{\lambda^2 - \lambda_{ir}^2}, \tag{1.1}$$

where λ_{UV} corresponds to the closest or first UV resonance and λ_{IR} corresponds to the closest or first IR resonance. The group velocity (v_g) of a photon is then

$$v_g = \frac{c}{n(\lambda) - \lambda(dn/d\lambda)}. \tag{1.2}$$

Figure 1.3 shows the group velocity of light in the LAr. From the index of refraction, the Rayleigh scatter length (l_r) can be computed using [94]

$$l_r^{-1} = \frac{16\pi^3}{6\lambda^4 N} kTNk_T(\frac{(n^2-1)(n^2+2)}{3})] \tag{1.3}$$

where k_T is the compressibility of the LAr and N is the number density of Ar atoms (N in the numerator and denominator cancel in the limit of small compressibility). A random distance to the Rayleigh scatter (d_r) can then be selected via

$$d_r = -l_r ln(n_{random}) \tag{1.4}$$

where n_{random} is a random floating point number between 0.0 and 1.0. When a photon is scattered, an arbitrary angle is selected via

$$rand = 1 - cos(\theta)^2 \pm \theta = cos^{-1}(\sqrt{}(1 - n_{rand})) \tag{1.5}$$

where the sign of θ is also chosen randomly. This distribution assumes an ideal Rayleigh angular distribution. The photon absorption length in the LAr is not explicitly known and depends on the number of impurities in the LAr. No clear sign of photon absorption was seen in the data. A value of 30 m was used, which is consistent with our expectation of the LAr purity and the analysis here [122].

The VUV light emission is isotropic at the event location with a singlet/triplet ratio tuned to match data. The time components for the light emission are initially taken as 7 ns and 1450 ns.

A.3.3 TPB

Several physical phenomena are simulated within the TPB: photon propagation, isotropic scattering, and fluorescence. The index of refraction for TPB is taken from [123], wavelengths below the reported range are given a constant

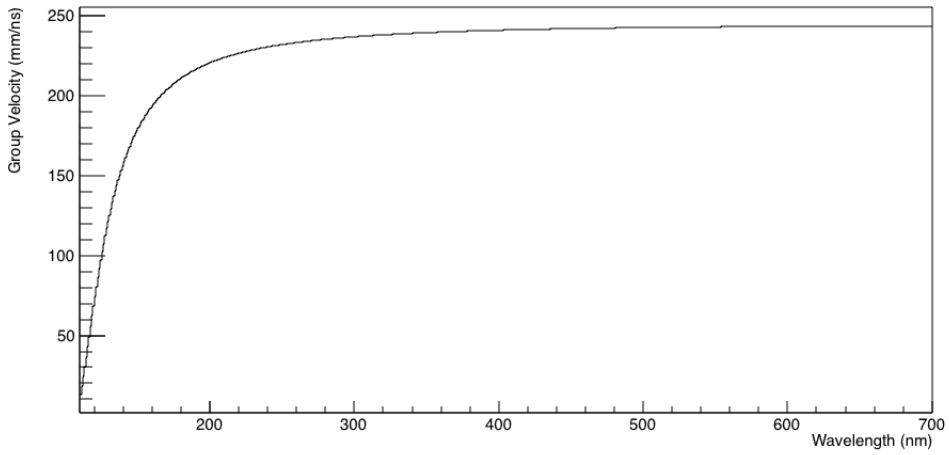

Figure 1.3: Group velocity of light in liquid Ar as computed using the index of refraction computed in Ref. [111].

value. Variations of the index of refraction did not have a significant impact on the optical characteristics.

The scattering length in TPB is assumed to have the same wavelength dependence as Rayleigh scattering, but the angular distribution is taken to be uniform. The literature value for the scatter length of TPB is 2.75 um for $\lambda = 420$ nm [113]; however, there are reasons to believe that this may be an overestimate due to the assumption of the TPB index of refraction. The TPB scatter length is tuned to match data, a value closer to 150 was found to produce an $fMaxPE_{prompt}$ close to data.

The efficiency of fluorescence is set to 100% and the emission spectrum from [124] is used. Any inefficiency in the fluorescence is difficult to decouple from the PMTs photon detection efficiency and is left to be accounted for in an overall efficiency scaling put in to match the measured LY.

A.3.4 Acrylic

The physical processes in the acrylic are the same as the TPB. The photon absorption lengths are fixed to the values measured for the AV acrylic, shown in Figure 1.4. The scattering length for the acrylic is not known, from the optical appearance of the acrylic, the scatter length must be long and is set to 5 m. The scattering length of the LGs did not seem to have a significant effect until made un-physically small.

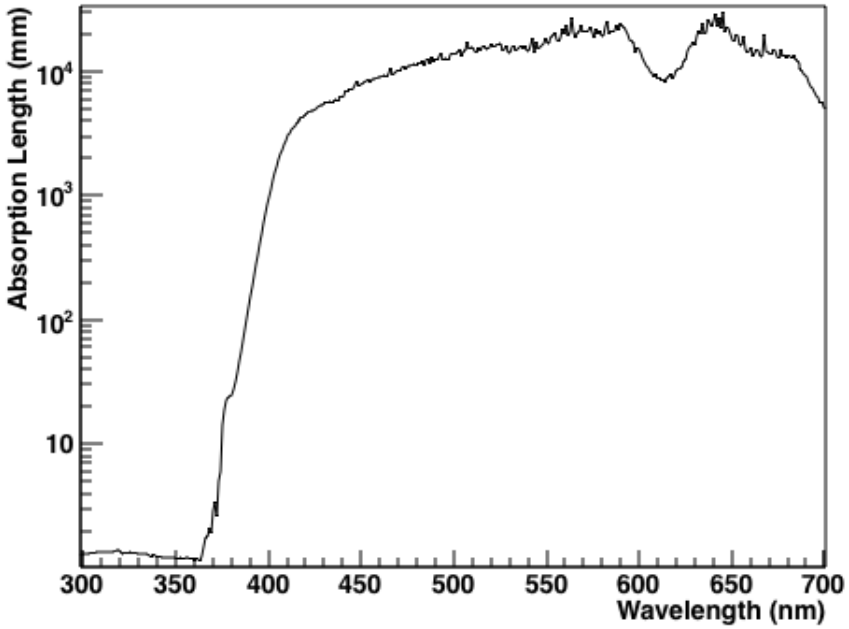

Figure 1.4: The absorption length of light in acrylic [87].

A.4 Volumes

This section will discuss the equations specific to volumes to decide how photons propagate.

A.4.1 Inner Volume

For photons traveling within the inner volume, first the position of the intersection with the TPB coating is calculated via:

$$d_{TPB} = -\hat{v} \cdot \vec{p_i} + \sqrt{((\hat{v} \cdot \vec{p_i})^2 - |\vec{p_i}|^2 + r_{tpb}^2)}, \tag{1.6}$$

$$\vec{p_f} = \vec{p_i} + d\hat{v}, \tag{1.7}$$

where d_{TPB} is the distance to the TPB intersection, $\vec{v}$ is the velocity, $\vec{p_{i,f}}$ are the initial and final positions and r_{tpb} is the radius of the TPB coating.If $\vec{p_i}$ and $\vec{p_f}$ are not on the same side of the liquid level, then the distance to liquid level intersection (d_{LArL}) is computed via:

$$d_{LArL} = \frac{z_{LAr} - p_z}{v_z} \tag{1.8}$$

where z_{LAr} is the hight of the LAr. If the photon started within the LAr, then a random distance to a Rayleigh scatter (d_r) is computed. The process with the shortest distance is selected as the next step. If a photon hits the LAr surface, then the photon path is computed using the Fresnel and Snell equations. The Fresnel equations compute the probability of reflection from the surface. Photons are assumed to be of random polarization thus giving the Fresnel equations:

$$\alpha = \frac{n_i}{n_f}, \tag{1.9}$$

$$\beta = \sqrt{(}1.0 - \alpha^2(1.0 - (\hat{v} \cdot \hat{n})^2)), \tag{1.10}$$

$$r_par = (\hat{v} \cdot \hat{n} - \alpha * \beta)/(\hat{v} \cdot \hat{n} + \alpha * \beta), \tag{1.11}$$

$$r_perp = (\alpha * \hat{v} \cdot \hat{n} - \beta)/(\alpha * \hat{v} \cdot \hat{n} + \beta), \tag{1.12}$$

$$R = (r_{par}^2 + r_{perp}^2)/2, \tag{1.13}$$

where $n_{i,f}$ are the initial and final index of refraction and R is the reflection probability. If β is imaginary, then the photon is reflected. If the photon is transmitted through the boundary, then a new direction is computed by splitting the velocity into components parallel and perpendicular to the normal $\hat{n}$. The $v_p\hat{e}rp$ is scaled by the ratio of the velocities in the two medium while $\hat{v_{par}}$ is scaled according to Snell's law. The new velocity vector then becomes:

$$\hat{v_f} = \frac{n_i}{n_f}\hat{n} \times (\hat{v_i} \times \hat{n}) - \sqrt{(}1 - (\frac{n_i}{n_f})^2)(1 - (\hat{v_i}\dot{\hat{n}})^2))\hat{n}. \tag{1.14}$$

A.4.2 TPB coating

The TPB coating is characterized by two distributions of normal angles, one for the inner AV edge and another for the Acrylic edge. When a photon hits the TPB interface, the distributions are sampled until an intersecting normal if found. Fresnel equations are again used to determine the reflectance probability. The process repeats until the photon is either transmitted or no

longer directed towards the TPB.

A.4.3 AV Acrylic

The photon propagation in the AV is split into two cases, photons traveling in the positive and negative radial direction. For photons moving in the positive radial direction the intersection point on the AV outer boundary is easily computed using Equation 1.6 but with r_{tpb} replaced with $r_{AVouter} = 900mm$. At the intersection with the outer AV limit, the photons will either hit the neck and be killed, enter a LG or be reflected. For photons reflected back, they can either be Fresnel reflected back or force reflected from the Tyvec reflectors with a penalty factor to account for the reflectivity of the Tyvec material. Reflections off the Tyvec is assumed to follow a Lambertian distribution. Photons moving in the negative radial direction, the existence of an intersection with the TPB is determined by

$$(\hat{v} \cdot \vec{p})^2 - \vec{p} \cdot \vec{p} + r_{AV} > 0.0 \tag{1.15}$$

If it exists, then the intersection point is computed, and the photon can propagate to this boundary. If no solution exists then an intersection with the outer AV boundary is calculated.

A.4.4 Light Guides

Photons are determined to enter the LG when a photon intersects with the outer AV boundary by searching for the closest PMT and then determining if

the photon is within the LG radius by the condition:

$$\hat{p_{pmt}} \cdot \hat{p} >= cos(tan^{-1}(r_{LG}/r_{outerAV})) \tag{1.16}$$

If a photon enters a LG, MC enters a separate LG simulation function, where the photons coordinate are transformed into the LG frame of reference where the cylindrical symmetry of the LG can be exploited. Photons are propagated at each step by finding the 2-dimensional intersection point on the edge of the LG; the photons are propagated to this location in 3 dimensions. The LG simulation handles the photon while 900 mm $< r <$ 1250 mm. If the photon exits the LG at 1250 mm, it enters the PMT volume.

A.4.5 PMT Volume

The PMT volume is defined as the LG region from 1 mm before the centre position on the PMT face to the intersection of the LG Edge and the PMT. Photons are propagated as in the LG simulation; however, an intersection with the PMT face is checked similar to Equation 1.15. If a photon intersects the PMT, the photon is either detected or reflected. The angle-dependent reflection probability is taken from [121]. This reflectivity function was computed for an LAB-to-PMT interface, so it is assumed that the difference in the index of refraction between LAB (n=1.48) and PMMA (n=1.49) is negligible. Photons that hit the LG edge within 1 mm of the end of the LG are killed.

A.4.6 Data Comparison

The optical parameters were only roughly tuned until they matched the data, as such only a general agreement was achieved between the data and MC. For the most part the parameters found in the Toy MC directly translated to the current values put into the RAT MC. This is except for the TPB scattering length. With the Toy MC, the best agreement was achieved with a long TPB scattering length in agreement with measurements of the relative transmittance [114] [115]. Figure 1.5 shows the Comparison of the Toy MC FMaxPE distribution with data for both 3 um and 150 um TPB scattering lengths. The 150 um TPB scattering length is clearly preferred. Figure 1.6 shows the agreement between the Toy MC and data for the charge distribution in an AARF run. One thing to notice with the AARF is that the discrepancy in the amplitude of light in the AARF PMT is opposite the discrepancy in the RAT simulations. While RAT simulated too little light, the Toy MC over predicts the amount of light seen in the AARF PMT. The over prediction is likely due to the omission of PMT saturation and digitizer clipping effects in the Toy MC.

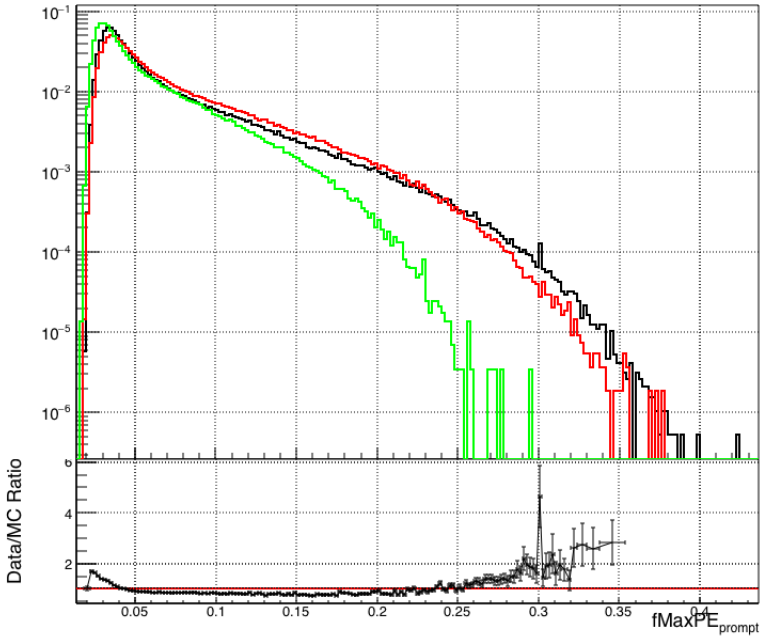

Figure 1.5: Comparison of the fMaxPE computed by the Toy MC with (black) Data. The Toy MC was run with TPB scattering lengths of (Red) 150 um and (Green) 3 um.

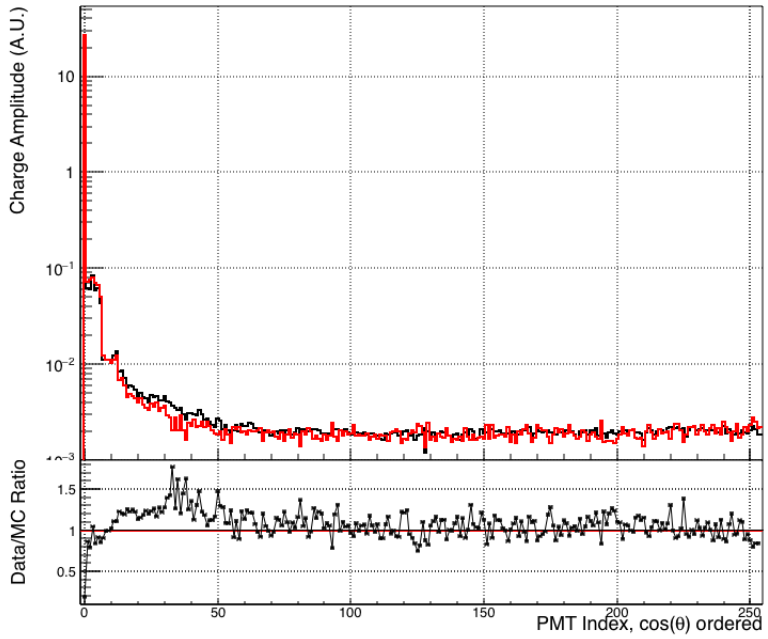

Figure 1.6: Comparison between AARF data and the simulated AARF with the Toy MC with 150 um TPB scattering length.